CORA Cork Open Research Archive
Cartlann Taighde Oscailte Chorcaí

Title	Hybrid materials for flexible, transparent electrodes
Authors	Puicervert, Roxane
Publication date	2017
Original Citation	Puicervert, R. 2017. Hybrid materials for flexible, transparent electrodes. PhD Thesis, University College Cork.
Type of publication	Doctoral thesis
Rights	© 2017, Roxane Puicervert. - http://creativecommons.org/licenses/by-nc-nd/3.0/
Download date	2026-10-31 10:18:27
Item downloaded from	https://hdl.handle.net/10468/5751



UCC
University College Cork, Ireland
Coláiste na hOllscoile Corcaigh

OLLSCOIL NA HÉIREANN

National University of Ireland



Hybrid materials for flexible, transparent electrodes

A Thesis Presented to the National University of Ireland

for the Degree of Doctor of Philosophy

by

Roxane Puicervert

Supervised by Dr. Mary Manning, Dr. Micheál Burke and Dr. Aidan Quinn



Tyndall National Institute

University College Cork

April 2017

I, Roxane Puicervert, certify that this thesis is my own work and I have not obtained a degree in this university or elsewhere on the basis of the work submitted in this thesis.

Roxane Puicervert

Abstract

This thesis investigates the application of metal meshes and Chemical Vapour Deposited graphene hybrid for flexible, transparent heaters. The transfer of graphene – a key step in the fabrication of the hybrid- was first optimised with a Failure Modes and Effects Analysis method to ensure a graphene layer free from mechanical defects (< 2%). The novel electrode was studied with two types of flexible transparent substrates: PET and PEN. The hybrids were recorded with sheet resistance as low as 15 Ω/□ for a material transparency of 82.9%. These performances were not compromised by mechanical testing. The thermal performances were also determined and the addition of graphene improved the thermal resistivity of the heater on PET by 18.7%. The hybrid was assessed under ON/OFF and long period testing for future application prospect. The heater passed the test with performance stable.

Additional works include a study with the aim to better understand the contribution of graphene when transferred on top of metal mesh and determine its limitations. The electrical, transparent and thermal characteristics of different configuration of square meshes with CVD graphene were investigated.

Acknowledgement

I would like to thank my supervisors Dr. Aidan Quinn, Dr. Micheál Burke and Dr. Mary Manning for giving me the opportunity to discover the world of graphene. I am particularly grateful for the many advices and helps that they have provided. Many thanks for your patience too.

Over the years many people helped me but I would like to give special thanks to Krimo Khalfi and Richard Murphy. Krimo, for his help in the training fab and his contagious good humour. Richard Murphy, for the fabrication of many lithographic masks. I am also grateful to Alan O'Riordan and Daniela Iacopino for making me step in Tyndall in the first place.

Morning coffee was always associated with good day so I would like to thanks the many caffeine addicts that were participating to this ritual: thanks Niamh, Pierre, Caoimhe, Benjamin and Armelle. Thanks to the many members of NTG Past and present, the Tyndall taggers and of course the Ballincollig Rugby Ladies.

Merci buckets Niamh, Alfonso & Eleanor: you're a moral bonus.

Thanks to my family and the Kelly's family.

Finally and most importantly thank you Niall. You're a Star!

Table of Contents

Chapter 1: Introduction 5

1.1 Need for flexible transparent electrodes 5

1.1.1 Increase in applications requiring transparent electrodes 5

1.1.2 Transparent and conductive electrodes for use as transparent heaters 3

1.1.3 Requirements for Flexible, Transparent and Conductive Electrode 3

1.1.4 Comparison of the main candidate to replace ITO 7

1.2 Graphene 11

1.2.1 Graphene production 13

1.2.2 Graphene characterisation 14

1.3 Metal Meshes 17

1.4 Scope of this thesis 19

1.5 References 21

Chapter 2: Optimisation of the transfer of Chemical Vapor Deposited Graphene 29

2.1 Introduction 29

2.2 Experimental method 31

2.1.1 Transfer of CVD graphene 31

2.1.3 Failure Mode Identification and Assessment 33

2.3 Results and discussion 35

2.3.1 FMEA results + improvements 35

2.4 Conclusion 43

2.5 References 44

Chapter 3: Hybrid electrode consisting of metal mesh and CVD graphene to use as transparent heater 47

3.1 Introduction 47

3.2 Experimental method 50

3.2.1 Substrate preparation 50

3.2.2 Fabrication of the hybrid electrode: metal mesh & CVD graphene 50

3.2.2 Electrical characterisation of the hybrid device 53

3.2.3 Transparency characterisation 54

3.2.4 Thermal characterisation: set up and measurements Type 1 & 2 54

3.3 Results and discussion 57

3.3.1 Successful transfer of graphene on 3D substrate 57

3.3.2 Electrical performance of the electrode on PEN vs PET 58

3.3.3 Transparency of the electrodes 60
3.3.4 Thermal performance of the electrode on PEN vs PET 61
3.3.5 Figure of merit and comparison to the state of the art alternative 65
3.4 Conclusion 67
3.5 References 68
Chapter 4: Flexibility and stability of the hybrid electrode to meet application requirements 70
4.1 Introduction 70
4.2 Experimental method 72
4.2.1 Thermal characterisation: Type 3 & 4 measurements 72
4.2.2 Fatigue verification: Compression and tension bending cycle 72
4.2.3 Fabrication of the thermochromics device 73
4.3 Results and discussion 74
4.3.1 ON/OFF resistance 74
4.3.2 Long period testing 74
4.3.3 Reliability under bending 75
4.3.4 Thermo-chromic device 78
4.4 Conclusion 79
4.5 References 80
Chapter 5: Study of the effect of CVD graphene on square metal mesh 82
5.1 Introduction 82
5.2 Experimental method 85
5.2.1 Fabrication of the hybrid electrode: metal mesh & CVD graphene 85
5.2.2 Thermal characterisation: Type 1 measurement 85
5.3 Results and discussion 86
5.3.1 Electrical and transmission characteristics associated with the different variable 86
5.3.2 Control of the electrical and thermal characterisation – Measurement's variables 88
5.3.3 Observed effects post transfer of CVD graphene 90
5.3.4 Lead for future work: Comparison pre-, post- and 6 months post transfer 97
5.4 Conclusion 99
5.5 References 100
Chapter 6: Conclusion and future works 101
Conclusion 101
Future works 103

Reference 104
Appendices 105

Chapter 1: Introduction

1.1 Need for flexible transparent electrodes

1.1.1 Increase in applications requiring transparent electrodes

Transparent electrodes form the basis of many optoelectronic devices such as solar cells, light-emitting diodes, flat panel displays and touch screens.

In "Touch screen display market global Industry analysis size, share, growth, trend and forecast" [1], the rapid growth of the touch screen market is attributed to user's familiarities with touch screen through smartphone use. The familiarity to the interface helped the development of new technologies such as touch screen displays (tablet, computer etc.) and kiosks. Expanding applications for displays offers a comfortable range of opportunities for the near future.

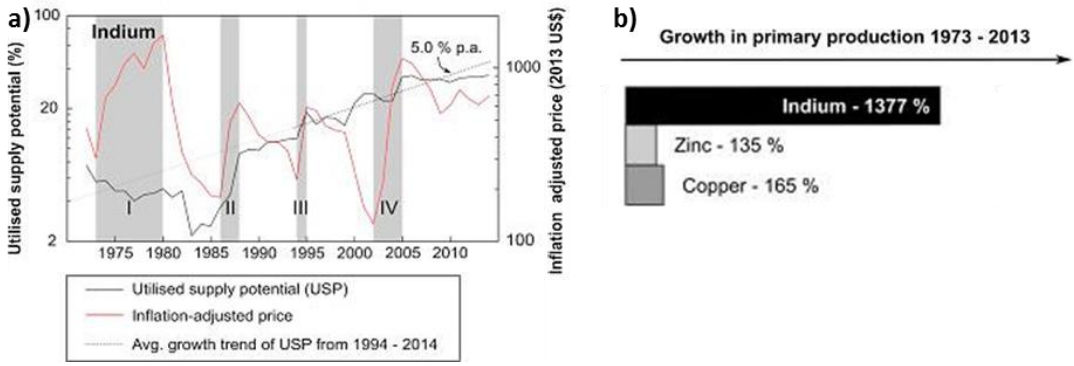


Figure 1.1: a) "Historic evolution of Utilised Supply Potential (USP) and inflation-adjusted price of indium from 1973 to 2014. Shaded areas indicate periods of major increases in demand for the element. I – development of pressurised water reactors with indium controls rods, II – Development of indium-doped tin oxide (ITO) for LCD's and solar cell, III – increased demand from Japan (mainly for ITO), IV – closure of French refineries and Chinese shortages." b) "Relative growth in the primary production of Indium and their associated source materials from 1973 to 2013". Indium is extracted alongside zinc and copper by smelting sulphidic zinc and copper. Figures and caption from [2].

The market opened by the drive for “renewable energy” technologies has also played an important role in the need for transparent electrodes. The recent awareness of global warming and the Paris agreement prioritises the development of technologies and actions to help limiting greenhouse gas emissions and promote climate-resilient development [3]. The transition to greener energy production gathered much interest. Many countries as Germany [4, 3], France[4], Japan [5] and China [6] have invested in solar cells. Efforts have also been focused on the reduction of energy consumption. The buildings sector is the most impacted since such reductions can lead to positive-energy buildings with high quality environmental certifications. Investment is also dedicated to renovations [7]. Smart windows (e.g thermo- and electro-chromic windows) could play an increasing role in the future in that regard.

Films of indium-doped tin oxide (ITO) are the most popular choice for transparent electrodes with low sheet resistance and high transparency. ITO can achieve a transmission of 90% with a sheet resistance as low as 10 Ω/□ [8, 9]. However, ITO has some drawbacks justifying the research into alternative electrode materials. The main reason enunciated was the supply in indium. As seen in the figure 1.1, the main milestones in indium history were highlighted in grey by the authors. The demand for the elements increased significantly since the development of technology depending on ITO films leading to the shortage of some extraction plant. The element is now considered as a “critical” due to its high economic importance and high supply risk [2, 7]. The concern for indium availability in the future is now spreading and, while a crisis is not predicted as imminent, alternative solutions to ITO would reduce risk for the dependent markets [10, 11]. Additionally, the ceramic nature of ITO films is not compatible with flexible substrates [12]. This last point is particularly problematic as the use of flexible substrates for transparent electrodes presents numerous advantages and has become a major driver for future applications. Flexible substrates should be lightweight, thin, robust, conformable and even offer the possibility for future displays to be bent or even rolled if required [13, 14]. The use of flexible substrates has also the potential to help simplify the production of novel displays (e.g. curved).

1.1.2 Transparent and conductive electrodes for use as transparent heaters

In this thesis, focus was given to a specific branch of transparent electrodes: transparent heaters. These devices are found in applications which make use of the heat generated by the passage of an electric current through a conductor: Joule heating. The effect, also known as ohmic heating or resistive heating, can be described by the following formula:

$$P \propto I^2 R \qquad (1.1)$$

Where P is the power

I is the current traveling through the conductor

R is the resistance

Transparent heaters are desired for many applications, the most known is for defogging and defrosting purposes [15, 16] to limit safety issues related to frost and ice in northern countries. For these applications the heater needs to heat uniformly over the entire device and have a low response time. These requirements are also essentials for another category of application: the smart window [17, 18]. In winter, windows are responsible of major heat loss. According to the Norwegian building regulation, 45% of the total heat loss is due to windows. In summer, they are responsible of a rise of temperature due to solar radiation. Considering the energy consumption of a building due to heating/cooling and lighting, the development of smart windows was targeted to help reducing energy consumption. The transparent heaters can be used in two fashions: as simple transparent heater or as a based electrode in thermochromic windows. The first is useful in winter or cold countries by limiting the heat loss through the window. A high transparency also has the advantage to keep the natural radiation. The thermochromic windows on other hand are designed for summer and warm countries. The window limits the rise of temperature due to solar exposure by decreasing its transparency. The change of color is initiated by the transparent heater. In both cases a uniform heat over long periods is also essential.

Transparent heaters are also required for a third category of applications: the pixelated heating display [19]. This category groups many applications such as

MEMs, biochips, artificial skin and point of care. However, these transparent heaters are different to the previous types of heater described. The main difference is the size of the electrode. Instead of a large electrode, the devices are composed of micro-heater patterns. The heaters are also required to be flexible and the control of the temperature needs to be extremely precise and reliable. Finally the materials used should be disposable.

1.1.3 Requirements for Flexible, Transparent and Conductive Electrodes

Electrodes for transparent flexible heaters are evaluated through their electrical, optical and mechanical performance. The cost of fabrication and the environmental impact of the new material should also be taken in consideration.

1.1.3.1 Optical performance

The transparency of an electrode is evaluated through the transmission and the haze characteristics. The transmission determines the amount of light that will pass through the material (vs scattered or absorbed light). The transmission requirements depend on the applications. For example, solar cell efficiency is dictated by the amount of light that can be absorbed by the active layer. Therefore, the transparent electrode dedicated to a solar cell needs high transmission in the 400 to 1750 nm wavelength range to match the spectral irradiance from the sun (as seen in figure 1.2). On the other hand, transparent electrodes dedicated to displays only need to perform in the wavelength range where the eye is most sensitive (from 380 to 800 nm).

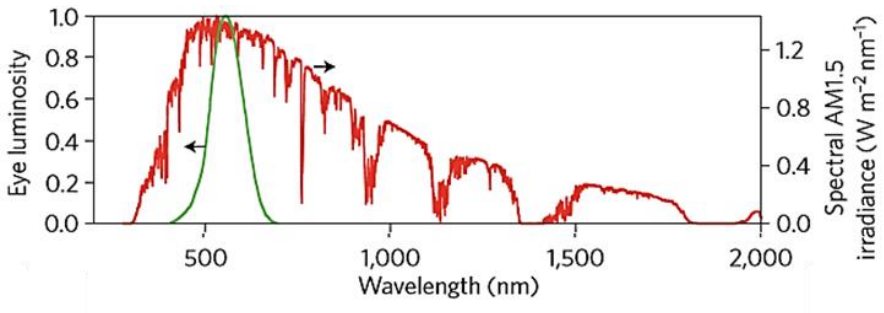


Figure 1.2: Spectral irradiance from the sun under AM1.5 conditions (red) and eye luminosity function range (green)[20].

The haze measurement determines the level of scattering of the light when going through the material. While the haze is not always investigated, it is a particularly important parameter for applications such as displays or smart windows (electro and thermochromic, defogger and defroster etc). A high level of scattering would result with an image with vague contour. Haze less than 0.7% is generally required [21].

1.1.3.2 The electrical performance [22]

The electrical property of semi-conductor at room temperature is represented by its conductivity σ (S.cm^{-1}):

$$\sigma = n_e \mu e \quad (1.2)$$

Where n_e is the free carrier concentration (cm^{-3}),
μ is the carrier mobility (cm^2.V^{-1}.s^{-1}),
and e is the charge of an electron (Coulombs)

However, the resistivity ρ (Ω.cm) -or sheet resistance in the case of thin film and 2D material- is the main property used to compare the electrical performance of different electrodes. The resistivity is the reciprocal of the conductivity and is determined in function of the resistance of the electrode and the dimensions of the material:

$$\rho_{bulk} = \frac{1}{\sigma} = \frac{RA}{L} = \frac{R(w.t)}{L} \quad (1.3)$$

Where R is the resistance (Ω),
A is the cross sectional area (cm^2)
w is the width and t the thickness (cm)
L is the length of the material (cm)
The sheet resistance Rs (Ω/□)is defined as:

$$Rs = \frac{R.w}{L} \quad (1.4)$$

The sheet resistance requirement also depends on the application. Antistatic layers and capacitive touch screens can adapt to higher sheet resistance than would a solar cell. Figure 1.3 gives an overview of these different requirements.

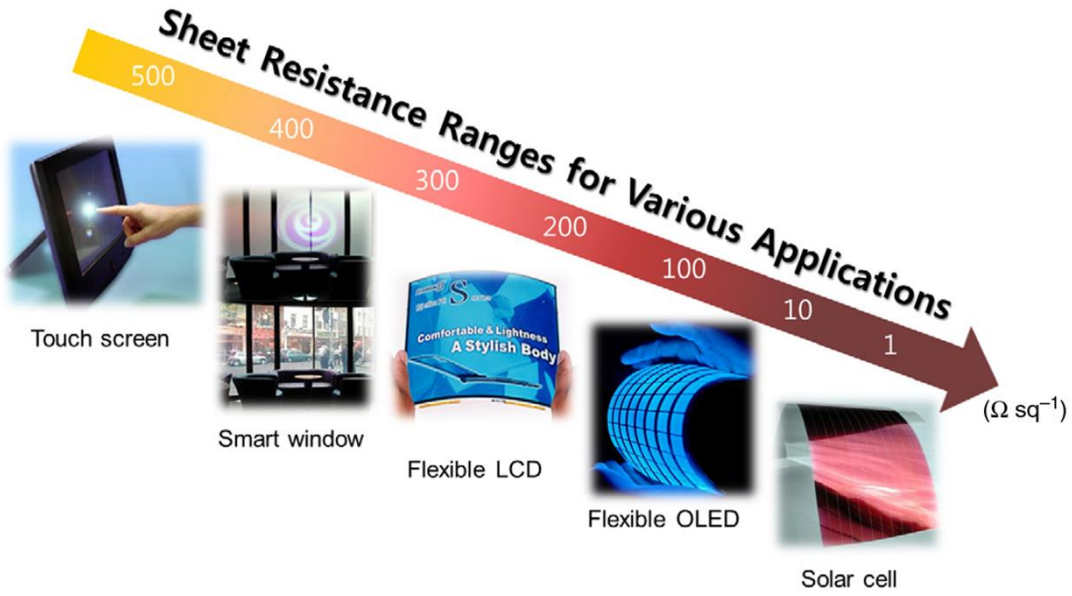


Figure 1.3: Overview of the sheet resistance requirements for transparent electrodes [23]

When a transparent electrode is incorporated in a device, the interaction between the electrode and the additional layer can influence the final device performance.

Note that the optical performance and the electrical performance of a material are linked. From Hagen-Rubens relation, later derived by Drude, it is known that material with large electrical conductivity (ie. metals) are also very good reflectors in the infrared region. A high level of reflection is known to influence transmission and haze [24].

1.1.3.3 Mechanical performance [23]

The flexibility of the electrodes is evaluated through adapted bending and fatigue tests. Most of the time, the sample is bent to a controlled radius for repeated cycles (e.g. 1000).

To date, no quantification method has been used to compare the mechanical properties of flexible TCEs. However, a classification of the flexible display -based on the observed flexibility- was developed by Kimberly J. Allen [24]. The authors differentiate four types of display: Flat, curved or conformed, mildly flexible and fully flexible. In the literature, most of the TCE describe could be categorised as

mildly flexible but the term flexible is generally used instead. In a comprehensive purpose, we use the adapted classification version of M.C. Choi [23] – see Table 1.1.

K.J. Allen	**M.C. Choi**	**Interpretation**
Flat	Flat	Display built on plastic but used in a flat rigid form
Curved or conformed	Conformed	Curved but not flexed during use
Mildly flexible	Flexible	Flexible but not designed for severe treatment
Fully flexible	Rollable	Flexible like paper and cloth

Table 1.1: Summary of the classification of display depending on their flexibility [25-27].

1.1.3.4 Thermal performance

The thermal performance of a conductive layer is characterised by its thermal resistivity. This value is determined by plotting the temperature associated at known power density. The power density can be estimated by recording the current at a given voltage.

The temperature can be determined using a non-contact IR thermal camera. It has the advantage to also characterise the homogeneity of the temperature distribution. The latest being particularly important when the electrode is used for thermo-chromic applications.

1.1.3.5 Fabrication

The electrode fabrication is another important factor. Costs need to be kept low and the method should be easy to implement. Additionally, regulations are increasingly implemented regarding environment and health protection. The process should then have a limited impact on the environment. Use of dangerous and unadvisable chemicals should be avoided. The lifetime of the fabricated product should be also considered, including waste remediation issues and potential for recycling.

1.1.4 Comparison of the main candidates to replace ITO

To date the most suitable candidates for transparent and conductive electrodes can be separated in three main groups:

- Carbon-based materials
- Metallic Nanostructures
- Hybrids

The "carbon-based" category groups materials such as carbon nanotubes and graphene. The "metallic nanostructure" category includes thin metal films, patterned metal grids and metal nanowires. Finally, the "hybrids" family includes electrodes made of more than one material. Table 1.2 gives an overview of the carbon-based and metallic nanostructure characteristics.

1.1.4.1 Carbon based materials

Carbon nanotubes (CNT's) can be divided into two main categories: single-walled- and multi-walled- carbon nanotubes. Both categories are practically insoluble and infusible [28-30] making their incorporation into practical devices difficult. To date, the most effective method consists in incorporating the CNT's in a conductive polymer. The process has the advantage to be compatible with low cost fabrication [31]. The CNT's + polymer composite has been recorded with sheet resistance ranging from 24 to 1000 Ω/□ and transparency from 63 to 90% (without substrate) [32]. These parameters depend on the percentage of CNT present in the mix, the type of CNT used (length and diameters) and the thickness of the polymer. Because of the nature of both materials, the CNT composite is also very flexible. The main disadvantage of the CNT's composite can be its surface roughness. Low quantity of polymer insures a better transparency but present a high surface roughness [33].

Graphene's main advantage comes from its 2D nature. Undoped graphene has a sheet resistance ≈ 6 kΩ/□ with a material transparency of 2.3%. Large scale production is also available. More details are given in the section 1.2 Graphene.

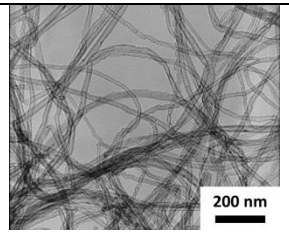
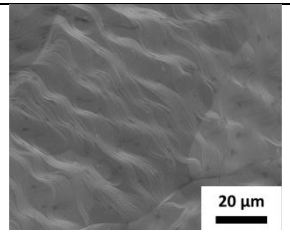
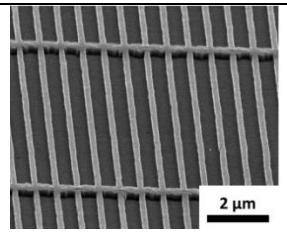
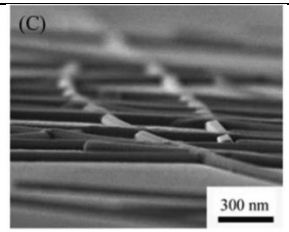
	Carbon based materials		Metallic based materials	
	Carbon nanotubes	**Graphene**	**Mesh**	**Silver nanowires**
Image				
Transparency	63 – 90% (400 to 800 nm)	T > 90% (400 to 800 nm)	70 – 90 %	80 – 90% (400 to 800 nm)
Haze	0.1 – 0.3%			H > 2%
Sheet resistance	24 – 1000 Ω/□	> 280 Ω/□	1 – 60 Ω/□	8 – 14 Ω/□
Roughness	5 – 10 nm	Depending of the substrate		
Flexible	Yes	Yes	Yes	Yes
Fabrication	- Dry-drawing - Solution processing - Gas filtering technique	- Liquid phase exfoliation - Chemical vapor deposition	- UV lithography - Nano-imprint lithography - Rolling mask lithography - EHD jet printing	- Brush painting - Dip coating - Doctor blade coating - Drop casting
References	[34-38]	[39-43]	[44]	[44]

Table 1.2: Table recapitulating the key characteristics of the main contender to replace ITO in transparent electrodes.

1.1.4.2 Metallic nanostructures

Ultrathin metal film is a term used to describe a metal film of thickness < 10 nm [45]. Two structural configurations are particularly known: oxide / metal / oxide (OMO) and dielectric / metal/ dielectric (DMD) [32]. The OMO structure is the most successful to date and the metal of choice are generally silver and copper [32]. The fabrication of the thin metal film is done by improving the wetting capacity of the metals on a chemically heterogeneous supporting film [46-50]. The electrodes fabricated have sheet resistance varying from 10 to 100 Ω/□ with transparency ranging from 70 to 85 % [39]. These parameters are dictated by the metal thickness, for the value given the thickness of the metal was varied from 5 to 13 nm. The thin film was also proven to be flexible and have the potential to be used in roll to roll processing [51]. While a promising alternative for transparent electrodes, the ultrathin metallic films require a fabrication process not yet fully understood. To date the process is inefficient and very challenging suggesting that high production cost should be considered.

Silver nanowires (AgNWs) are a very interesting alternative for transparent electrodes. One of the strongest assets of this material is the ease of implementation and the low-cost of their production. Additionally, the electrodes fabricated from AgNW have sheet resistance varying from 1 to 100 Ω/□, transparency around 80 to 90% [52] and excellent flexibility [53]. However, the random nature of the Ag mesh enhances the scattering of light resulting in high haze [35, 54]. The use of larger diameter nanowires can also give difficulties as it increases the surface roughness [25-31, 55].

Patterned metal grids consist of a metallic nano- or micro- structure. They have sheet resistances ranging from 1 to 60 Ω/□ and transparency from 70 to 90%. These characteristics can be affected by many parameters such as the metal used, the metal thickness or again parameters related to the structure (geometry, line width, pitch size etc…). The possibility to fabricate the metal mesh through Electrohydrodynamic (EHD) jet printing or transfer printing is also very encouraging for low cost and large scale production [22, 44, 56-64].

1.2 Graphene

Graphene is a two dimensional material formed of carbon atoms in a honeycomb like structure. It was first isolated in 2004 through mechanical exfoliation of graphite by Andre Geim and Kostya Novoselov [65]. Despite its recent discovery, graphene was already heavily studied theoretically being considered as starting point for the study of graphite, carbon nanotubes and fullerenes.

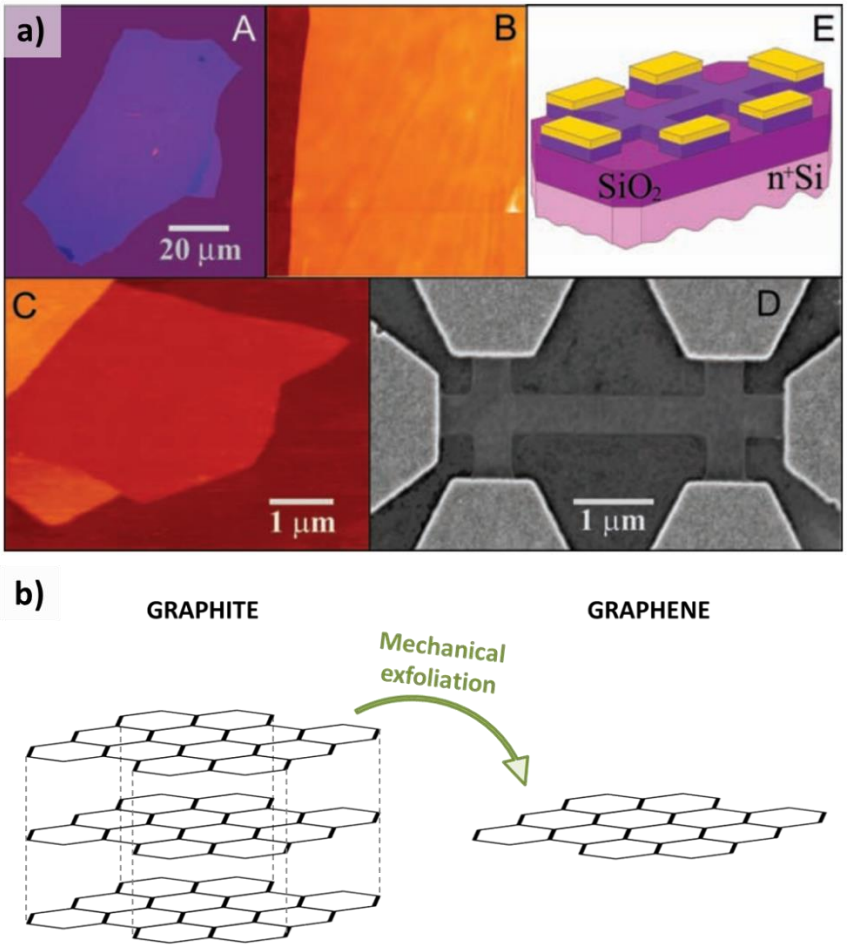


Figure 1.4: a) Figure extracted from "Electric Field Effect in Atomically Thin Carbon Films"[66], the first reported successful isolation of graphene. (A) Multilayer graphene flake transferred on an oxidized Si wafer (B) Atomic force microscope (AFM) image of 2x2 μm area of multi-layer graphene near the edge of the flake (C) AFM image of a single-layer graphene (D) Scanning electron microscope (SEM) image of one of the devices prepared (E) Schematic view of the device in (D). b) Schematic of the structure of graphite and graphene.

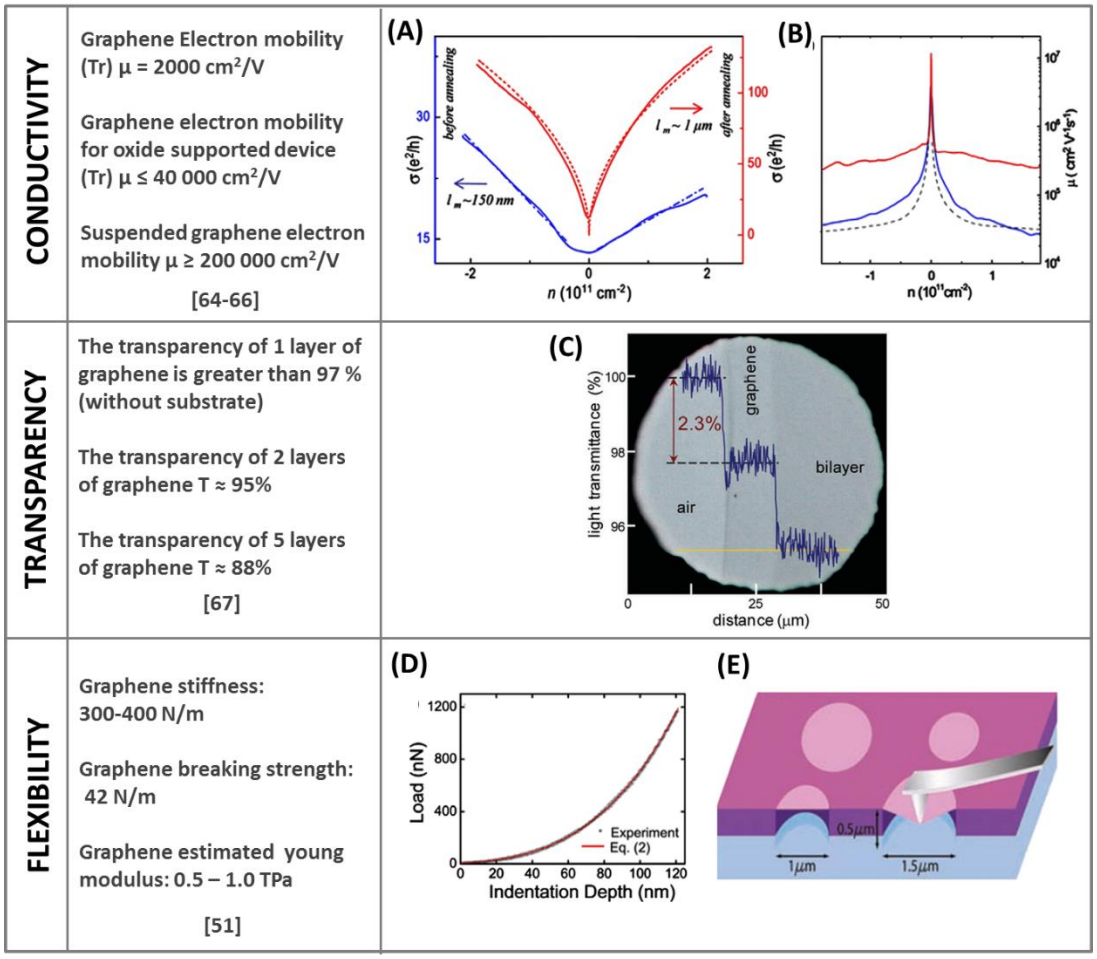


Figure 1.5: Set of properties that makes graphene a promising transparent conductor. (Tr) stand for room temperature and T for transparency. [67] CONDUCTIVITY: (A) Conductance of a suspended graphene sample in function of the carrier density Pre (Blue) and post (red) annealing. Measurement done at 40 K [68] (B) Electron mobility in function of the carrier density [60].

TRANSPARENCY: (C) Optical micrograph of one and two layers of graphene in contrast of an uncovered area (Air). The transmittance was given for wavelength 550 nm [56, 57].

FLEXIBILITY: (D) Loading/unloading curve for suspended graphene (E) Schematic of the system used to obtained the curve (AFM nanoindentation) [58, 59].

Since its discovery, graphene has gathered much interest due to a remarkable combination of characteristics including a high mobility [60], transparency [22, 61-64] mechanical strength and flexibility [69]. This interesting set makes it a potential candidate for use in future flexible optoelectronic devices [70-73].

1.2.1 Graphene production

Overall, three types of graphene are available [74-77]: films supported by smooth substrates [78-80], oriented flakes or nano walls supported by diverse substrates [63, 69, 81-83] and flakes originating from graphite [63, 69, 84, 85]. Each type of graphene benefits from multiple methods of fabrication. The quality of graphene, the scalability to large production, or again the costs of the method are characteristics that vary strongly from one method to another. For example, graphene flakes can be obtained through the mechanical exfoliation or liquid phase exfoliation. Mechanical exfoliation has the advantage to produce micron-scale graphene of very good quality but the method of fabrication requires to deposit the graphene layers by hand using tape. The method is not suitable for large scale production and is mainly used in research where the highest quality is required. Liquid phase exfoliation on the other hand is cheap and scalable to large scale production, but the method is aggressive and the graphene obtained a low yield of single layer and has sheet resistances ranging from 22.5 to > 900 kΩ/□ [86]. It was also reported that the use of reduced graphene oxide can limit the electrode's sheet resistance to 350 Ω/□ (80% of transparency without substrate) [86].

From the variety of method available, three have the potential to be used for large production: graphene made from Chemical Vapor Deposition (CVD), epitaxial growth and liquid phase exfoliation. As stated earlier, the liquid phase exfoliation produces poor quality graphene removing it from the list of the possible candidate for TCE use. The epitaxial growth on other hand, is capable to produce graphene of high quality on the surface of a SiC substrate [59, 87-90]. The method is based on the thermal decomposition of SiC. However, SiC wafers are difficult to produce making the process very expensive. Additionally, the graphene is limited to a wafer size and the graphene fabricated is not always monolayer. Finally, the graphene can't be transferred making its use for transparent electrode impossible.

The last contender is chemical vapour deposition. The method involves the reaction between a gaseous precursor and a heated catalyst substrate that leads to the formation of thin solid films. In the case of CVD graphene, the gaseous precursor can be acetylene, methane, ethanol. Copper and nickel are the two main catalyst

substrates [59]. The methods have the advantage to be adaptable to roll to roll fabrication [91].

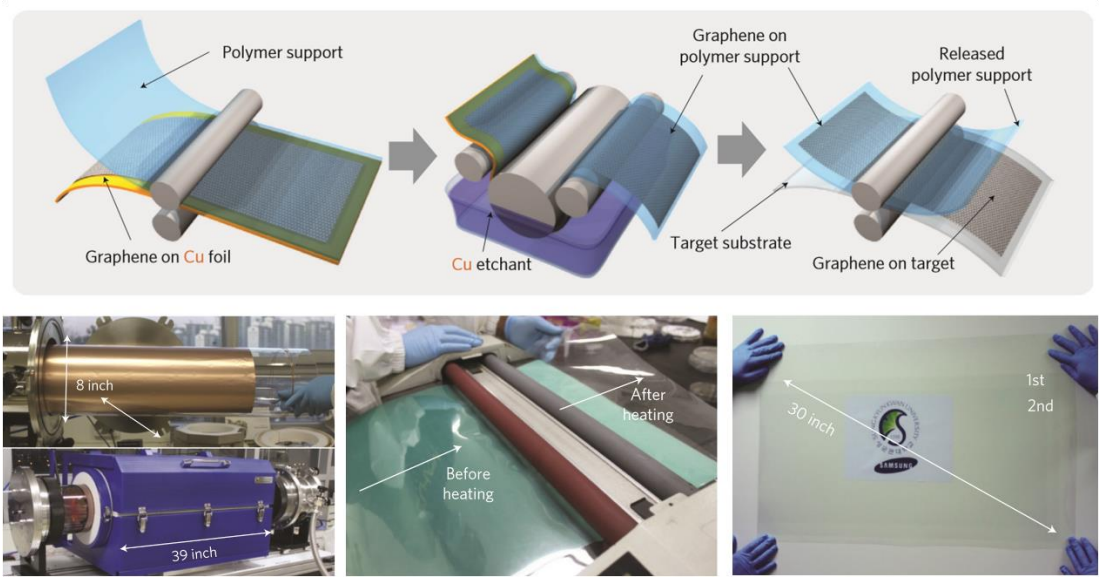


Figure 1.6: a) Schematic of the transfer of CVD graphene on copper using a roll to roll procedure b) CVD growth of graphene on copper. On the upper picture, the catalytic substrate (copper) is wrapped around a quartz tube of 7.5-inch diameter. On the lower picture, the tube was inserted in the reactor (8 inch of diameter) c) Image of the transfer of graphene + releasing tape to a polyethylene terephthalate substrate using the roll to roll technique d) Large graphene film transferred on a 35-inch PET sheet. 2 layers of graphene were transferred.[91]

1.2.2 Graphene characterisation

Many methods of characterisation are used to verify the quality of graphene. Only two are presented in this section as both were intensively used in this thesis work.

Optical characterisation

Due to its high transparency, the observation of graphene through standard microscopy requires one to take certain precautions. Blake P. [91] reported that the substrate on which graphene is transferred and the wavelength of the light used for the observation play a critical role in “making graphene visible”. Graphene needs to be transferred onto a substrate composed of silicon covered by a given thickness

(e.g. 90 nm or 300 nm) of SiO_2 and the illumination source should be emitting at wavelength from 400 to 600 nm.

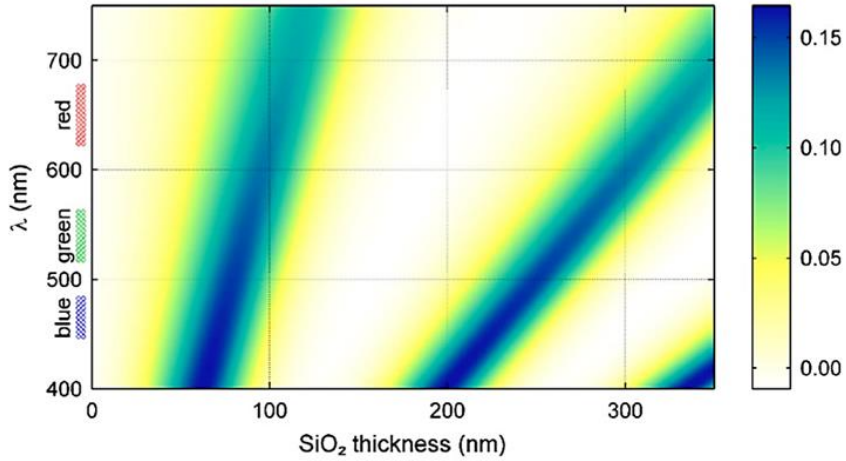


Figure 1.7: False colour plot of the optical contrast for graphene on a oxidised silicon substrate as a function of the illumination wavelength and the SiO_2 thickness.[92]

Note that alternatives to oxidised silicon have been studied. Graphene is also visible on 50 nm Si_3N_4 [91-93] and 72 nm Al_2O_3 on Si wafer [77] using blue light.

Raman spectroscopy

Raman spectroscopy is particularly popular for the characterisation of graphene. The method is fast and provides information about the electronic and structure of the material studied. In the case of graphene, Raman spectra are mainly used to [94]:

- determine the number of graphene layers and therefore confirm when a single layer is present [95];
- highlight the presence of defects;
- reveal the level of doping, which can be intentional or un-intentional;
- study the effect of strain on graphene
- and finally, in the case of bi-layer graphene the method can be used to assess the layers orientation.

A typical Raman spectrum for graphene has three main peaks [36]:

- The D peak (≈ 1360 cm^{-1}): this peak is only present when the sp^2 hybridation of graphene is perturbed. Therefore it is a good indicator of structural defects and/or impurities.
- The G peak (≈ 1560 cm^{-1}): The full width at half-maximum (FWHM) and peak position of this peak varies when graphene is doped.
- And the 2D peak (≈ 2700 cm^{-1}): the typical FWHM of a monolayer graphene is 24.5 cm^{-1}. A single Lorentzian fit can be used for a graphene monolayer while a bilayer graphene has an asymmetric peak.

Additional information can be deduced by checking the area (A_{2D}/A_G) and/or intensity (I_{2D}/I_G) ratios between the 2D and G peaks.

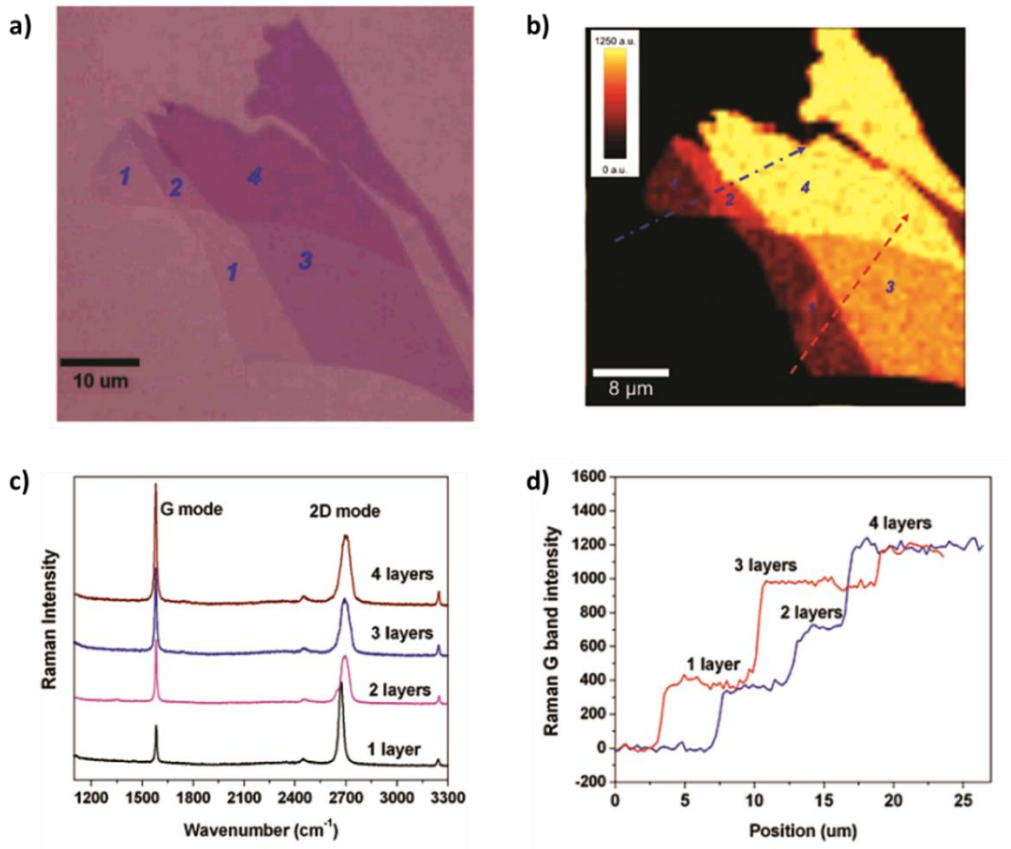


Figure 1.8: Determination of the number of layers using Raman spectroscopy. a) Optical image of a mechanically exfoliated graphene transferred on a Si/SiO_2 substrate. The blue number represents the number of graphene layers. b) Raman image plotter from the intensity of the G peaks. The blue and red dotted lines highlight the area from which the cross sections were taken. c) Raman spectrum for sample with 1 to 4 layers of graphene. d) Cross section from the Raman image.[95]

1.3 Metal Meshes

Metals have excellent conductivity but poor transparency. The use of metal mesh structures allows the combination of the electrical properties of the metals while improving the transparency by creating open areas. The line width of the metal mesh, the metal thickness and the space of open area can be manipulated to design a transparent electrode with specific properties. Note that the line width should ideally be kept < 5 µm to keep the mesh invisible to the human eye [35].

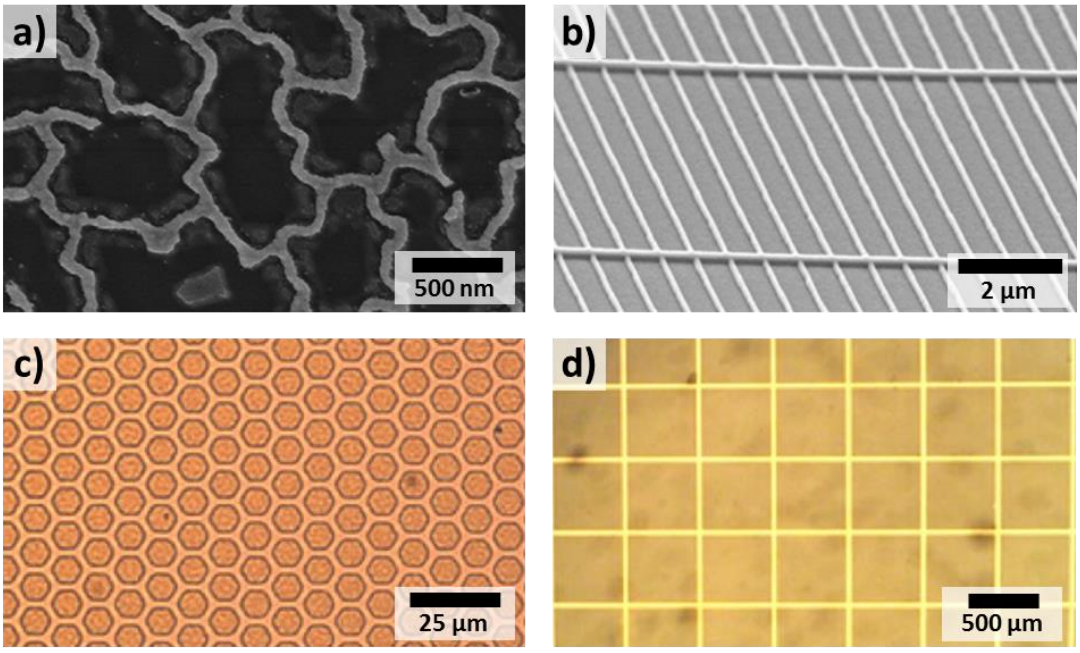


Figure 1.9: Example of metal mesh geometry found in literature. a) Nanomesh electrodes made by grain boundary lithography [36]. b) Cu nanowire mesh fabricated by transfer printing [37]. c) Hexagonal gold grids [35, 96] and d) Square Cu mesh [35] made using photolithography.

To date, standard structures such as square and hexagonal meshes are commonly used. However, these geometries were not designed to efficiently distribute stress under mechanical strain. The development of new types of metal mesh is regularly investigated to overcome this issue. Examples are presented in figure 1.9.

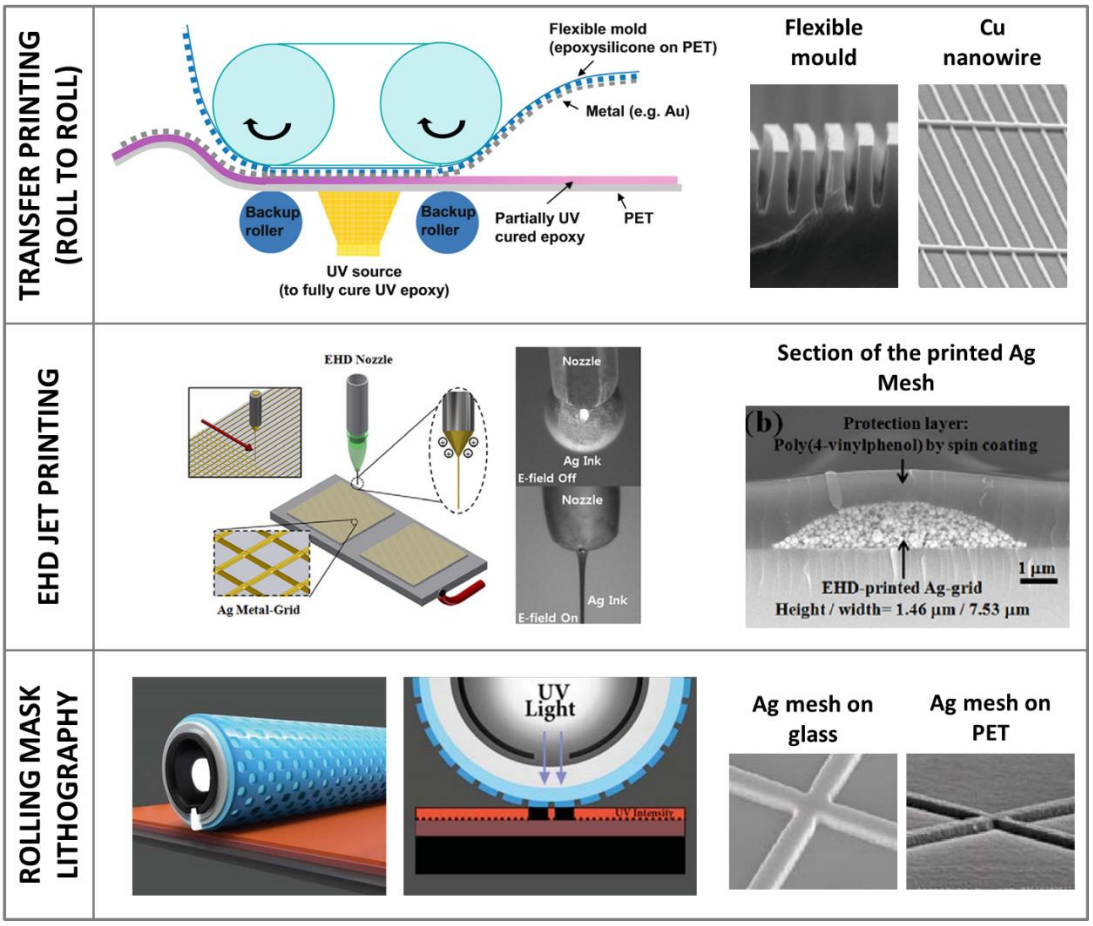


Figure 1.10: Most popular methods for the fabrication of metal mesh. [96-98]

The fabrication of metal meshes can be done through a variety of methods including UV Lithography to ink jet printing. Both methods can be adapted to large scale production. The methods based on the lithography principles such as transfer printing and rolling mask can be used for very fine features. The transparency of such devices will then be excellent. Additionally, the method is well known due to its intensive use in the semi-conductor area. However, the method requires the use of toxic chemicals and a substantial starting investment. Printing techniques on other hand are cheap and can fabricate meshes in one step. The main downside of the method is the minimal line width that can be reached (4 to 40 µm) and the solution used for the metal ink [99, 100]. Figure 1.10 presents the three main contenders available.

1.4 Scope of this thesis

The scope of this thesis is to study viable materials to use as alternative for flexible and transparent electrodes. The electrodes will need to have suitable electrical performance (Sheet resistance < 50 Ω/□), as well as good transparency (Transmittance > 80% from 400nm to 800nm not including the substrate) and mechanical characteristics (Flexible qualification). In addition, the electrodes will have to be suitable for use as heaters for future applications such as thermochromic devices for smart windows or pixelated heating displays. The transparent and conductive electrodes investigated will be a hybrid made of a metal mesh and graphene.

Chapter 2 focuses on the transfer of CVD graphene from copper to targeted substrates. Despite the literature available on the subject, the transfer protocol can result in graphene of poor quality. The high chance of failure is due to the numerous steps and the high technicality required. A Failure Modes and Effects Analysis (FMEA) method was developed to rigorously assess and optimise the transfer method. The focus of the FMEA was to obtain graphene free of mechanical defects. The chapter includes the establishment of the FMEA, the improvements made to the transfer protocol as well as the evaluation of the graphene obtained pre- and post- application of the FMEA method.

Chapter 3 focuses on the fabrication of hybrid transparent electrodes answering the requirements cited earlier. CVD graphene was transferred on top of a novel pentagonal mesh designed to support strain due to compression and tension bending. Additionally, the hybrid device was fabricated on two of the most common plastic substrates for flexible devices. While the flexibility is an important aspect of the electrode, this chapter only focus on the evaluation of the electrical performance, transparency and thermal performance for both type of devices made.

In Chapter 4, preliminary tests were performed to establish if the new hybrid transparent electrodes could manage the strain associated with real life

applications. The electrodes were subjected to flexibility and fatigue test as well as on/off and long period use.

In chapter 5, graphene was transferred on top of different grid meshes made of titanium and gold. The aim was to investigate and better understand the contribution and limitation of graphene in the thermal performance of metal mesh / CVD graphene hybrids. Different grid sizes and different metal thicknesses were tested. The study also includes the electrical performance and transparency results of the different combinations available. The thermal analysis presented in this chapter focus on important details such as the maximum and median temperature, the range of temperatures and the thermal resistivity for each combination.

Finally, the conclusion and future work chapter gives a summary of the key results achieved, the conclusions drawn from the presented work and thoughts on future work.

1.5 References

1. *Touch Screen Display Market - Global Industry Analysis, Size, Share, Growth, Trends and Forecast 2016 - 2024*. February 2017, Report buyer.
2. Frenzel, M., et al., *Quantifying the relative availability of high-tech by-product metals – The cases of gallium, germanium and indium.* Resources Policy, 2017. **52**(Supplement C): p. 327-335.
3. *Paris Agreement*. 2015 December 12.
4. *Transition énergétique : quels investissements pour quelle compétitivité ?*
5. Dinçer, F., *The analysis on photovoltaic electricity generation status, potential and policies of the leading countries in solar energy.* Renewable and Sustainable Energy Reviews, 2011. **15**(1): p. 713-720.
6. Liu, L.-q., et al., *Solar energy development in China—A review.* Renewable and Sustainable Energy Reviews, 2010. **14**(1): p. 301-311.
7. *Energy transition for green growth act*. 2016 July.
8. Stadler, A., *Transparent Conducting Oxides—An Up-To-Date Overview.* Materials, 2012. **5**(4): p. 661.
9. Guillén, C. and J. Herrero, *Comparison study of ITO thin films deposited by sputtering at room temperature onto polymer and glass substrates.* Thin Solid Films, 2005. **480–481**: p. 129-132.
10. Leterrier, Y., et al., *Mechanical integrity of transparent conductive oxide films for flexible polymer-based displays.* Thin Solid Films, 2004. **460**(1): p. 156-166.
11. Chen, Z., et al., *A mechanical assessment of flexible optoelectronic devices.* Thin Solid Films, 2001. **394**(1): p. 201-205.
12. Logothetidis, S., *Flexible organic electronic devices: Materials, process and applications.* Materials Science and Engineering: B, 2008. **152**(1): p. 96-104.
13. Laforte, J.L., M.A. Allaire, and J. Laflamme, *State-of-the-art on power line de-icing.* Atmospheric Research, 1998. **46**(1): p. 143-158.
14. Thomas, S.K., R.P. Cassoni, and C.D. MacArthur, *Aircraft anti-icing and de-icing techniques and modeling.* Journal of Aircraft, 1996. **33**(5): p. 841-854.

15. Grynning, S., et al., *Windows in the buildings of tomorrow: Energy losers or energy gainers?* Energy and Buildings, 2013. **61**: p. 185-192.
16. *ZEB Final Report*. 2017, The research council of Norway: Trondheim.
17. Cooney, C.G. and B.C. Towe, *A thermopneumatic dispensing micropump.* Sensors and Actuators A: Physical, 2004. **116**(3): p. 519-524.
18. Moschou, D., et al., *All-plastic, low-power, disposable, continuous-flow PCR chip with integrated microheaters for rapid DNA amplification.* Sensors and Actuators B: Chemical, 2014. **199**(Supplement C): p. 470-478.
19. Ellmer, K., *Past achievements and future challenges in the development of optically transparent electrodes.* Nat Photon, 2012. **6**(12): p. 809-817.
20. Crawford, G., *Flexible Flat Panel Displays*. 2005: Wileys.
21. Hummel, R.E., *ELECTRONIC PROPERTIES OF MATERIALS*. 2011, Gainesville: Springer.
22. Sukang, B., et al., *Towards industrial applications of graphene electrodes.* Physica Scripta, 2012. **2012**(T146): p. 014024.
23. Choi, M.-C., Y. Kim, and C.-S. Ha, *Polymers for flexible displays: From material selection to device applications.* Progress in Polymer Science, 2008. **33**(6): p. 581-630.
24. Allen, K.J., *Reel to Real: Prospects for Flexible Displays.* Proceedings of the IEEE, 2005. **93**(8): p. 1394-1399.
25. Snow, E.S., et al., *High-mobility carbon-nanotube thin-film transistors on a polymeric substrate.* Applied Physics Letters, 2005. **86**(3): p. 033105.
26. Cao, Q. and J.A. Rogers, *Ultrathin Films of Single-Walled Carbon Nanotubes for Electronics and Sensors: A Review of Fundamental and Applied Aspects.* Advanced Materials, 2009. **21**(1): p. 29-53.
27. Rouhi, N., D. Jain, and P.J. Burke, *High-Performance Semiconducting Nanotube Inks: Progress and Prospects.* ACS Nano, 2011. **5**(11): p. 8471-8487.
28. Yu, Z., et al., *Intrinsically Stretchable Polymer Light-Emitting Devices Using Carbon Nanotube-Polymer Composite Electrodes.* Advanced Materials, 2011. **23**(34): p. 3989-3994.

29. Zhang, D., et al., *Transparent, Conductive, and Flexible Carbon Nanotube Films and Their Application in Organic Light-Emitting Diodes.* Nano Letters, 2006. **6**(9): p. 1880-1886.
30. Rowell, M.W., et al., *Organic solar cells with carbon nanotube network electrodes.* Applied Physics Letters, 2006. **88**(23): p. 233506.
31. Jing, G., et al., *Modification of carbon nanotube transparent conducting films for electrodes in organic light-emitting diodes.* Nanotechnology, 2013. **24**(43): p. 435201.
32. Yun, J., *Ultrathin Metal films for Transparent Electrodes of Flexible Optoelectronic Devices.* Advanced Functional Materials, 2017. **27**(18): p. 1606641-n/a.
33. Guillén, C. and J. Herrero, *TCO/metal/TCO structures for energy and flexible electronics.* Thin Solid Films, 2011. **520**(1): p. 1-17.
34. Guo, C.F., et al., *Highly stretchable and transparent nanomesh electrodes made by grain boundary lithography.* 2014. **5**: p. 3121.
35. Kang, M.-G., et al., *Transparent Cu nanowire mesh electrode on flexible substrates fabricated by transfer printing and its application in organic solar cells.* Solar Energy Materials and Solar Cells, 2010. **94**(6): p. 1179-1184.
36. Sam, F.L.M., et al., *Thin film hexagonal gold grids as transparent conducting electrodes in organic light emitting diodes.* Laser & Photonics Reviews, 2014. **8**(1): p. 172-179.
37. Ghosh, D.S., T.L. Chen, and V. Pruneri, *High figure-of-merit ultrathin metal transparent electrodes incorporating a conductive grid.* Applied Physics Letters, 2010. **96**(4): p. 041109.
38. Lordan, D., et al., *Asymmetric Pentagonal Metal Meshes for Flexible Transparent Electrodes and Heaters.* ACS Applied Materials & Interfaces, 2017. **9**(5): p. 4932-4940.
39. Basarir, F., et al., *Recent progresses on solution-processed silver nanowire based transparent conducting electrodes for organic solar cells.* Materials Today Chemistry, 2017. **3**: p. 60-72.

40. Guo, F., et al., *Fully Solution-Processing Route toward Highly Transparent Polymer Solar Cells.* ACS Applied Materials & Interfaces, 2014. **6**(20): p. 18251-18257.

41. De, S., et al., *Silver Nanowire Networks as Flexible, Transparent, Conducting Films: Extremely High DC to Optical Conductivity Ratios.* ACS Nano, 2009. **3**(7): p. 1767-1774.

42. Menamparambath, M.M., et al., *Silver nanowires decorated with silver nanoparticles for low-haze flexible transparent conductive films.* 2015. **5**: p. 16371.

43. Lee, J.-Y., et al., *Solution-Processed Metal Nanowire Mesh Transparent Electrodes.* Nano Letters, 2008. **8**(2): p. 689-692.

44. Novoselov, K.S., et al., *Electric Field Effect in Atomically Thin Carbon Films.* Science, 2004. **306**(5696): p. 666-669.

45. Ghosh, D.S., *Basics of Ultrathin Metal Films and Their Use as Transparent Electrodes*, in *Ultrathin Metal Transparent Electrodes for the Optoelectronics Industry*, D.S. Ghosh, Editor. 2013, Springer International Publishing: Heidelberg. p. 11-32.

46. Choi, Y.-Y., et al., *Flexible ZnSnO3/Ag/ZnSnO3 multilayer electrodes grown by roll-to-roll sputtering on flexible polyethersulfone substrates.* Journal of Vacuum Science & Technology A: Vacuum, Surfaces, and Films, 2011. **29**(6): p. 061502.

47. Yong-Seok, P., C. Kwang-Hyuk, and K. Han-Ki, *Room temperature flexible and transparent ITO/Ag/ITO electrode grown on flexile PES substrate by continuous roll-to-roll sputtering for flexible organic photovoltaics.* Journal of Physics D: Applied Physics, 2009. **42**(23): p. 235109.

48. Guillén, C. and J. Herrero, *Transparent electrodes based on metal and metal oxide stacked layers grown at room temperature on polymer substrate.* physica status solidi (a), 2010. **207**(7): p. 1563-1567.

49. Park, Y.-S., H.-K. Kim, and S.-W. Kim, *Thin Ag Layer Inserted GZO Multilayer Grown by Roll-to-Roll Sputtering for Flexible and Transparent Conducting Electrodes.* Journal of The Electrochemical Society, 2010. **157**(8): p. J301-J306.

50. Choa, S.-H., et al., *Mechanical integrity of flexible InZnO/Ag/InZnO multilayer electrodes grown by continuous roll-to-roll sputtering.* Solar Energy Materials and Solar Cells, 2011. **95**(12): p. 3442-3449.
51. Hu, L., H. Wu, and Y. Cui, *Metal nanogrids, nanowires, and nanofibers for transparent electrodes.* MRS Bulletin, 2011. **36**(10): p. 760-765.
52. Preston, C., et al., *Optical haze of transparent and conductive silver nanowire films.* Nano Research, 2013. **6**(7): p. 461-468.
53. Hu, L., et al., *Scalable Coating and Properties of Transparent, Flexible, Silver Nanowire Electrodes.* ACS Nano, 2010. **4**(5): p. 2955-2963.
54. Ahn, B.Y., D.J. Lorang, and J.A. Lewis, *Transparent conductive grids via direct writing of silver nanoparticle inks.* Nanoscale, 2011. **3**(7): p. 2700-2702.
55. Hamon, M.A., et al., *Dissolution of Single-Walled Carbon Nanotubes.* Advanced Materials, 1999. **11**(10): p. 834-840.
56. Castro Neto, A.H., et al., *The electronic properties of graphene.* Reviews of Modern Physics, 2009. **81**(1): p. 109-162.
57. Novoselov, K.S., et al., *Two-dimensional gas of massless Dirac fermions in graphene.* Nature, 2005. **438**(7065): p. 197-200.
58. Kim, K.S., et al., *Large-scale pattern growth of graphene films for stretchable transparent electrodes.* Nature, 2009. **457**(7230): p. 706-710.
59. Bae, S., et al., *Roll-to-roll production of 30-inch graphene films for transparent electrodes.* Nat Nano, 2010. **5**(8): p. 574-578.
60. Lee, C., et al., *Measurement of the Elastic Properties and Intrinsic Strength of Monolayer Graphene.* Science, 2008. **321**(5887): p. 385-388.
61. Bonaccorso, F., et al., *Graphene photonics and optoelectronics.* Nat Photon, 2010. **4**(9): p. 611-622.
62. Gunho, J., et al., *The application of graphene as electrodes in electrical and optical devices.* Nanotechnology, 2012. **23**(11): p. 112001.
63. Novoselov, K.S., et al., *A roadmap for graphene.* Nature, 2012. **490**(7419): p. 192-200.
64. Huang, X., et al., *Graphene-Based Electrodes.* Advanced Materials, 2012. **24**(45): p. 5979-6004.

65. Soldano, C., A. Mahmood, and E. Dujardin, *Production, properties and potential of graphene.* Carbon, 2010. **48**(8): p. 2127-2150.

66. Bolotin, K.I., et al., *Temperature-Dependent Transport in Suspended Graphene.* Physical Review Letters, 2008. **101**(9): p. 096802.

67. Bolotin, K.I., et al., *Ultrahigh electron mobility in suspended graphene.* Solid State Communications, 2008. **146**(9–10): p. 351-355.

68. Nair, R.R., et al., *Fine Structure Constant Defines Visual Transparency of Graphene.* Science, 2008. **320**(5881): p. 1308.

69. Levchenko, I., et al., *Scalable graphene production: perspectives and challenges of plasma applications.* Nanoscale, 2016. **8**(20): p. 10511-10527.

70. Yang, X., et al., *Clean and efficient transfer of CVD-grown graphene by electrochemical etching of metal substrate.* Journal of Electroanalytical Chemistry, 2013. **688**: p. 243-248.

71. Wang, M., et al., *CVD Polymers for Devices and Device Fabrication.* Advanced Materials, 2017. **29**(11): p. 1604606-n/a.

72. Lee, H.C., et al., *Synthesis of Single-layer Graphene: A Review of Recent Development.* Procedia Chemistry, 2016. **19**(Supplement C): p. 916-921.

73. Zhang, Y., L. Zhang, and C. Zhou, *Review of Chemical Vapor Deposition of Graphene and Related Applications.* Accounts of Chemical Research, 2013. **46**(10): p. 2329-2339.

74. Bi, H., et al., *Graphitization of nanocrystalline carbon microcoils synthesized by catalytic chemical vapor deposition.* Journal of Applied Physics, 2008. **104**(3): p. 033510.

75. Liu, J., et al., *Direct growth of graphene nanowalls on the crystalline silicon for solar cells.* Applied Physics Letters, 2015. **106**(4): p. 043904.

76. Mostofizadeh, A., et al., *Synthesis, Properties, and Applications of Low-Dimensional Carbon-Related Nanomaterials.* Journal of Nanomaterials, 2011. **2011**: p. 21.

77. Wu, Y.H., T. Yu, and Z.X. Shen, *Two-dimensional carbon nanostructures: Fundamental properties, synthesis, characterization, and potential applications.* Journal of Applied Physics, 2010. **108**(7): p. 071301.

78. Ciesielski, A. and P. Samori, *Graphene via sonication assisted liquid-phase exfoliation.* Chemical Society Reviews, 2014. **43**(1): p. 381-398.

79. Pei, S. and H.-M. Cheng, *The reduction of graphene oxide.* Carbon, 2012. **50**(9): p. 3210-3228.

80. Cai, M., et al., *Methods of graphite exfoliation.* Journal of Materials Chemistry, 2012. **22**(48): p. 24992-25002.

81. Beshkova, M., L. Hultman, and R. Yakimova, *Device applications of epitaxial graphene on silicon carbide.* Vacuum, 2016. **128**(Supplement C): p. 186-197.

82. Seyller, T., et al., *Epitaxial graphene: a new material.* physica status solidi (b), 2008. **245**(7): p. 1436-1446.

83. Hass, J., W.A.d. Heer, and E.H. Conrad, *The growth and morphology of epitaxial multilayer graphene.* Journal of Physics: Condensed Matter, 2008. **20**(32): p. 323202.

84. Li, X., L. Colombo, and R.S. Ruoff, *Synthesis of Graphene Films on Copper Foils by Chemical Vapor Deposition.* Advanced Materials, 2016. **28**(29): p. 6247-6252.

85. Lisi, N., et al., *Rapid and highly efficient growth of graphene on copper by chemical vapor deposition of ethanol.* Thin Solid Films, 2014. **571**: p. 139-144.

86. Song, Y., et al., *Challenges and opportunities for graphene as transparent conductors in optoelectronics.* Nano Today, 2015. **10**(6): p. 681-700.

87. Choi, T., et al. *Roll-to-roll synthesis and patterning of graphene and 2D materials*. in *2015 IEEE International Electron Devices Meeting (IEDM)*. 2015.

88. Kobayashi, T., et al., *Production of a 100-m-long high-quality graphene transparent conductive film by roll-to-roll chemical vapor deposition and transfer process.* Applied Physics Letters, 2013. **102**(2): p. 023112.

89. Juang, Z.-Y., et al., *Graphene synthesis by chemical vapor deposition and transfer by a roll-to-roll process.* Carbon, 2010. **48**(11): p. 3169-3174.

90. Chandrashekar, B.N., et al., *Roll-to-Roll Green Transfer of CVD Graphene onto Plastic for a Transparent and Flexible Triboelectric Nanogenerator.* Advanced Materials, 2015. **27**(35): p. 5210-5216.

91. Blake, P., et al., *Making graphene visible.* Applied Physics Letters, 2007. **91**(6): p. 063124.

92. Gao, L., et al., *Total Color Difference for Rapid and Accurate Identification of Graphene.* ACS Nano, 2008. **2**(8): p. 1625-1633.

93. Akcöltekin, S., et al., *Graphene on insulating crystalline substrates.* Nanotechnology, 2009. **20**(15): p. 155601.

94. Ferrari, A.C., et al., *Raman Spectrum of Graphene and Graphene Layers.* Physical Review Letters, 2006. **97**(18): p. 187401.

95. Ni, Z.H., et al., *Graphene Thickness Determination Using Reflection and Contrast Spectroscopy.* Nano Letters, 2007. **7**(9): p. 2758-2763.

96. Yonghee, J., K. Jihoon, and B. Doyoung, *Invisible metal-grid transparent electrode prepared by electrohydrodynamic (EHD) jet printing.* Journal of Physics D: Applied Physics, 2013. **46**(15): p. 155103.

97. Jaehong, P. and H. Jungho, *Fabrication of a flexible Ag-grid transparent electrode using ac based electrohydrodynamic Jet printing.* Journal of Physics D: Applied Physics, 2014. **47**(40): p. 405102.

98. Baekhoon, S., et al., *Metal-mesh based transparent electrode on a 3-D curved surface by electrohydrodynamic jet printing.* Journal of Micromechanics and Microengineering, 2014. **24**(9): p. 097002.

99. Thanh Huy, P., K. Seora, and K. Kye-Si, *A high speed electrohydrodynamic (EHD) jet printing method for line printing.* Journal of Micromechanics and Microengineering, 2017. **27**(9): p. 095003.

100. Zhang, Z. and T. Si, *Controllable assembly of silver nanoparticles based on the coffee-ring effect for high-sensitivity flexible strain gauges.* Sensors and Actuators A: Physical, 2017. **264**(Supplement C): p. 188-194.

Chapter 2: Optimisation of the transfer of Chemical Vapour Deposited Graphene

The aim was to establish a reliable procedure for the transfer of Chemical Vapour Deposition graphene from its growth substrate to a targeted substrate. The method should allow the transfer of graphene to variable substrate (flat, 3D, rigid, flexible). The quality of the graphene transferred should be as consistent as the raw graphene allows it.

2.1 Introduction

Graphene has raised a lot of interest since it was first isolated by mechanical exfoliation of graphite in 2004 [1]. Graphene's remarkable combination of high carrier mobility [2, 3], transparency [4, 5], mechanical strength and flexibility [6] make it a viable candidate for use in future flexible optoelectronic devices [7-11]. Growth of graphene via chemical vapour deposition (CVD) has been demonstrated as one of the most promising methods to produce graphene at sufficient scale and quality for such high-volume manufacturing applications [12-14]. However, this method relies on the growth of graphene directly on both sides of a host transition metal catalyst like copper, which for most optoelectronics applications requires complete removal. Consequently, significant research effort have been dedicated to the development of suitable graphene transfer processes [5, 15-18]. Of these, one class of graphene transfer methods that has garnered much focus is polymer-assisted transfer, due to ease of implementation and potential for manufacturability.

During the polymer assisted transfer process, graphene is temporarily supported by a protective polymer layer while it is liberated from its host, via selective chemical etching of the catalyst substrate. The protected graphene layer is then transferred onto the desired substrate and the protective layer is removed. The most widely used polymers for this protective layer are thermal release tapes (tens of microns thick) [5, 19, 20] and ultra-thin (~100 nm) spun-cast polymer layers, such as

poly(methyl methacrylate) PMMA [21-25]. Rapid transfer (rates ~150 - 200 mm/min) have been reported for roll-to-roll methods employing thermal release tape [5]. However, the mechanical and thermal stresses associated with the lamination step can cause permanent damage such as structural defects and significant increase of the sheet resistance, particularly when using rigid substrates [26].

Graphene transfer using spun-cast protective polymer layers is slower but provides an end product of good quality and is suited to a variety of substrate types (flat, 3D [23, 27], rigid, flexible, etc). This technique is widely used in the literature and progress continues to be reported regarding the various steps of the process. The complexity and the number of steps increases the possibility to encounter failures, affecting the quality of the transferred graphene and the reliability of the process.

A widely used tool for reliability analysis is Failure Modes and Effect Analysis (FMEA), which was first developed by the United States Army in the late 1940's [28]. It was then extended to the aerospace and automotive industries [29]. It has proven very successful in identifying, prioritising and mitigating failures within processes across a wide range of industries [28-33]. In this chapter, we report on the implementation of a FMEA approach to a typical polymer-assisted graphene transfer process. The FMEA approach results in a significant improvement in the quality of transferred graphene. Finally, derived from the learnings obtained during the FMEA, we offer guidelines toward optimising a graphene transfer process, as part of a future continuous improvement strategy.

2.2 Experimental method

2.1.1 Transfer of CVD graphene

The original transfer process employed is referred as the "standard" procedure and comprises 9 process steps (S1 to S9); see Figure 2.1. After unpacking the as-purchased graphene-coated copper (S1), the graphene was then cut to the appropriate size (~ 1 cm × 1 cm) using scissors (S2). A protective PMMA layer was spun-cast (4000 rpm, 1 minute) onto the front side of the foil (S3) and subsequently heat-cured for 5 minutes at 180°C in an oven (S4). The graphene on the unprotected back-side of the copper was removed (S5) by RF reactive ion etching (RIE) in an oxygen plasma for 90 seconds (50 standard cm3 per minute O2, 100 W). Samples were then placed (PMMA side up) on the surface of an ammonium persulfate solution (0.1M) for several hours to etch away the copper substrate (S6). The graphene/PMMA was transferred from the ammonium persulfate solution to a de-ionised (DI) water bath (using a "carrier" glass slide) and left for one hour (S7). In the meantime, the Si/SiO2 or glass "target" substrates were cleaned with an ultrasonic bath: 15 minutes in acetone, then 15 minutes in isopropanol and finally 15 minutes in DI water. Each PMMA-coated graphene film was then transferred onto the (wet) target substrate (S8) and dried overnight under vacuum. The final step to remove the PMMA (S9) included annealing each sample on a hotplate at 180°C for 5 minutes followed by immersion in acetone for two hours at room temperature and finally rinsing in isopropanol and then de-ionised (DI) water.

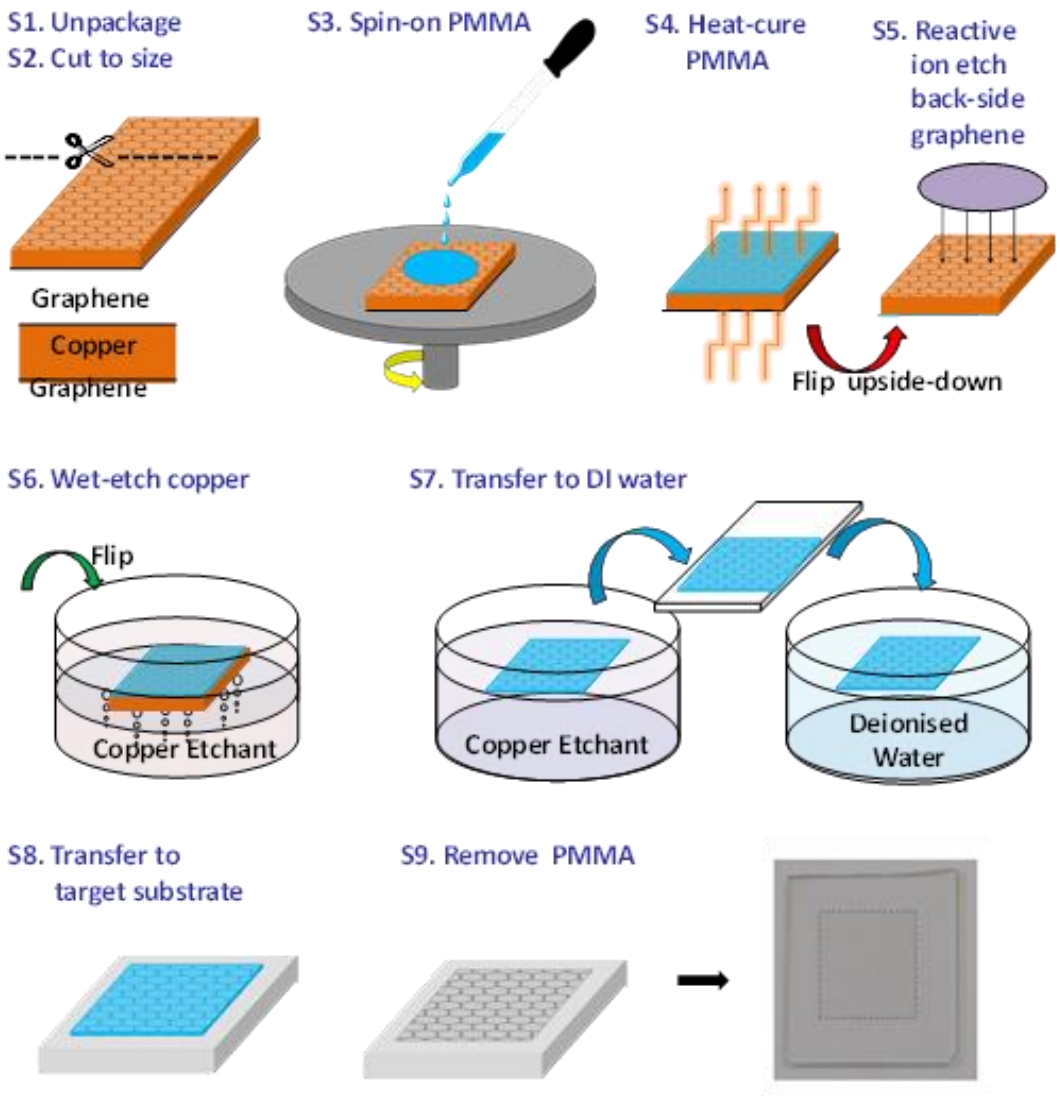


Figure 2.1: Schematic of the main steps (S1 to S9) in the graphene transfer process. Inset: Photograph of an 8 mm x 8 mm graphene layer (border marked by dashed square following transfer to a glass substrate.

2.1.2 Method of characterisation

- **Optical characterisation**
  - **Si/SiO_2 substrate for the optical characterisation**

The substrate was composed of thermally oxidised silicon (90 nm of SiO_2) to facilitate the observation of graphene. The importance of the SiO_2 thickness and the wavelength of the illumination was described in section 1.2.2 [34].

- **Zeiss microscope and VHX-2000 microscope**

Optical images were acquired using a Keyence VHX-2000 microscope for cm-scale regions to monitor macro-defects. A Zeiss Axioscop-II microscope was employed to monitor micro-defects; see Appendix S1. For each transferred sample, one cm-scale optical micrograph and at least 5 high-resolution micrographs were acquired (see Appendix S1).

- **Image J analysis**

Image analysis to quantify defect densities was performed using ImageJ (see Appendix S2). The image was first converted to grey-scale and the edges were identified. The percentage of defects was determined from the quantity of edges pixels compare to the total number of pixels in the image.

- **Raman spectroscopy characterisation**

Raman spectra for transferred graphene samples were acquired at room temperature using a confocal Raman microscope (Renishaw InVia, 514nm laser excitation) from at least 9 regions across the surface; see figure A1 in the Appendix S1.

2.1.3 Failure Mode Identification and Assessment

Determine the potential failures and evaluate their impact

Figure 2.2 shows a flow-chart representation of the FMEA process. Based on the key process steps (S1 – S9), potential failure modes, i.e. “what could go wrong”, were identified for each process step. Each potential failure mode was assessed to determine the effect that this failure mode could have on the quality of the transferred graphene. The impact of the effect was assessed in terms of severity (SEV), likelihood of occurrence (OCC) and likelihood of detection (DET). No record of FMEA methods were found in the literature regarding the transfer of CVD graphene. SEV, OCC and DET scoring criteria were developed following the examples reported by Scipioni [28] and Xu [31]. Severity was scored on a scale of 1 to 10, 10 being most severe; see Table A1 in the Appendix S3 for scoring criteria. Table S2 lists the scoring criteria for likelihood of occurrence (OCC) for a given

failure mode. Table S3 lists the scoring criteria for likelihood of detection (DET). A DET score of 1 means that the detection methods to identify that failure mode are poor or non-existent, while a score of 10 implies excellent detection methods. The Risk Priority Number (RPN) was calculated as the product: RPN = SEV × OCC × DET (maximum value: 1000).

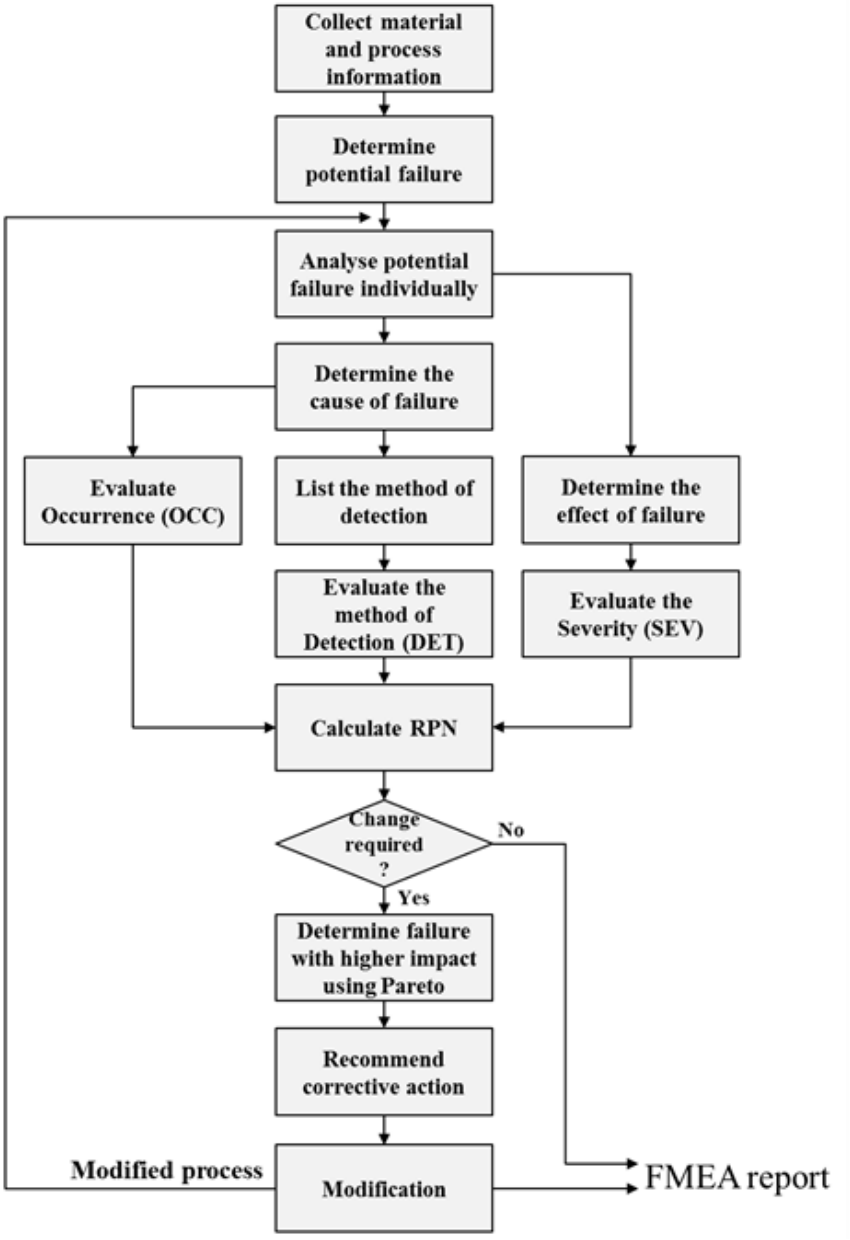


Figure 2.2: Flow chart summarising the FMEA procedure (following Ref. [31])

2.3 Results and discussion

2.2.1 FMEA results + improvements

Optimisation of a graphene transfer process requires accurate and quantitative monitoring of defects from the millimetre to micron scales. Transfer of graphene monolayers to thermally oxidised silicon substrates (90 nm thermal oxide) enables rapid optical monitoring of quality. The top part of Figure 2.3 a) shows a centimetre-scale optical image of a transferred graphene monolayer. Macro-scale structural defects are clearly visible down to the 50 µm scale, including roughly circular holes (due to bubbles underneath the graphene or in the protecting PMMA film) as well as cracks and tears. In order to quantify the defect density, image processing routines (Image J) were employed to highlight edges and identify "defective" regions.

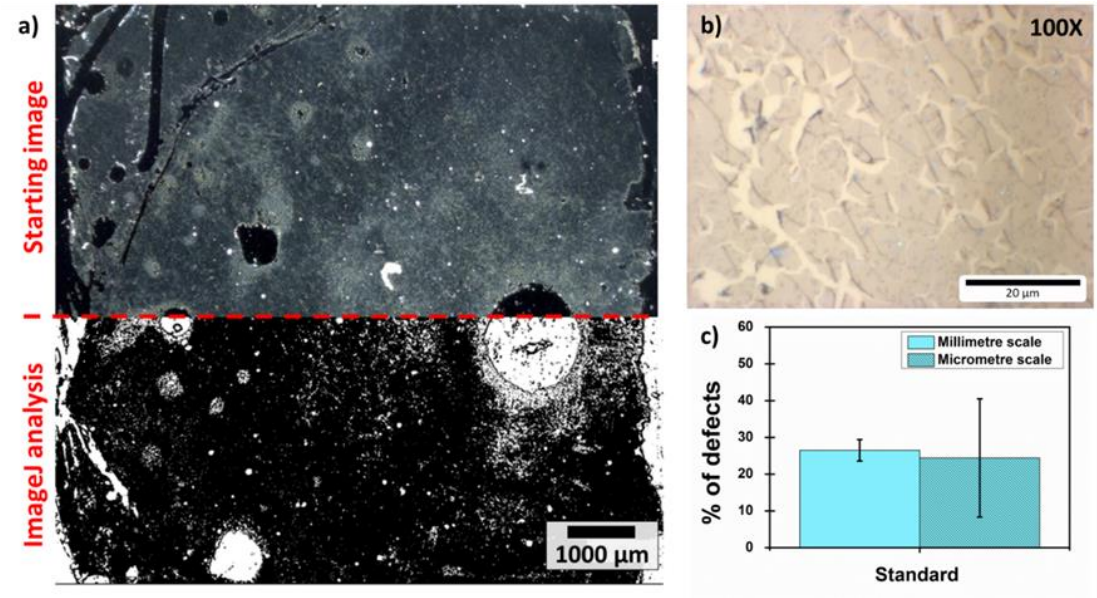


Figure 2.3: a) Optical image of a 1 cm x 1 cm sample (top) with post-processed black-and-white image showing "macro-scale" defects in white (bottom). b) High resolution micrograph of one region from the sample with data shown in a). c) Histogram of defect density as a percentage of sample area at both macro- and micro-scale.

These regions appear in white in the post-processed image shown in the bottom part of Figure 2.3 a). Figure 2.3 b) shows a higher-resolution image revealing micro-

scale defects - cracks in the graphene and process residue (see also Appendix S1, Figure A2). Figure 2.3 c) presents a histogram of the macro-scale and micro-scale defects from several graphene monolayers transferred using the "standard" process described above. For cm-scale images, macro-scale defects (ranging from 50 µm to 700 µm in size) yielded a mean defect density of 26% of the surface area (95% confidence interval: 20% - 33%). The mean defect density for micro-scale defects was 24% of the surface area, with a broader distribution across the different samples and different regions (95% confidence interval: 10% - 39%).

In order to optimise the process, each process step (S1 – S9) was assessed and associated potential failure modes were identified. Table A4 in the Appendix S3 lists all identified Failure Modes (FM1 – FM13) and the associated effect (impact) on the transfer process. Each failure mode was assessed in terms of severity (SEV), likelihood of occurrence (OCC) and likelihood of detection (DET) and the associated Risk Priority Number (RPN) was calculated. The modes whose combined RPN scores accounted for 80% of the summed RPN total (Pareto analysis) are listed in Table 2.1 below. Figure 2.4 shows the RPN scores for all 13 failure modes.

The first significant potential failure mode identified (FM1, RPN = 810) related to unpacking the as-received graphene (process step S1). Contact between the graphene and packaging was assessed as a risk. In order to monitor defects arising from this failure mode, samples were heated on a hotplate in air (up to 220 °C) following the method of Xia et al. [35].

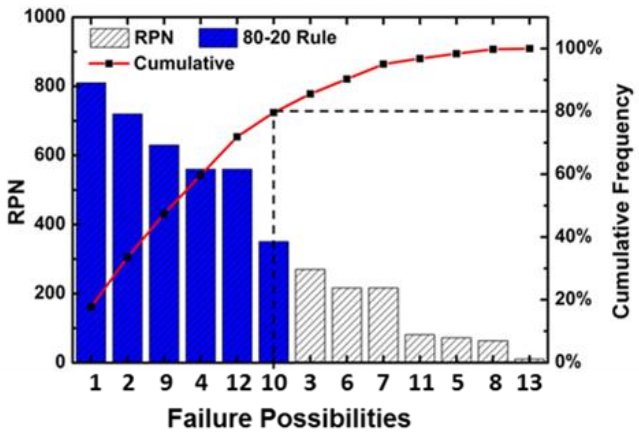


Figure 2.4: Risk Priority Number (RPN) scores of each potential failure mode in decreasing order (maximum RPN value: 1000).

Process Step No.	Key Process Step or Input	Potential Failure Mode	Failure Mode No.	Potential Failure Effects	SEV	Potential Causes	OCC	Current Controls	DET	RPN	Ref.
S1	Unpackaging	Graphene in contact with packaging (vacuum sealed)	**FM1**	Delamination of graphene, surface contamination on remaining graphene.	9	No free space between graphene and packaging	10	None*	9	**810**	
S2	Cutting sample to size	Graphene / Copper substrate deformed when being cut into smaller samples.	**FM2**	Graphene delaminates from Cu or cracks form in graphene.	8	Non-rigid substrate.	10	None*	9	**720**	
S3	PMMA spin-coating	PMMA thickness increases with "age" of solution.	**FM4**	Incomplete removal of PMMA due to thickness non-uniformity. Bubbles in PMMA. Delamination, cracks in graphene.	10	Local stress parallel or perpendicular to graphene-PMMA interface.	7	None**	8	**560**	[21]
S7	Transfer to DI water bath	Graphene surface in contact with "carrier" substrate.	**FM10**	Delamination, cracks in graphene	7	Transfer of graphene from one bath to the other	10	none	9	**630**	[36]
S8	Transfer to target substrate	Poor adhesion to target substrate, moisture/residue between graphene and substrate	**FM11**	Delamination, cracks in graphene. Damage from bubbles	7	Transfer from water bath to target substrate	6	none	9	**378**	[25] [37]
S9	PMMA removal (heating and dissolution)	Sample introduced to pre-heated (180°C) hotplate	**FM12**	Delamination, cracks in graphene	7	Thermal shock	10	None***	8	**560**	

* oxidation of copper can be used to reveal the homogeneity of graphene. ** Tencor can be used to estimate the PMMA thickness

***High-resolution optical microscope can be used post annealing - the graphene is slightly visible through PMMA at 10X and 100 X)

Table 2.1: Failure Mode Effect Analysis – most significant modes (see Table S4 in Supporting Information for complete list)

Since graphene acts as an oxidation barrier, regions of the copper foil without any graphene change colour rapidly (a piece of unprotected copper foil was simultaneously annealed to act as a reference). Panel FM1:S in Figure 2.5 shows a gray-scale optical micrograph with discoloured regions highlighted in blue. This potential failure mode was addressed by requesting specialised packaging, comprising a plastic "dome" to prevent contact between the vacuum-shrunk plastic packaging and the front side of the graphene-on-copper foil sample. Optical images for these annealed samples (Figure 2.5, FM1:O) revealed the grain boundaries of the polycrystalline CVD graphene as expected, with very low densities of discoloured (oxidised) regions.

In many cases, graphene samples of a specific size are required. For the standard transfer method, a large piece of copper/graphene was held with a tweezers and cut into smaller samples using sharp scissors (step S2). The corresponding failure mode (FM2, RPN = 720) was identified as structural damage due to substrate deformation; see panel FM2:S in Figure 2.5 for photographs. Oxidation resistance tests (as described above for FM1) showed evidence of graphene delamination. To limit the stress on the copper, this step was changed to employ a roller cutter and a self-healing cutting mat (Figure 2.5, FM2:O). Oxidation resistance tests showed significant reductions in delaminated graphene.

Potential failure modes were also identified for the spun-cast PMMA polymer layer. This layer is intended to protect the front-side graphene during the transfer process. However, ageing of the PMMA in anisole solution (failure mode FM4, RPN = 560) can lead to thickness non-uniformity as well as bubbles. Panel FM4:S in Figure 2.5 shows an optical micrograph of a PMMA layer spun-cast onto a graphene/copper foil sample. A macro-scale bubble is evident. These bubbles led to large circular defects similar to those shown in Figure 2.3 a). Non-uniform PMMA films can also cause delamination of graphene, possibly arising from excessive local adhesion between the graphene and the PMMA layer (relative to the graphene-substrate adhesion). Process improvements for this step involved careful monitoring of the PMMA layer thickness (using profilometry) and use of fresh PMMA in anisole solutions, which led to significant reductions in bubbles and smaller defects.

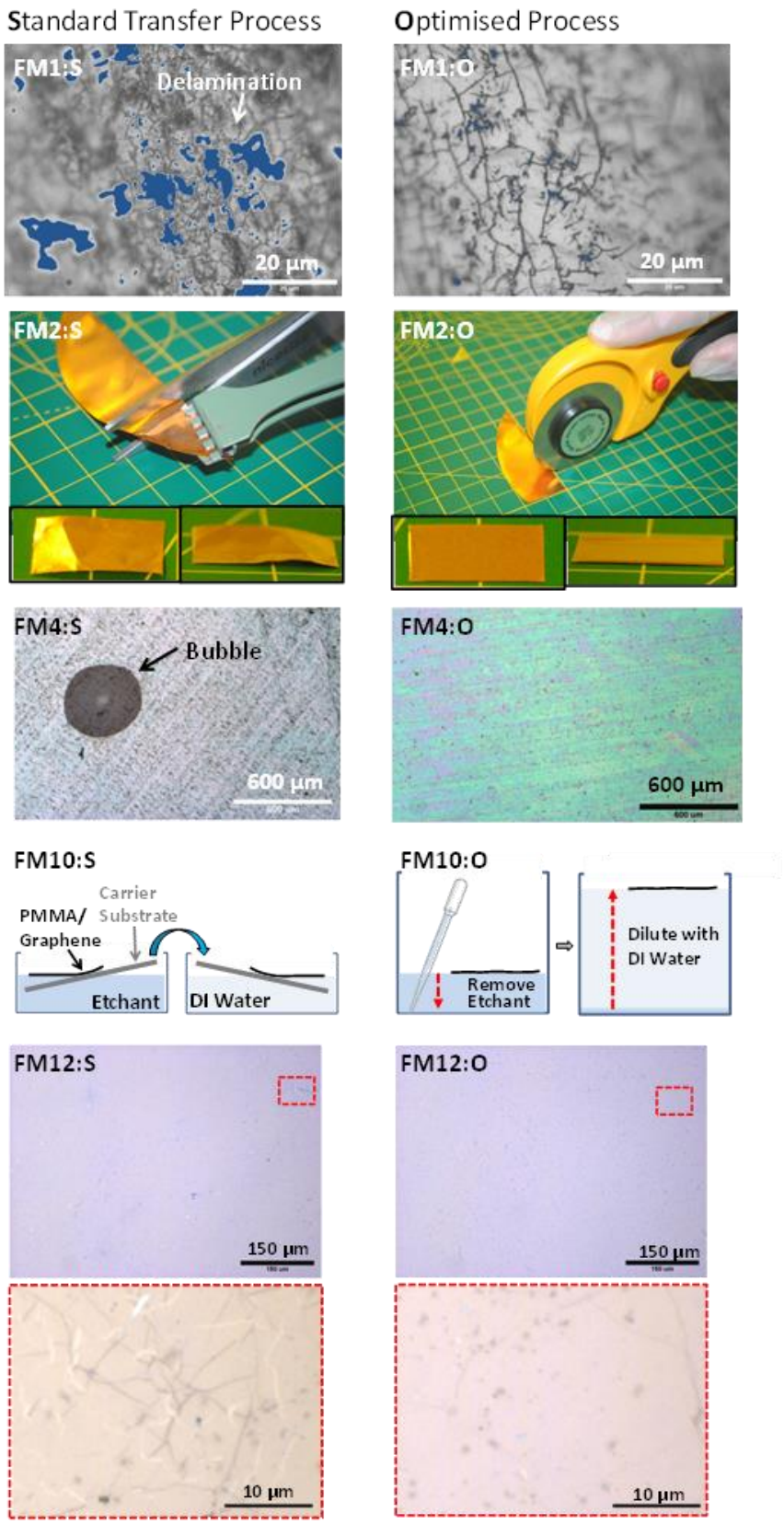


Figure 2.5: Examples of the most significant failure modes for the standard process (left column) and corresponding data (or process improvements) for the optimised transfer process (right column).

The next significant failure mode (FM10, RPN = 630) was identified related to transfer of the PMMA/graphene film to a deionised (DI) water "rinse" bath following wet-etching of the copper foil in an ammonium persulphate solution. A carrier substrate was used to transfer the graphene from the etchant solution to the DI water bath. Initially, most of substrate (~75%) was immersed in the etchant solution at a shallow angle to the horizontal (panel FM10:S in Figure 2.5). One of the edges of the PMMA/graphene film was brought into contact with the surface of the substrate. In some cases, the film was manipulated towards the substrate by gently touching it with a plastic pipette tip. The substrate was slowly removed from the solution. This procedure was operated in reverse to transfer the film into the DI water bath. Several rinse steps were often used to remove the residue from the copper etching step. Potential damage to the graphene could result from manipulation and contact with the carrier substrate during removal from one bath and insertion into another bath; see panel FM10:S in Figure 2.5 [37]. The mitigation strategy developed involved use of a larger etchant bath and also multiple iterations of careful removal of etchant using a pipette and eventual dilution to 1:100 with deionised water (Fig. 5, FM10:O).

Ultimately the graphene has to be transferred to a target substrate using a procedure similar to that depicted in Fig. 2.5 for the removal of the PMMA-coated graphene from the etchant solution. The failure mode identified here (FM11, RPN = 378) included damage from manipulation and also process/moisture residue trapped between the film and the target substrate. Samples were characterised using optical microscopy after hotplate annealing. No measurable improvement was found for this step.

The final significant failure mode (FM12, RPN = 560) related to annealing of the target substrate to melt the PMMA prior to dissolution. Thermal shock resulting from placing the substrate on a pre-heated hotplate can lead to the formation of micron-scale cracks as shown in the optical images in panel FM12:S in Figure 2.5. To mitigate this risk, a slow ramp up to 180°C was introduced. Optical microscopy images acquired after introduction of the improved process step (Fig. 2.5, FM12:O) showed a much lower density of micron-scale cracks.

Figure 2.6 demonstrates the significant improvement in quality of the transferred graphene. Large scale images (e.g., Figure 2.6 a)) reveals uniform transfer with a low density of macro-scale defects. Some damage close to the edge of the transferred layer is evident. Image analysis of cm-scale samples for the optimised process yields a mean defect density of 1.5% (95% Confidence Interval: 0.9 – 2.1%). At micro-scale the defect density is < 1% with a margin of error of 0.04%.

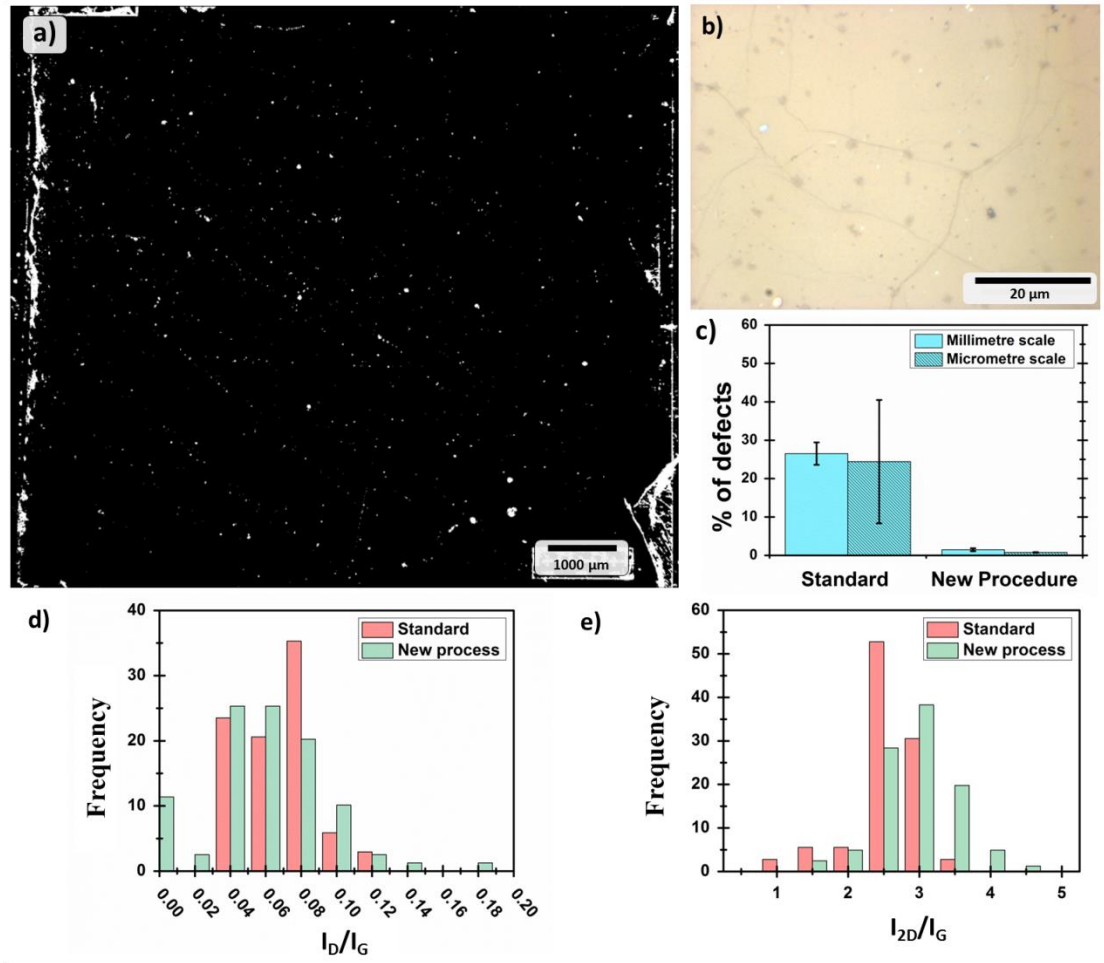


Figure 2.6: a) Post-processed image of transferred graphene (defects highlighted in white) using the FMEA-optimised transfer process. b) High resolution optical image of a region of the sample shown in a. c) Comparison of defect densities for standard and FMEA-optimised processes. d), e) Histograms of the Raman peak ratios I_D/I_G and I_{2D}/I_G respectively for the standard process and the FMEA-optimised process.

Analysis of Raman spectroscopy data comprised Lorentzian peak fits to the G peak (radial breathing mode), 2D peak (sharp two-phonon peak characteristic of monolayer graphene) and the D peak (associated with defects). Figure 6d shows the

distribution of peak intensity values for the defect peak normalised to the G peak intensity (ID/ IG). The distributions are comparable for both processes and with literature data [26]. Thus, the FMEA-optimised process does not introduce any additional nanoscale defects to the transferred graphene. The distribution of I2D/IG values shows a shift towards higher values for the FMEA-optimised process. Reductions in I_{2D}/I_G values have been reported for adsorbate-doped graphene [38]. The higher I_{2D}/I_G values may indicate that the FMEA-optimised process leads to a reduction in surface adsorbates.

Failure Modes and Effects Analysis is a continuous improvement process. Having identified and implemented improvements for individual process steps as outlined above, each step in the new process can then be re-assessed and re-scored for Severity, Likelihood of Occurrence and Method of Detection. Re-calculating the RPN scores and ranking the potential failure modes would enable further systematic process improvement.

2.4 Conclusion

We have demonstrated that Failure Modes and Effects Analysis is a structured, rigorous approach to enable continuous improvement in complex, multi-step processes. Laboratory-scale transfer of cm-scale CVD graphene is an ideal process to demonstrate the benefits of FMEA and provides important learnings for graphene transfer at larger scales.

From the results presented above, it is clear that mechanical contact to graphene remains a significant challenge, both in terms of packaging and also manipulation during processing. This may necessitate use of larger starting samples with sacrificial border regions that would not be used/needed for the eventual application. The uniformity of the protective polymer layer is also critical. Furthermore, it appears that maintaining an "adhesion balance" between the graphene/polymer interface on one hand, and the graphene-substrate interface is of key importance in obtaining high-quality transferred graphene (at high yield) with minimal process residue. Finally, development of reliable, efficient methods for transfer of the protected graphene layer from solution to the ultimate target substrate remains a significant challenge. Further reductions in (sub-micron) contaminants at the graphene-substrate interface and also at the exposed graphene surface (e.g., PMMA residue) could be addressed using a dedicated FMEA study with high resolution electron microscopy/spectroscopy and scanning probe methods.

References

1. Novoselov, K.S., et al., *Electric Field Effect in Atomically Thin Carbon Films.* Science, 2004. **306**(5696): p. 666-669.
2. Castro Neto, A.H., et al., *The electronic properties of graphene.* Reviews of Modern Physics, 2009. **81**(1): p. 109-162.
3. Novoselov, K.S., et al., *Two-dimensional gas of massless Dirac fermions in graphene.* Nature, 2005. **438**(7065): p. 197-200.
4. Kim, K.S., et al., *Large-scale pattern growth of graphene films for stretchable transparent electrodes.* Nature, 2009. **457**(7230): p. 706-710.
5. Bae, S., et al., *Roll-to-roll production of 30-inch graphene films for transparent electrodes.* Nat Nano, 2010. **5**(8): p. 574-578.
6. Lee, C., et al., *Measurement of the Elastic Properties and Intrinsic Strength of Monolayer Graphene.* Science, 2008. **321**(5887): p. 385-388.
7. Bonaccorso, F., et al., *Graphene photonics and optoelectronics.* Nat Photon, 2010. **4**(9): p. 611-622.
8. Gunho, J., et al., *The application of graphene as electrodes in electrical and optical devices.* Nanotechnology, 2012. **23**(11): p. 112001.
9. Novoselov, K.S., et al., *A roadmap for graphene.* Nature, 2012. **490**(7419): p. 192-200.
10. Huang, X., et al., *Graphene-Based Electrodes.* Advanced Materials, 2012. **24**(45): p. 5979-6004.
11. Sukang, B., et al., *Towards industrial applications of graphene electrodes.* Physica Scripta, 2012. **2012**(T146): p. 014024.
12. Muñoz, R. and C. Gómez-Aleixandre, *Review of CVD Synthesis of Graphene.* Chemical Vapor Deposition, 2013. **19**(10-11-12): p. 297-322.
13. Li, X., L. Colombo, and R.S. Ruoff, *Synthesis of Graphene Films on Copper Foils by Chemical Vapor Deposition.* Advanced Materials, 2016. **28**(29): p. 6247-6252.

14. Seah, C.-M., S.-P. Chai, and A.R. Mohamed, *Mechanisms of graphene growth by chemical vapour deposition on transition metals.* Carbon, 2014. **70**: p. 1-21.
15. Kang, J., et al., *Graphene transfer: key for applications.* Nanoscale, 2012. **4**(18): p. 5527-5537.
16. Deokar, G., et al., *Towards high quality CVD graphene growth and transfer.* Carbon, 2015. **89**: p. 82-92.
17. Zaretski, A.V. and D.J. Lipomi, *Processes for non-destructive transfer of graphene: widening the bottleneck for industrial scale production.* Nanoscale, 2015. **7**(22): p. 9963-9969.
18. Liang, X., et al., *Toward Clean and Crackless Transfer of Graphene.* ACS Nano, 2011. **5**(11): p. 9144-9153.
19. Kang, J., et al., *Efficient Transfer of Large-Area Graphene Films onto Rigid Substrates by Hot Pressing.* ACS Nano, 2012. **6**(6): p. 5360-5365.
20. Juang, Z.-Y., et al., *Graphene synthesis by chemical vapor deposition and transfer by a roll-to-roll process.* Carbon, 2010. **48**(11): p. 3169-3174.
21. Borin Barin, G., et al., *Optimized graphene transfer: Influence of polymethylmethacrylate (PMMA) layer concentration and baking time on graphene final performance.* Carbon, 2015. **84**: p. 82-90.
22. Wu, Z.T., et al., *The influence of chemical solvents on the properties of CVD graphene.* Journal of Raman Spectroscopy, 2015. **46**(1): p. 21-24.
23. Suk, J.W., et al., *Transfer of CVD-Grown Monolayer Graphene onto Arbitrary Substrates.* ACS Nano, 2011. **5**(9): p. 6916-6924.
24. Yang, X., et al., *Clean and efficient transfer of CVD-grown graphene by electrochemical etching of metal substrate.* Journal of Electroanalytical Chemistry, 2013. **688**: p. 243-248.
25. Hallam, T., et al., *Strain, Bubbles, Dirt, and Folds: A Study of Graphene Polymer-Assisted Transfer.* Advanced Materials Interfaces, 2014. **1**(6): p. 1400115-n/a.
26. Chen, Y., X.-L. Gong, and J.-G. Gai, *Progress and Challenges in Transfer of Large-Area Graphene Films.* Advanced Science, 2016. **3**(8): p. 1500343-n/a.

27. Hong, J.-Y., et al., *A Rational Strategy for Graphene Transfer on Substrates with Rough Features.* Advanced Materials, 2016. **28**(12): p. 2382-2392.
28. Scipioni, A., et al., *FMEA methodology design, implementation and integration with HACCP system in a food company.* Food Control, 2002. **13**(8): p. 495-501.
29. *Surface vehicle recommended practice*. April 1997: Draft proposal from the SAE J1739 Main Working Committee.
30. Stamatis, D.H., *Failure mode and effect analysis: FMEA from theory to execution*. 1995, New York: ASQC Quality Press.
31. Arabian-Hoseynabadi, H., H. Oraee, and P.J. Tavner, *Failure Modes and Effects Analysis (FMEA) for wind turbines.* International Journal of Electrical Power & Energy Systems, 2010. **32**(7): p. 817-824.
32. Xu, K., et al., *Fuzzy assessment of FMEA for engine systems.* Reliability Engineering & System Safety, 2002. **75**(1): p. 17-29.
33. Rhee, S.J. and K. Ishii, *Using cost based FMEA to enhance reliability and serviceability.* Advanced Engineering Informatics, 2003. **17**(3–4): p. 179-188.
34. Blake, P., et al., *Making graphene visible.* Applied Physics Letters, 2007. **91**(6): p. 063124.
35. Teng, S.H. and S.Y. Ho, *Failure mode and effects analysis: An integrated approach for product design and process control.* International Journal of Quality & Reliability Management, 1996. **13**(5): p. 8-26.
36. Boscá, A., et al., *Automatic graphene transfer system for improved material quality and efficiency.* Scientific Reports, 2016. **6**: p. 21676.
37. Jia, C., et al., *Direct Optical Characterization of Graphene Growth and Domains on Growth Substrates.* Scientific Reports, 2012. **2**: p. 707.
38. Long, B., et al., *Non-Covalent Functionalization of Graphene Using Self-Assembly of Alkane-Amines.* Advanced Functional Materials, 2012. **22**(4): p. 717-725.

Chapter 3: Hybrid electrode consisting of metal mesh and CVD graphene to use as transparent heater

The aim is to determine the performance of hybrid electrodes made of pentagonal mesh and CVD graphene on flexible substrates for future applications. The electrical and optical characteristics were investigated for two flexible substrates.

3.1 Introduction

To date transparent heaters have been mostly used for defrosting and defogging purposes in cars and aircraft [1, 2]. However, additional applications such as thermochromic devices for smart windows [3, 4] and pixelated heating displays [5, 6] have been making their entry. As for the transparent electrodes, transparent heaters are mainly fabricated from Indium-doped Tin Oxide (ITO). The growing need for ITO lead to a growing exploitation of indium and experts predict that the quantity of indium that will be required to answer the demand will be greater than what can be offered [7].

	Hybrid	**Shape**	**Mesh dimension Linewidth/pitch**	**Metal thickness**	**T%**	**Rs**	**Heater ?**
T. Qiu [8]	Cr/Au + RGO	Square	5/50 µm	5/20 nm 5/30 nm 5/40 nm 5/50 nm	80 %	18 Ω/□	no
T. Goa [9]	Ti/Ag + CVD	Hexagon	10/200 µm 10/300 µm 5/200 µm	0.6-1 µm	94 %	0.6 Ω/□	no
Y. Zhu [10]	Ti/Au Al/Cu Al + CVD	Square	10/100 µm 5/200 µm	5/100 nm	70 - 91 %	3-60 Ω/□	no
J. Kang & Y. Janga [11]	Ag NP + CVD	Square	10/150 µm 10/250 µm 10/500 µm 10/750 µm	500 nm	78 – 92 %	4-30 Ω/□	yes

Table 3.1: Example of hybrid of metal mesh and graphene available in the literature

Such a scenario would negatively impact the depending market. Therefore, much effort has been gathered to offer alternatives to ITO. Hybrids consisting of metal meshes and graphene is one of the alternatives that have been studied. The addition of CVD graphene on top of a metal mesh was reported with many potential advantages including the creation of a uniform interface with other layers, the possibility to decrease the Water Vapour Transmission Rate (WVTR) and the Oxygen Transmission Rate (OTR) value of the complete electrodes [12] and finally the advantage to decrease power consumption and improve the temperature distribution of the heating metal mesh [11]. The hybrid concept was already used for standard transparent electrodes by T. Qiu [8], T. Goa [9] and Y. Zhu [10]. The TCE offered sheet resistance < 50 Ω/□ for a given transparency > 80% at 550 nm. A transparent heater was even proposed and studied by J. Kang and Y. Janga [11]. Unfortunately, the classic square shape was the main geometry used for the mesh. Such geometry offers limited mechanical flexibility, a major drawback for future applications.

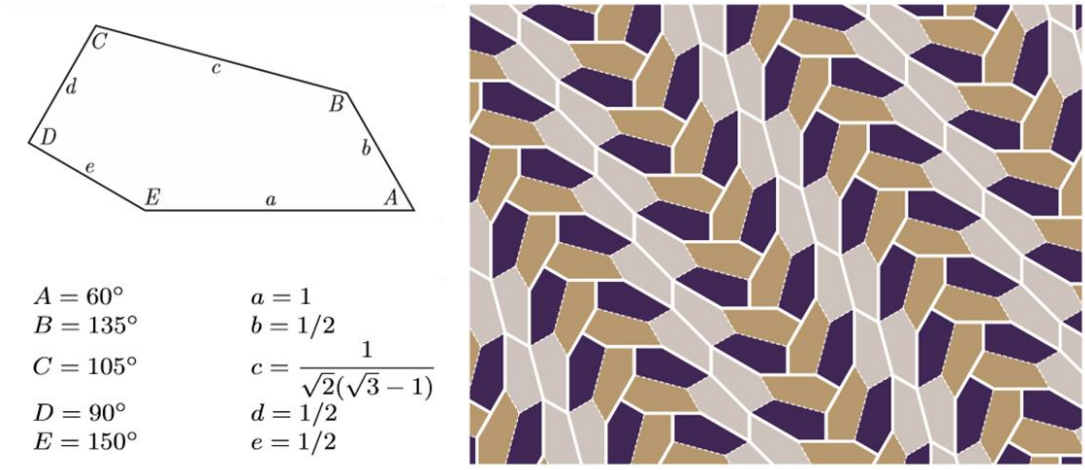


Figure 3.1: Pentagonal mesh developed by Casey Mann [13].

To address this issue two solutions are available: changing the mesh geometry to dissipate strain during bending and using metals with high ductility. Much geometry was investigated in literature from which the pentagonal mesh presented in figure 3.1. The work presented by Daniel Lordan in his thesis included the fabrication of this pentagonal mesh using platinum [14]. The mesh combines both solutions: the use of geometry capable to sustain high stress level and the use of one of the most

"flexible" metals. The transparent heater recorded a thermal resistivity of 213-258 °C.cm^{-2}/W and a transparency of 73 to 91% (without substrate). Finally the stability of the electrical characteristics post bending test confirmed the flexibility of the electrodes [14]. The work presented in this chapter employed the pentagonal mesh to use in a hybrid of metal mesh and CVD graphene. A combination of titanium and gold was used for the meshes instead of platinum to keep the cost of the final transparent heater down. Additionally, gold has a lower bulk resistivity than platinum (1.8 μΩ.cm versus 11 μΩ.cm). Efforts were focused on the thermal performance, electrical characteristics and transparency of the electrode. As the final aim of the device is to be flexible, the devices were fabricated on top of two types of flexible substrates: Polyethylene terephthalate (PET) and Polyethylene naphthalate (PEN). Both substrates are found in literature and have similar properties. Due to their polymeric nature, both films have very good tensile strength and are good electrical insulators. They were also designed to be chemically resistant and, to a certain extent, thermally stable. Finally, they both have a transparency > 80%. The main differences between PET and PEN reside in their optical and thermal properties as well as their surface roughness. Optically, PET (transparency: 88%, Haze: 3%) has a better transparency and haze than PEN (transparency: 82%, Haze: 14%). On the other hand, PET has a glass transition temperature of 110°C, less than the value for PEN 155°C. PEN also has a smoother surface (PEN Ra 11 to 13 nm < PET Ra 19 to 22 nm) which is appropriate for graphene. The comparison was based on the properties displayed by the supplier Teijin DuPont Films™. The two substrates have strong assets and therefore both were investigated.

3.2 Experimental method

3.2.1 Substrate preparation

The substrates -supplied by Teijin DuPont Films™- were cut to size and cleaned prior to any fabrication steps. The samples were dipped in acetone, IPA and DI water then dried with a nitrogen gun.

3.2.2 Fabrication of the hybrid electrode: metal mesh & CVD graphene

The fabrication of the metal mesh involves conventional UV lithography. The resist is deposited and patterned under UV light using a contact mask, the metals are evaporated and finally the resist and excess metals are removed (Lift off). Note that challenges reside in the transparent and flexible nature of the substrate. The process was done by Niall Kelly in the block C cleanroom at Tyndall.

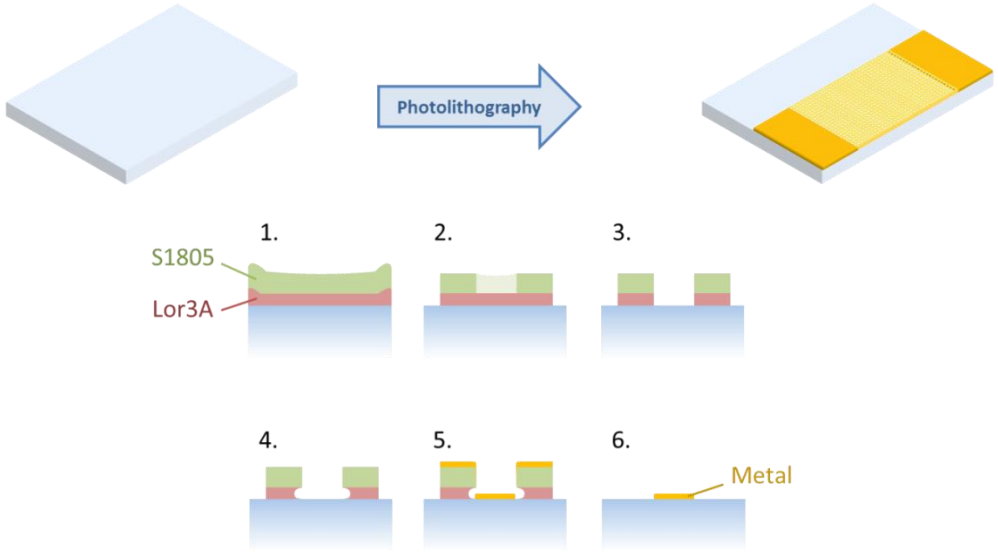


Figure 3.2: Schematic of the metal mesh fabrication process including the photolithography process.

Definition of the pattern using photolithography

The sample surface was first dehydrated to allow a better adhesion of the resist. The wafers were heated for 2 minutes on a hotplate at 120°C.

Two different types of resist were then deposited with a spin coater:

- LOR3A that forms a 300nm layer of pre-exposed resist. Its purpose is to facilitate the formation of undercuts and therefore an easier lift off.
- S1805, a 500nm layer of UV sensitive resist. It allows the drawing of patterns by exposing selected area to UV light.

The programme used on the spin coater is the same for each step:

- 10s at 500 rpm
- 60s at 4000 rpm

Each layer of resist was baked on a hotplate post deposition. The LOR3A layer was baked for 5 minutes at 170°C and S1805 was baked for 2 minutes at 115°C. The edges of the wafer were then cleaned using a tissue soaked with acetone.

The wafers were exposed to UV light (350 to 450 nm) through the mask NTG-M051. The mask was developed with the help of Richard Murphy to facilitate the fabrication of large numbers of samples. As seen in figure 3.3, the mask also includes design for the transfer of graphene only. Each type of samples was designed with 4 additional test grids to allow 4 probes measurements.

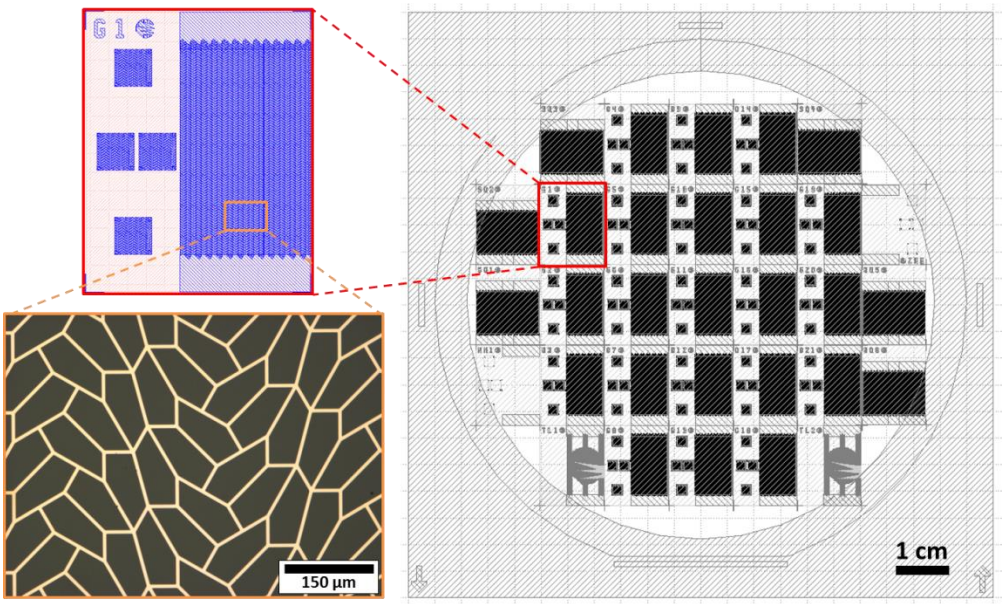


Figure 3.3: NTG-M051 mask with focus on the sample used in this chapter. The design of the sample is visible in the red inset. The main device is composed of 2 electrodes and 11 mm x 7 mm rectangle of mesh. The test grids are 2 x 2 mm square of mesh. Finally an optical image of the pentagonal meshes fabricated is visible is the orange inset.

Only the section exposed through the mask develops during the next stage, yielding the patterns of the future metal contact. The exposure was made with the SUSS MA6 contact aligner and the resolution expected is at least 0.5 µm. The exposure time used for the sample was 4 seconds.

The wafers were then immersed in MF319 for 20 seconds to develop the pattern. The reaction was stopped with a DI water bath and the resist stack was baked a last time at 120ºC for 5 minutes. The samples were heated to solidify the top resist properly to ensure the success of the lift off. It was necessary to avoid the deformation of the resist during the creation of the undercut or when exposed to the vacuum during the metal evaporation.

MF319 was used a second time to develop the layer of LOR3A more deeply. As LOR3A resist is pre-exposed to UV light, the development of the resist is not limited by the mask pattern. Cavities called undercut are then formed under the S1805 layer. The undercuts are essential to insure a split between the metals of the contacts (in the pattern) and the excess metals (on top of the resist). No undercut lead to a continuous layer of metals, which will not be removed during a lift off or would rip everything off.

Evaporation of the metal to create the grid and electrodes

The evaporation was made using a Temescal ebeam evaporator. Two layers of metals were successively evaporated. First, a thin layer of titanium (≈ 10 nm) was evaporated to act as an adhesion layer between the metal of choice and the substrate. Then 50 nm of gold was evaporated.

Final step: the lift off

The samples were immersed in a bath of R1165 at 70°C then left to cool overnight. Wrinkles should appear at the surface of the excess metals. Patience is key in this step. Rushing the process would have an impact on the quality of the final product. Once the excess resist and metals “lifted off” the surface, the samples are introduced into a second R1165 bath at 60 ºC. This last step ensures the removal of any residual resist that could affect future use of the samples. Samples were finally

rinsed in acetone, isopropanol and DI water and each sample was cut and optically verified.

Transfer of CVD Graphene on top of the Grid substrate:

The CVD graphene was transferred using the protocol developed in Chapter 02. The challenges of the transfer resided in the 3D nature of the substrate as humidity can stay trapped in the area between graphene and the grid. Risk of friction and therefore mechanical defects also need to be considered when the graphene/PMMA stack is running over the edge of the substrate.

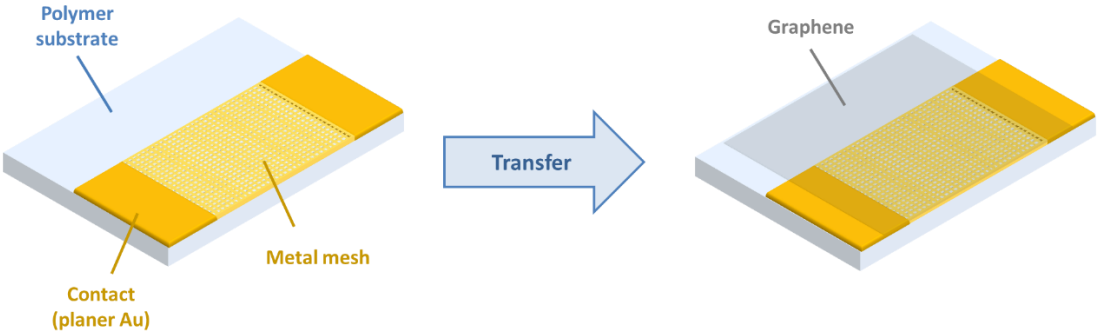


Figure 3.4: Schematic of the evolution of the hybrid electrode pre- and post-transfer.

The transparent and flexible electrodes were fabricated using photolithography for the metal layer and the transfer developed in Chapter 2 for CVD graphene. The metallic layer was patterned using the mask NTG-M051.

3.2.2 Electrical characterisation of the hybrid device

The electrical measurements were made using a 2-terminal probe method for the main device and 4-terminal probe method for the testing grids. The measurements were made at room temperature using an Agilent E5270B parameter analyser interfaced to a LakeShore Desert TTPX probe station (10 mV – 200 mV bias voltage range). The resistance and sheet resistance of the devices were determined using the Van der Pauw method.

The four probe methods could not be used for the main device because of the large contacts covering two of the mesh edges. These large contacts were needed for the thermal characterisation of the device.

3.2.3 Transparency characterisation

The optical characterisation of the devices was made with a Perkin Elmer Lambda 950. The transparency measurement includes the evaluation of the transmission from 300 to 800 nm wavelength range. Measurements were made with air reference and substrate reference. The transparency was then averaged from 450 to 800 nm.

3.2.4 Thermal characterisation: set up and measurements Type 1 & 2

The circuit represented in figure 3.5 was used for the thermal measurements. The sample was connected through crocodile clips to a DC power source. A multi-meter was also inserted in the circuit to record the current during the measurements. The set up was installed in a black box to allow the measurement to be taken in the dark and limits interference due to the light radiation. The thermal measurements were taken with a FLIRONE camera linked to a tablet positioned above the sample at a distance of 4.6 cm. The ambient temperature and the humidity around the set up were also recorded during measurements for the tailoring of the thermal images.

Type 1 measurement:

A voltage was applied to the samples for 90 seconds before taking a thermal image. The experience was repeated with voltages from 2.0 volts to 5.0 volts with 0.5 V steps. Between each change of voltage, the sample was let cool for 40 seconds. A thermal image of the cooled sample was taken 40 seconds after stopping the last voltage.

The different images were then processed with the FLIRONE software and data were extracted for analysis. Figure 3.6 show the specific area for which the data was extracted. The box size was kept identical for all the samples. Temperature histograms were then obtained from the data set.

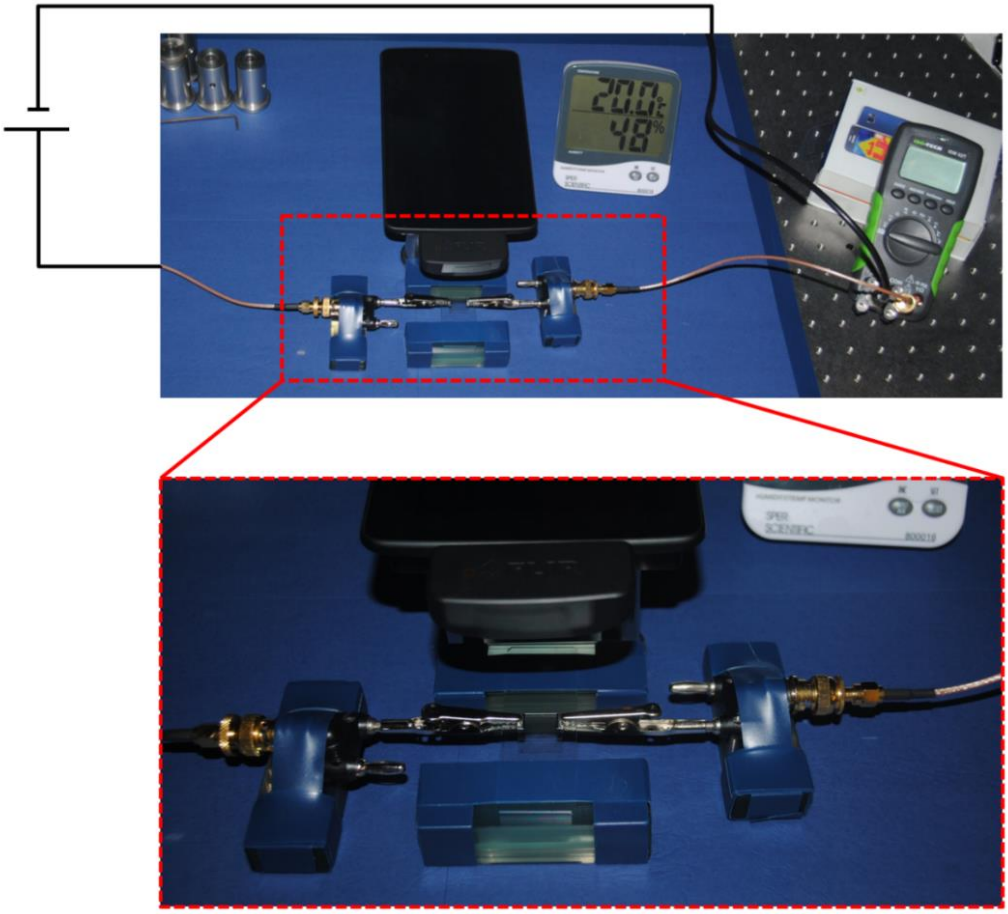


Figure 3.5: Circuit used for the thermal measurements. The FLIRONE camera and the tablet used for the measurements are also visible.

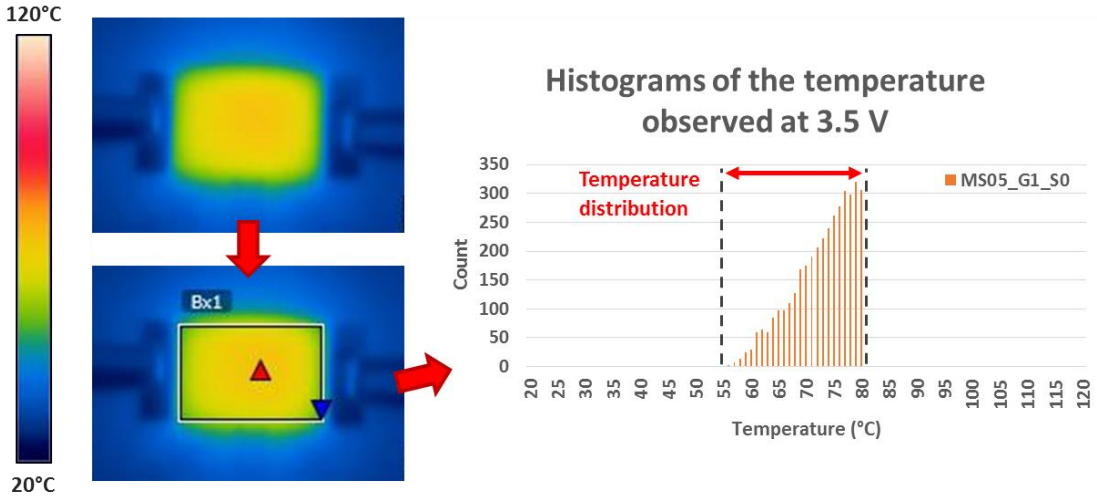


*Figure 3.6: Origin of the temperature histogram. A thermal image is generated using the thermal camera. The image is then processed through the software FLIRone and the area to analyse is selected in a 75*50 pixels box.*

Type 2 measurement:

The samples were installed between 2 crocodile clips and a constant voltage was applied for 90 seconds (heating phase) then turned off (cooling phase). The voltage applied varies from 2.0 to 5.0 volts with steps of 0.5 volts. The temperature of the device (central point) was recorded every 5 seconds through the heating and the cooling phase. The measurement lasted 140 seconds.

3.2.5 SEM characterisation

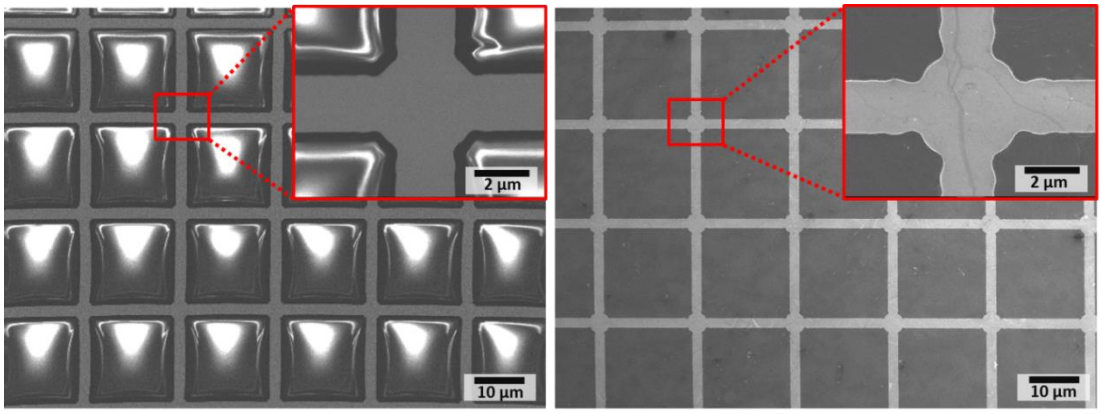


Figure 3.7: SEM characterisation of a sample pre- (left) and post- (right) graphene transfer. Without graphene, the charging due to the substrate makes the observation of defects impossible. Post- transfer, defects created on the mesh can be observed as the focusing is now possible.

It is interesting to note that graphene can be used as a tool for the SEM characterisation of devices on insulating substrates. Substrates such as PET and PEN make SEM characterisation of metal meshes for example very difficult. Charging effects are clearly evident in the areas where the substrate is not covered by metals. In the case of metal mesh, the areas covered by metal are negligible compared to the opened areas explaining why the characterisation is so challenging. When graphene is transferred on top of the metal mesh, the charging effect is cancelled to some extent. Graphene being only one atom thick, the under layer can still be observed.

3.3 Results and discussion

3.3.1 Successful transfer of graphene on 3D substrate

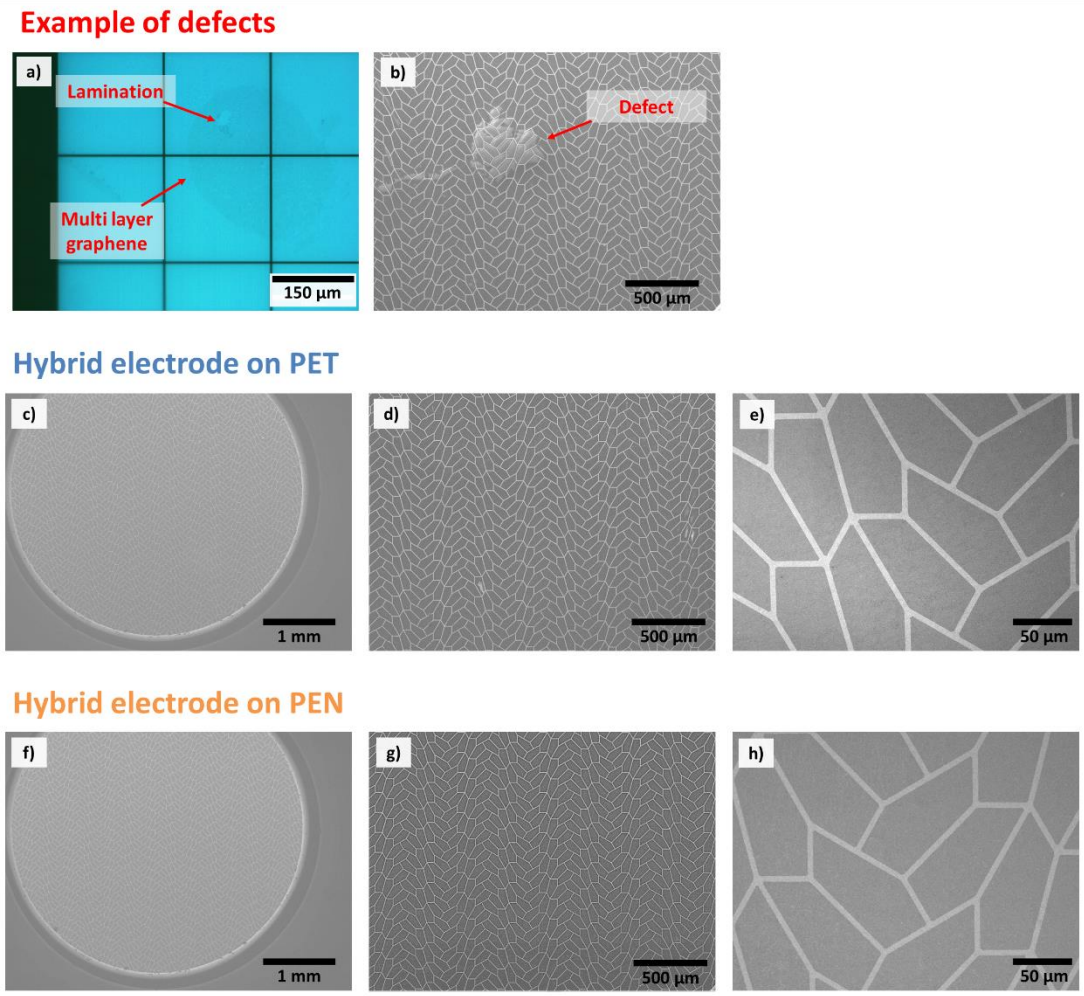


Figure 3.8: a) Epifluorescence optical image under UV light showing an example of defects (excitation wavelength of 390-420 nm and fluorescence collected for wavelength above 450 nm - Zeiss filter set 18). b) SEM image of one of the rare defects found in the electrodes. Defects in the graphene are directly highlighted by the charging due to exposed PET/PEN substrate. c), d) and e) SEM image at different scale of a PET mesh sample post transfer of CVD graphene. f), g) and h) SEM image at different scale of a PEN mesh samples post transfer of CVD graphene.

The 3D nature of the metal grid can be the source of challenges for the transfer of CVD graphene. Due to its transparency, graphene is difficult to characterise on top of transparent substrates such as PEN and PET. Standard optical characterisation

isn't suitable; however by using epifluorescence imaging, large mechanical defects can be detected. As shown in figure 3.8 a) the image obtained is limited and the characterisation could fail to identify micro scale type of defects. This is why the SEM characterisation was favoured. The samples were fully characterised (thermal, electrical etc) before taking the image. As shown in figure 3.8, the transfer of graphene was successful on PET and PEN. There are very few micro and macro scale defects.

3.3.2 Electrical performance of the electrode on PEN vs PET

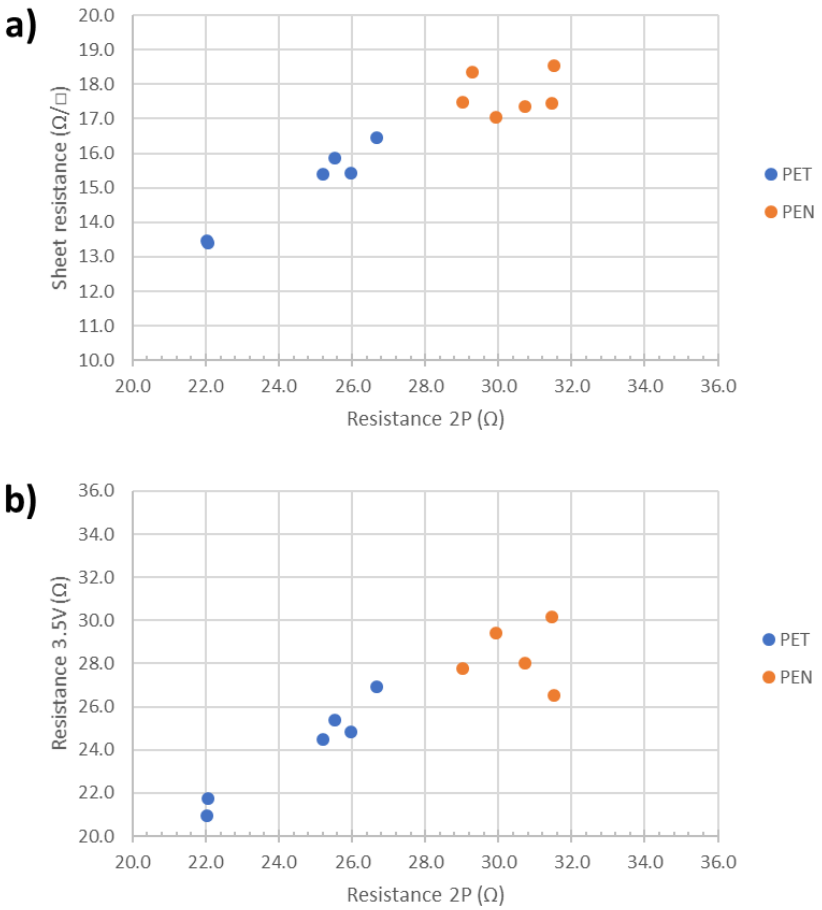


Figure 3.9: a) Sheet resistance in function of the 2-points resistance for meshes on PET and PEN b) Resistance observed at 3.5V during thermal analysis in function of the 2-points resistance

The electrical characterisation of the pentagonal meshes includes results from the sheet resistance – determined from several testing devices- and the resistance of the main device (see figure 3.3). The resistance of the main devices were also

recorded at different voltages during the thermal analysis. In figure 3.9 the different resistances for the as-fabricated electrodes (prior to transfer of graphene) were plotted to assess any resistance variations from one sample to another and highlights any additional resistance due to the set up (particularly in the case of the thermal set up). The linearity of the data in Figure 3.9 a) confirms a negligible resistance from the set up used in the electrical characterisation. The sheet resistance is proportional to the 2-points resistance made using the same equipment. This information validates the use of the 2-points resistance in figure 3.9 b). Note that the data for the PET devices are more linear than the data for the PEN electrodes (figure 3.9 a)). We can estimate that local resistance (resistance over the same sample) is more consistent for the PET samples than the PEN samples. Additionally, the resistance of the meshes on PET substrate varies from 22.0 to 26.7 Ω and the sheet resistance from 13.4 to 16.5 Ω/□. While the variations of resistance in the case of meshes on PEN are more limited with resistance from 29.0 to 31.5 Ω and sheet resistance from 17.0 to 18.4 Ω/□. These differences of variation between meshes on PET and PEN are also observable in figure 3.9 b). Overall, we can estimate that the PET electrodes are locally consistent with variations from device to device. The PEN electrodes however, have local variations but are more consistent from one sample to another.

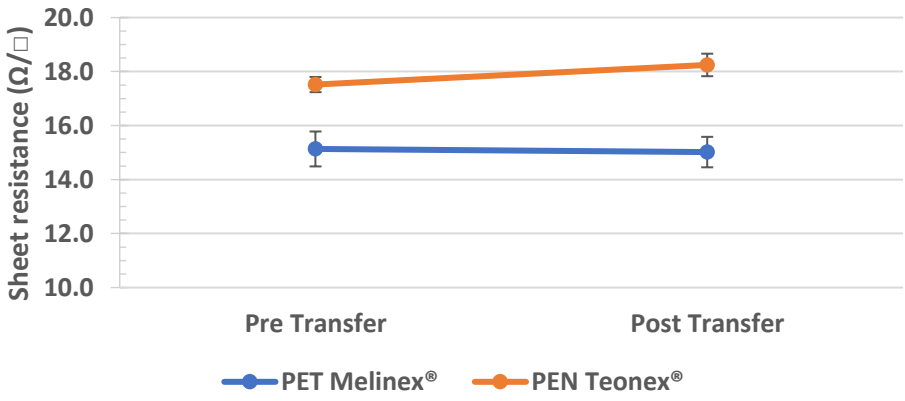


Figure 3.10: Sheet resistance of pentagonal mesh device with and without graphene.

The sheet resistance was estimated at 15.1 Ω/□ for the metal mesh on PET and 17.5 Ω/□ for the metal mesh on PEN (figure 3.10). With standard deviation of 1.2 and 0.6

Ω/□ respectively. After the transfer of CVD graphene on top of the electrode the sheet resistance was 15.0 and 18.2 Ω/□ for the device on PET and PEN.

The difference of sheet resistance between the device on PET and PEN is ≈ 3 Ω/□. This slight difference could be due to the presence of adhesive residues on the surface of PEN. Dupont Teijin Films™ protect the PEN with an additional layer of plastic which must be removed prior use. In our case the protection was removed and the substrates were removed prior to cleaned in 1165, acetone, IPA then DI water before preparing the mesh.

3.3.3 Transparency of the electrodes

The transparency of the pentagonal mesh on both substrates is displayed in figure 3.11. Oscillations are present for both substrates. According to the manufacturer, these interference fringes are due to the adhesive coating on the substrate surface causing internal refraction and reflection. Devices made using PET let pass more than 50% of light from wavelength 326 nm against wavelength 390 nm for the devices made using PEN. Both type of devices registers a transparency superior to 70% in visible light (from 450 to 800 nm). The device on PEN reaches 73.6% transparency with a standard deviation as low as 0.8 %. While the device made with PET reaches 73.8 % transparency with a standard deviation of 1.5 %.

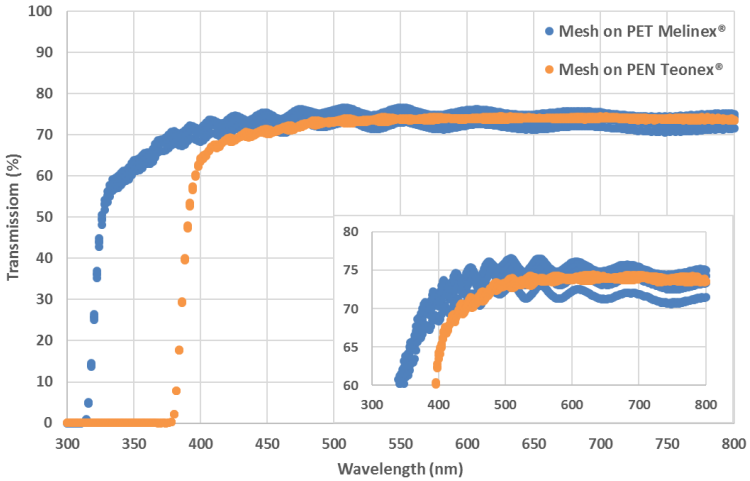


Figure 3.11: Transmission spectra of pentagonal mesh on PET and on PEN. The inset zoom limits the transparency from 60 to 80%.

An approximately 3 % decrease is observed for both types of device after transfer of CVD graphene on the device surface. The finished devices have transparency of 70.9% (standard deviation = 0.8) and 71.2% (standard deviation = 1.4) from 450 to 800 nm for the devices made on PEN and PET respectively. Note that the devices mesh + graphene without substrate have a transparency of 82.9% at 550 nm.

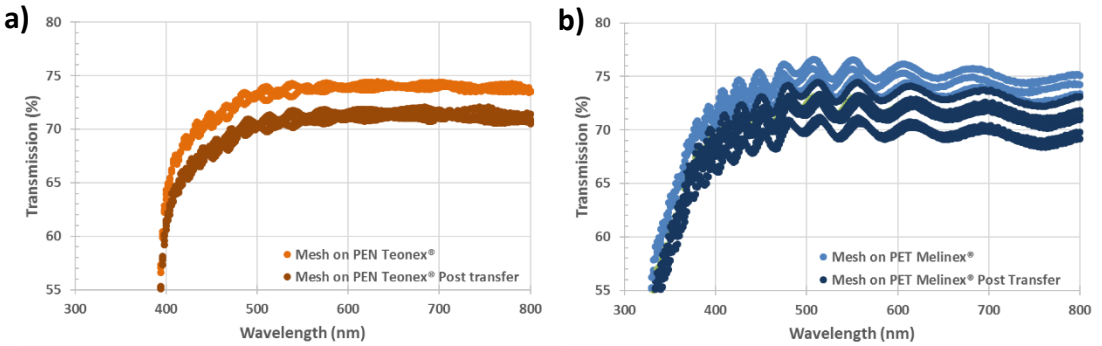


Figure 3.12: Transparency of the pentagonal mesh on a) PET and b) PEN with and without CVD graphene.

3.3.4 Thermal performance of the electrode on PEN vs PET

The thermal characteristic of the devices can be observed in Figure 3.13. Differences in performance are observable between the meshes on PET and the meshes on PEN despite the similarities between the two types of sample. Heaters on PEN reach higher temperature than the heaters on PET. The difference between both type of device is also observable after transfer of CVD graphene. The thermal performance of the device on PET are visibly improved by the addition of the 2D extra layer. However the performance of the device on PEN stays unchanged. When comparing both type of device post transfer, the devices on PET reach higher temperatures than the devices on PEN. Note that the power density should always be taken in consideration when comparing the thermal output of the sample as a change of power density results in a change of temperature. The best way to verify improvement or decrease in the thermal performance of an electrode is to plot the temperature of the device as a function of the power density (figure 3.15). The thermal analysis pre- and post- transfer of graphene for each individual sample is available in appendix S4.

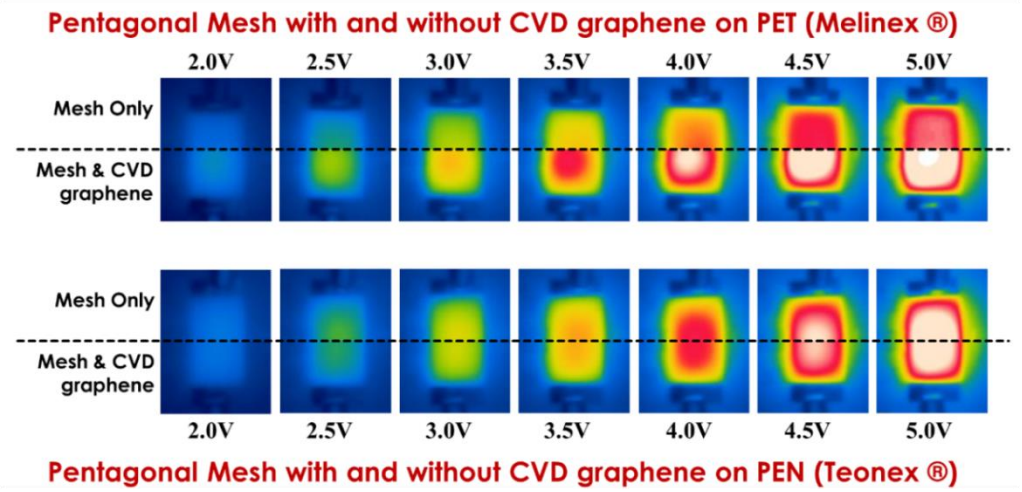


Figure 3.13: Thermal performance of the pentagonal mesh pre- and post- transfer of CVD graphene.

These first observations are confirmed through the histogram analysis. In the case of the device on PET, the histograms extend to higher temperature post transfer. The range of temperature post- transfer is larger than pre- transfer revealing a less homogeneous temperature distribution (see figure 3.14 for example). The histograms of temperature for the device on PEN stays unchanged pre- and post-transfer.

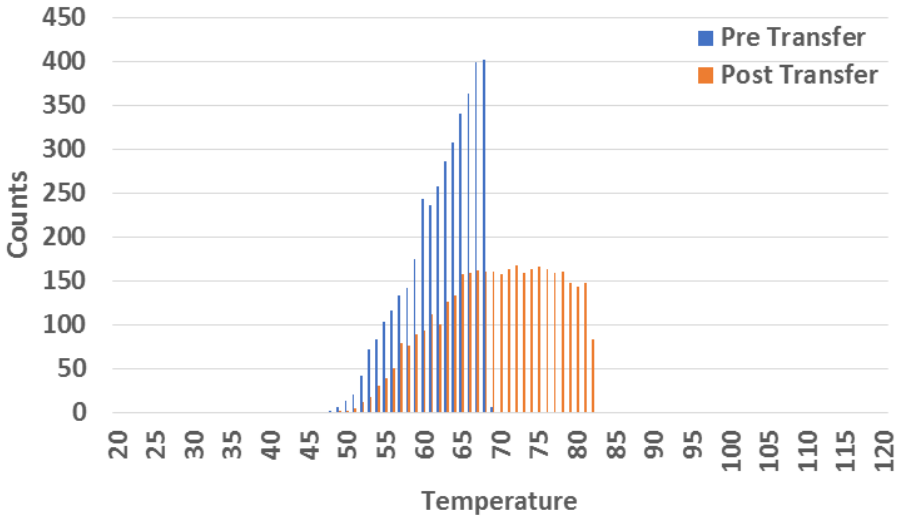


Figure 3.14: Histogram of the temperature of a device on PET with and without CVD graphene. The measurement was made applying a 3.5 voltage in both case.

Finally, figure 3.15 represents the median temperature as a function of the power density. The median temperature was used instead of the mean due to the temperature distribution. As seen in figure 3.13, the temperature histograms present strong skewing. Mean values, in contrast to the median values, are very sensitive to skewing effects and outliers (isolated data out of the distribution range) making them less accurate than the median for asymmetric distributions. The power density was calculated from the current recorded, the voltage applied and the sample size. Due to the camera limitation (accurate measurement up to 120°C), the plots were limited to the data under 4 volts. The measurement made at 4.5 and 5.0 volts both reached higher temperatures.

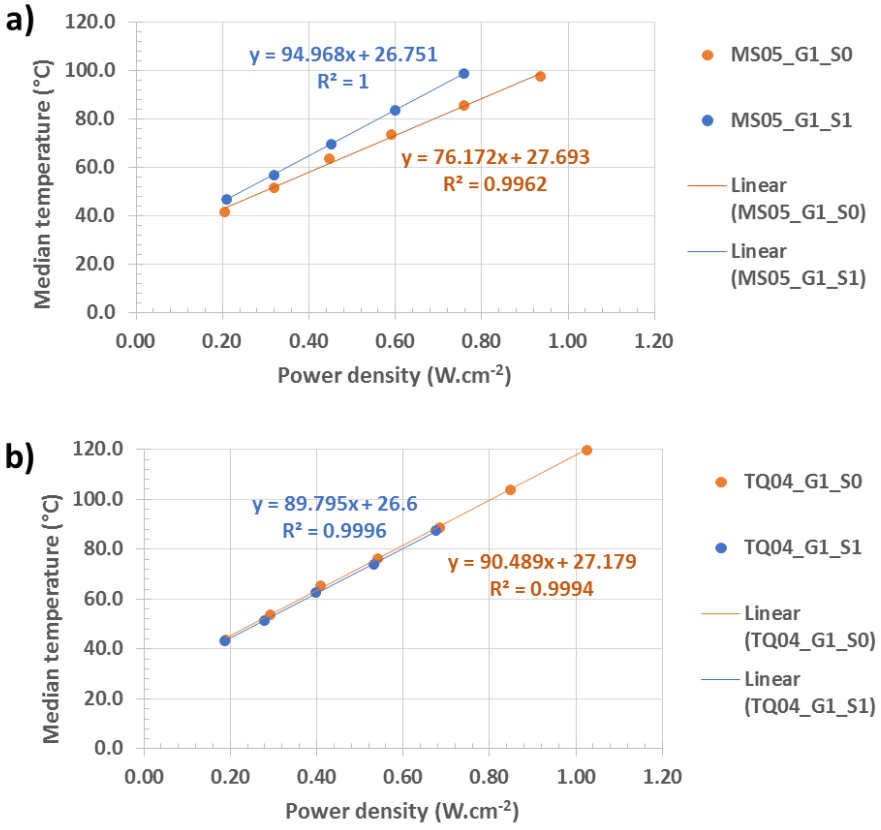


Figure 3.15: Temperature as a function of the power density for a) the pentagonal mesh on PET and b) the pentagonal mesh on PEN pre- (orange) and post- (blue) transfer of CVD graphene.

The slope of the linear fit (dT/dP) represents the thermal resistance of the device. The dT/dP is commonly used to define the heating performance of transparent heaters. Pre- transfer of CVD graphene, the dT/dP of the pentagonal mesh on PEN

(97.3 °C.cm^2.W^{-1} with a standard deviation of 13.6 °C.cm^2.W^{-1}) is higher than the dT/dP of the pentagonal mesh on PET (70.4 °C.cm^2.W^{-1} with a standard deviation of 3.0 °C.cm^2.W^{-1}). This difference can be explained by the difference in thermal diffusivity of the substrate material.

The difference between the two types of electrode decreases with the addition of CVD graphene. The thermal resistance of the device on PEN records a decrease of 2.43 °C.cm^2.W^{-1} with a thermal resistance of 94.9 °C.cm^2.W^{-1} (Std: 5.0 °C.cm^2.W^{-1}), while the device on PET records an increase of 17.1°C.cm^2.W^{-1} with a thermal resistivity of 87.5 °C.cm^2.W^{-1} (Std: 11.90 °C.cm^2.W^{-1}). The standard deviation is also affected. The variations are reduced in the case of the PEN electrode and increase for the PET electrodes.

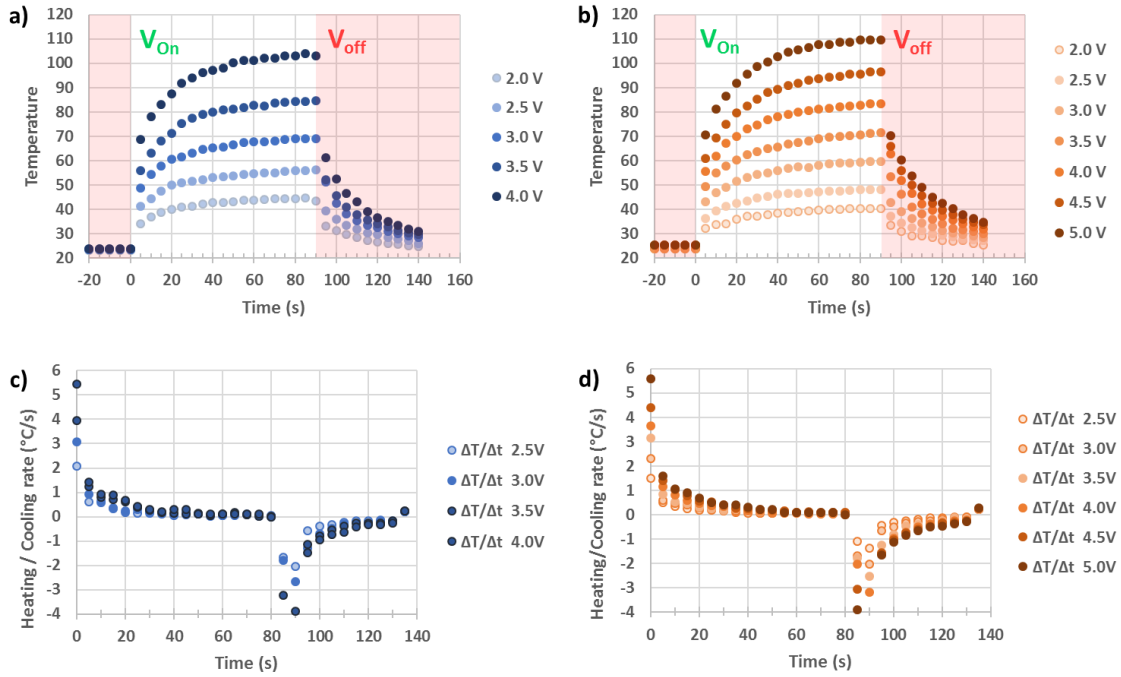


Figure 3.16: a) and b) Time versus temperature profiles at different voltages for pentagonal mesh + CVD graphene on PET and PEN respectively c) and d) Derivative plots of the temperature profile for both type of device.

Figure 3.16 a) and b) show the temperature plot in function of time for both types of device under different DC input voltage. In both case the increase in temperature is very fast and nearly steady state is reached in less than 80 seconds. A response time from 20 to 30 seconds (depending of the voltage applied) is highlighted by the

derivative plot in figure 3.16 c) and d) for both electrodes. As expected the temperature reached at stabilisation state is higher with PET than PEN. For example, the electrode on PET reached a plateau at 103°C for a 4.0 volts input while the electrode on PEN reached a plateau at 83°C.

3.3.5 Figure of merit and comparison to the state of the art alternative

The figure of merit allows the comparaison of transparent electrodes. The figure relies on the sheet resitance and transparency of the material, two key parameters required for optoelectronic technologies. The figure can be calculated by resolving the following equation [15]:

$$T = \frac{1}{\left(1+\frac{188.5}{Rs}\frac{1}{FOM}\right)^2} \quad (3.1)$$

Where T is the transparency of the electrode not including substrate (%), Rs the sheet resistance (Ω/□) and FOM the figure of merit. The following equation was then used to determine the FOM of both type of electrode.

$$FOM = \frac{188.5}{Rs\left(\sqrt{\frac{1}{T}}-1\right)} \quad (3.2)$$

Note that parameters such as haze and method of fabrication are not included in the FOM. Therefor the choice of TCE cannot be exclusively based on this value. Finally, the FOM is not suitable for heaters as the thermal resistivity is also missing. The calculated value should only be used for comparison purpose for the common TCE performance. The pentagonal mesh + CVD graphene on PET yield a figure of merit of 128. The same electrodes on PEN yield 105.

Table 3.2 compares the characteristics of various heaters found in literature with the heaters developed in this chapter. From the flexible electrodes, the hybrid of silver mesh and graphene developed by J. Kang and Y. Janga is one of the best options. The fabrication methods used in this work are compatible for large scale production and the heaters combine a high FOM (356) with high thermal resistivity (379°C.cm^2.W^{-1}). The hybrid developed in this chapter arrived second with a FOM of 128 and a thermal resistivity of 86.6 °C.cm^2.W^{-1}.

Material	FOM	Rs (Ω/□)	T(%)	TR (°C.cm^2.W^{-1})	Response time (s)	Voltage range (V)	T° range (°C)
SWCNT (Glass) [7]	132	54.6	95*	90-137	30-40	10-60	25-47
Ag NWs (PEN) [2]	105	33	~90*		200	3-7	30-47
G (3L) (Glass) [3]	11	403	92*	645	300	6-30	25-110
AuCl3-doped G (glass) [3]	53	66	~90*	645	300	5-12	25-110
RGO (PI) [4]	0.3-0.4	641 – 6079	34-81		120	10-60	30-210
G + Ag grid (PET) [5]	356	4	78	379	30	4	50
Au wire (quartz) [6]	484	5.4	87*	139-189	30-90	2-15	60-600
Hmg (PET)	128	15	82.9*	87.5	20-30	2.0-4.0	47-103
Hmg (PEN)	105	18.2	82.9*	94.9	20-30	2.0-4.0	44-83

FOM: *Figure of merit*

Rs: *Sheet resistance*

T: *Transparency*

TR: *Thermal Resistivity*

CNTs: *Carbon Nanotubes*

Ag NWs: *Silver Nanowire*

G: G*raphene*

T°: Temperature

SWCNT: *Single Walled Carbon Nanotube*

Hmg: *Hybrid of gold pentagonal mesh and CVD graphene*

**Transmission value for the electrodes without substrate*

Table 3.2: Example of transparent and conductive electrodes found in the literature to use as heater. The pentagonal electrodes developed in this chapter are highlighted in green.

3.4 Conclusion

In this chapter, we successfully developed and analysed a new electrode on two substrates commonly used in literature. We also demonstrated that the substrate influences the hybrid's performance as a transparent electrode and as a heater. Lower sheet resistance (Rs (PET): 15.0 Ω/□ < Rs (PEN): 18.2 Ω/□) and higher transparency (T% (PET): 71.2% > T% (PEN): 70.9%) are obtained for the electrodes on PET compared to the same electrode on PEN. These characteristics qualify both electrodes for applications such as displays.

It was also established that graphene improves the performance of pentagonal mesh on PET by increasing the thermal resistivity by 24%, reaching a thermal resistivity of 86.6 °C.cm^2.W^{-1}. The electrode on PEN on the other hand, was reported with a 2.5% decrease post transfer of graphene, reaching a thermal resistivity of 94.7 °C.cm^2.W^{-1}. Both heaters have response time ranging from 20 to 30 seconds.

3.5 References

1. Laforte, J.L., M.A. Allaire, and J. Laflamme, *State-of-the-art on power line de-icing.* Atmospheric Research, 1998. **46**(1): p. 143-158.
2. Thomas, S.K., R.P. Cassoni, and C.D. MacArthur, *Aircraft anti-icing and de-icing techniques and modeling.* Journal of Aircraft, 1996. **33**(5): p. 841-854.
3. Grynning, S., et al., *Windows in the buildings of tomorrow: Energy losers or energy gainers?* Energy and Buildings, 2013. **61**: p. 185-192.
4. *ZEB Final Report*. 2017, The research council of Norway: Trondheim.
5. Cooney, C.G. and B.C. Towe, *A thermopneumatic dispensing micropump.* Sensors and Actuators A: Physical, 2004. **116**(3): p. 519-524.
6. Moschou, D., et al., *All-plastic, low-power, disposable, continuous-flow PCR chip with integrated microheaters for rapid DNA amplification.* Sensors and Actuators B: Chemical, 2014. **199**(Supplement C): p. 470-478.
7. Frenzel, M., et al., *Quantifying the relative availability of high-tech by-product metals – The cases of gallium, germanium and indium.* Resources Policy, 2017. **52**(Supplement C): p. 327-335.
8. Qiu, T., et al., *Hydrogen reduced graphene oxide/metal grid hybrid film: towards high performance transparent conductive electrode for flexible electrochromic devices.* Carbon, 2015. **81**(Supplement C): p. 232-238.
9. Gao, T., et al., *Hierarchical Graphene/Metal Grid Structures for Stable, Flexible Transparent Conductors.* ACS Nano, 2015. **9**(5): p. 5440-5446.
10. Zhu, Y., et al., *Rational Design of Hybrid Graphene Films for High-Performance Transparent Electrodes.* ACS Nano, 2011. **5**(8): p. 6472-6479.
11. Kang, J., et al., *An Ag-grid/graphene hybrid structure for large-scale, transparent, flexible heaters.* Nanoscale, 2015. **7**(15): p. 6567-6573.
12. Choi, K., et al., *Reduced Water Vapor Transmission Rate of Graphene Gas Barrier Films for Flexible Organic Field-Effect Transistors.* ACS Nano, 2015. **9**(6): p. 5818-5824.
13. Mann, C., J. McLoud-Mann, and D. Von Derau, *Convex pentagons that admit i-block transitive tilings.* Geometriae Dedicata, 2017.

14. Lordan, D., et al., *Asymmetric Pentagonal Metal Meshes for Flexible Transparent Electrodes and Heaters.* ACS Applied Materials & Interfaces, 2017. **9**(5): p. 4932-4940.

15. De, S., et al., *Silver Nanowire Networks as Flexible, Transparent, Conducting Films: Extremely High DC to Optical Conductivity Ratios.* ACS Nano, 2009. **3**(7): p. 1767-1774.

Chapter 4: Flexibility and stability of the hybrid electrode to meet application requirements

The aim was to determine if the hybrid pentagonal mesh + CVD graphene was suitable for use in real applications. The stability of the electrode was studied through ON/OFF and long period testing. The flexibility was also investigated through bending test.

4.1 Introduction

The lifetime of applications such as smart windows and pixelated heating display can be influenced by the extensive usage that it undergoes. Most devices are turned ON and OFF thousands of times. Some will be used from a few seconds to a few minutes while others will need to be sustained for hours. Additionally, the flexibility requirements of future applications bring another source of fatigue likely to decrease the life expectancy. Therefore, the electrodes used to build such products need to reach certain standards to guarantee a constant service and a long life span. In this chapter, we apply a first set of testing to assess the stability of the transparent electrodes developed in chapter 3. These preliminary tests should give an overview of the electrodes potential and, if successful, encourage its use for possible applications development. Industrial standard durability and reliability tests are reserved to products at the final stage.

ON/OFF tests can easily be found in the literature [1-4]. The method used is constant over the different examples available. The current is turned ON and OFF repeatedly while the temperature is recorded. The testing of long hour applications is less common in literature but the principle is simple [4]. In this chapter, such a test was adapted from the ON/OFF tests.

Flexibility tests, while very often used, lack standardisation. Testing of transparent electrodes in the literature can be separated in two types: tests with measurement of the resistance pre- and post- multiple bendings [1, 5-7] and tests which evaluate the resistance during bending [8, 9]. The first type of test is often chosen due to its

ease of application. The test does not require specific equipment and the devices are commonly bended manually over a rod of known diameter [10, 11]. The main issue with this method is that during compression the electrode is in direct contact with the bending rode. Additionally, the bending diameter varies from one study to another making any comparison difficult. The second type of test involves the recording of the current during a controlled bending. This method is designed to investigate the device reaction under bending stress. The main disadvantage of this method is the requirement of specific equipment [12, 13].

The practical application of the transparent heaters are often demonstrated through de-icing [2, 14] and thermo-chromic testing [1, 4, 5]. In this chapter, the hybrid was demonstrated in a thermo-chromic device.

4.2 Experimental method

4.2.1 Thermal characterisation: Type 3 & 4 measurements

The type 3 measurement consists of a succession of 10 heating and cooling phases. The heating involved the application of 3.5 volts for 90 seconds. The cooling phase was 50 seconds. The temperature from the centre of the sample was recorded every 10 seconds.

In the type 4 measurement a voltage of 3.5 V was applied to a sample for 10 hours. The temperature at the centre of the sample was recorded every 10 seconds for the first 100 seconds then the temperature was recorded every 10 minutes.

4.2.2 Fatigue verification: Compression and tension bending cycle

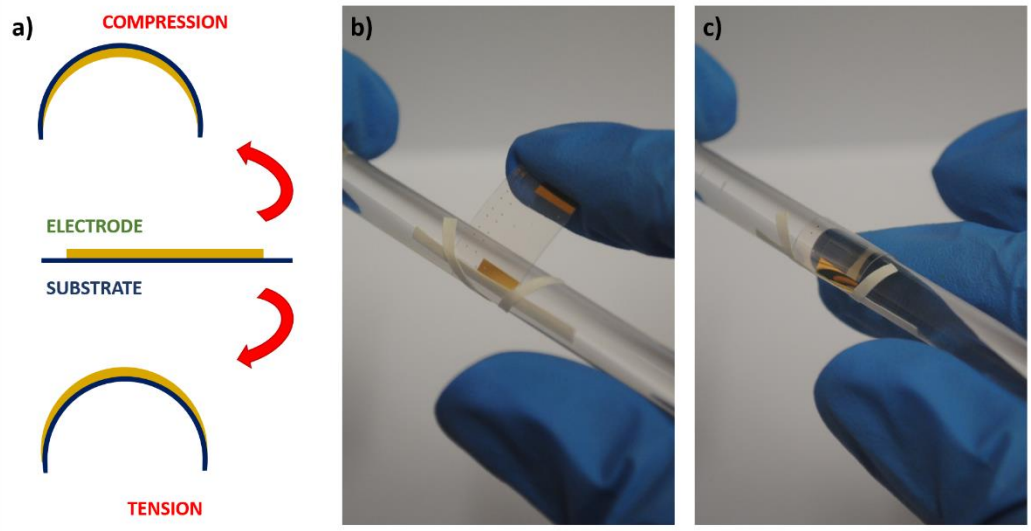


Figure 4.1: a) Schematic of the two types of bending, with the difference being the orientation of the sample. The electrode is inside the bend for the compression test and on the exterior of the bend for the tension test. b) and c) are pictures of a dummy sample at the start and the end of a tension cycle.

To verify the fatigue resistance of the device the samples were bended repetitively 1000 times. They were then electrically, thermally and optically inspected. Two types of bending were applied: Compression and Tension. The tension bending was done using a rod with a 7.6 mm diameter (see figure 4.1). The rod could not be used for the compression bending as the electrode surface would have been in

direct contact with the rod. To limit damage on the graphene surface a system was designed and Ludovic Caro fabricated the bending system using a 3D printer. The developed system is visible in figure 4.2. The bending diameter was also 7.6 mm.

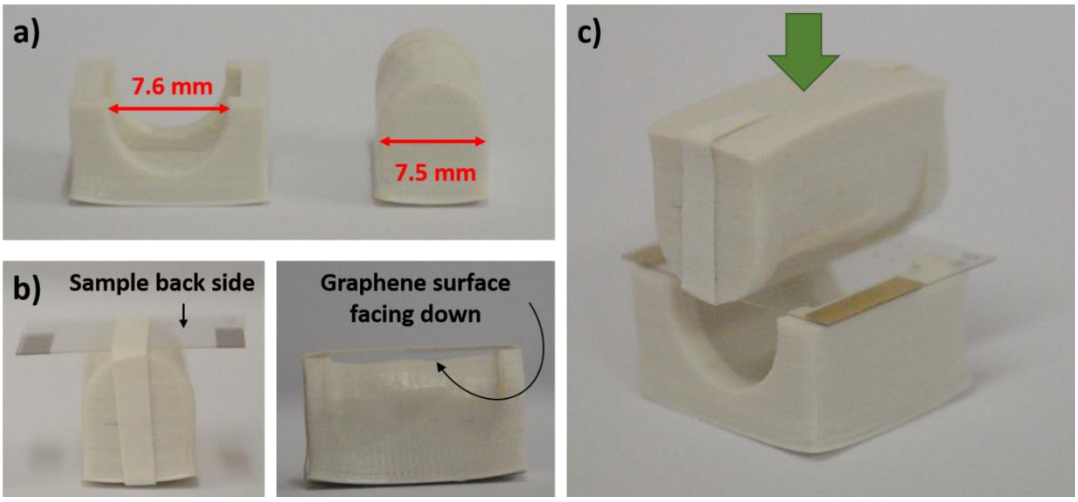


Figure 4.2: a) System used for the compression test. The system is composed of two pieces: the sample holder and the bending piece. b) Two different views of the sample holder mounted with a dummy sample. The first view highlights how the sample was maintained on the sample holder while the second view highlights the space between the sample holder and the sample. c) System prepared for the bending cycle.

4.2.3 Fabrication of the thermochromic device

The thermochromic ink was purchase from SFXC® Special effect and coating.

Preparation of the thermochromic ink:

The ink and the "bending agent" were mixed in equal quantity in a small glass vial. Plastic pipettes were used to estimate the volume of each solution.

Application of the thermochromic ink:

Samples were vertically dipped in the solution then removed at a rate of 0.5 mm/s. The samples were then dried in a pre-heated oven at 50°C for 5 minutes. Once the ink dried, the contact electrodes were cleaned using a tissue soaked in acetone.

4.3 Results and discussion

4.3.1 ON/OFF resistance

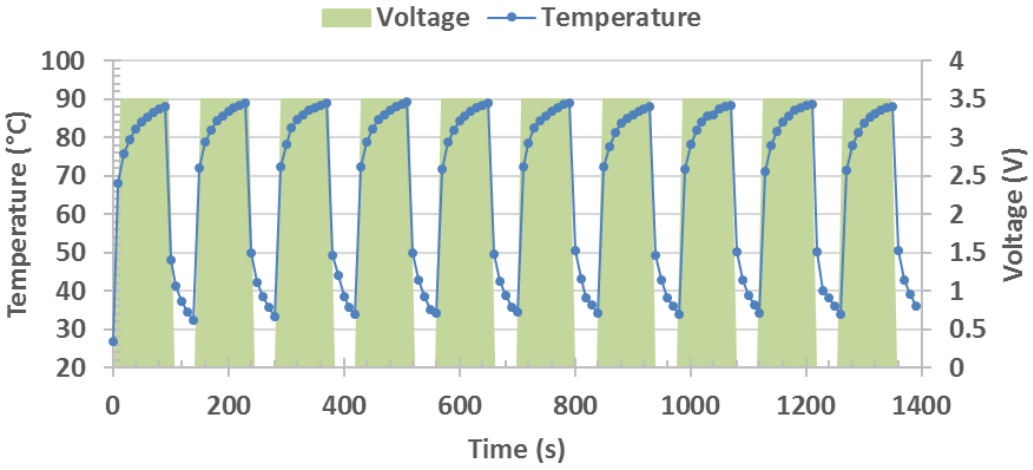


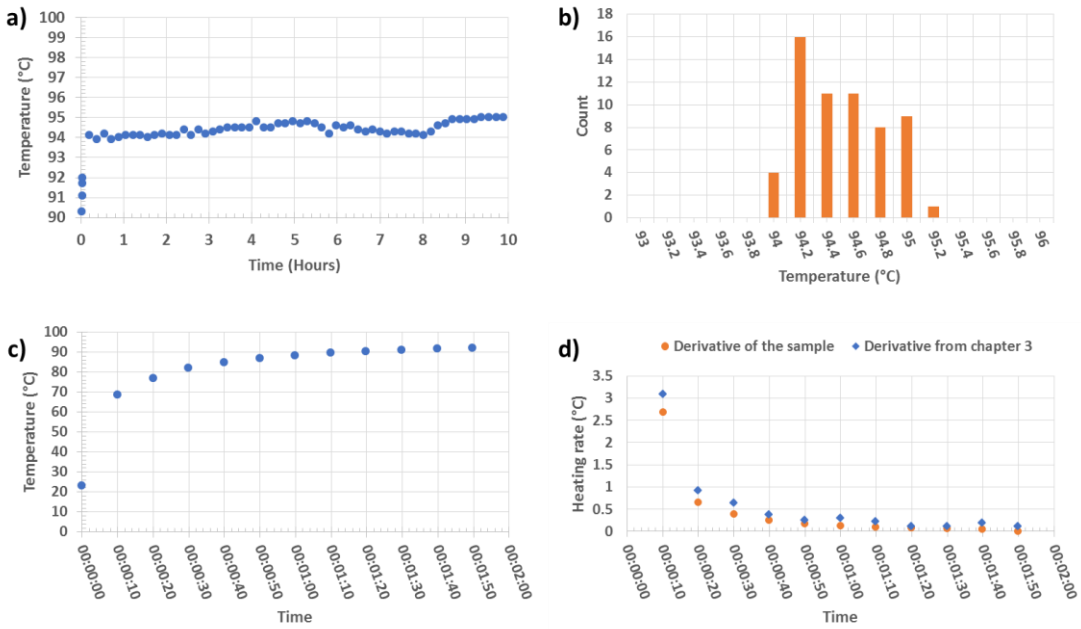
Figure 4.3: Heating and cooling cycle for a hybrid device made of Ti/Au pentagonal mesh and CVD graphene on PET. Heating time of 90 seconds and cooling time of 50 seconds. Experiment done at 3.5 volts.

One of the factors that can influence the life time of an electrode is the repeated ON/OFF associated with the application usage. To mimic this repeated usage, alternating heating and cooling periods were applied. The capacity of the electrode to reproduce the same cycle without variations was then verified. As shown in figure 4.3, the reaction time when switching the voltage ON and OFF is constant in every cycle. Additionally, the maximum temperatures reached are also similar. These observations validate the stability of the hybrid heater.

4.3.2 Long period testing

Many applications such as smart windows require the device to be left on for a few hours. A consistent temperature would need to be maintained throughout this period. The operational stability was investigated by leaving the electrode ON for 10 hours. The results are presented in Figure 4.4. The device reaches the stabilisation state approximately 30 seconds which corresponds to the response time observed in chapter 3 (figure 4.4 c) and d)). While in the stabilisation state, the

temperature varies from 94.0 to 95.2°C. The range of variation is minimal and could be attributed to environmental factors (figure 4.4 b)).



Figures 4.4: Testing for long period usage at 3.0 volts of a Ti/Au pentagonal mesh + CVD graphene electrode on PET (Melinex®). a) Temperature stability over a 10 hours period. b) Histograms of the temperature reached over the 10 hours, excluding the temperature measured during the ramp up period (2 minutes). c) Increase of the temperature after switching the current ON. d) Derivative of the temperature during the warm up period. The data from figure 3.15 c) were included for comparison.

4.3.3 Reliability under bending

To show the mechanical flexibility of the device, tension and compression bending tests were performed. The sheet resistance and the 2 points resistance were monitored between each cycle of 250 bending. No significant change of sheet resistance was observed. Figure 4.5 summarises the total change of sheet resistance pre and post 1000 bending. The gold pentagonal mesh + graphene electrode on PET was not affected by the tension testing. However, the sheet resistance increased slightly post compression tests. The gold pentagonal mesh + graphene electrode on PEN substrate resisted both bending tests (tension and

compression) without change in the sheet resistance. The 2 point resistance follows the same trend as the sheet resistance (figure 4.6)

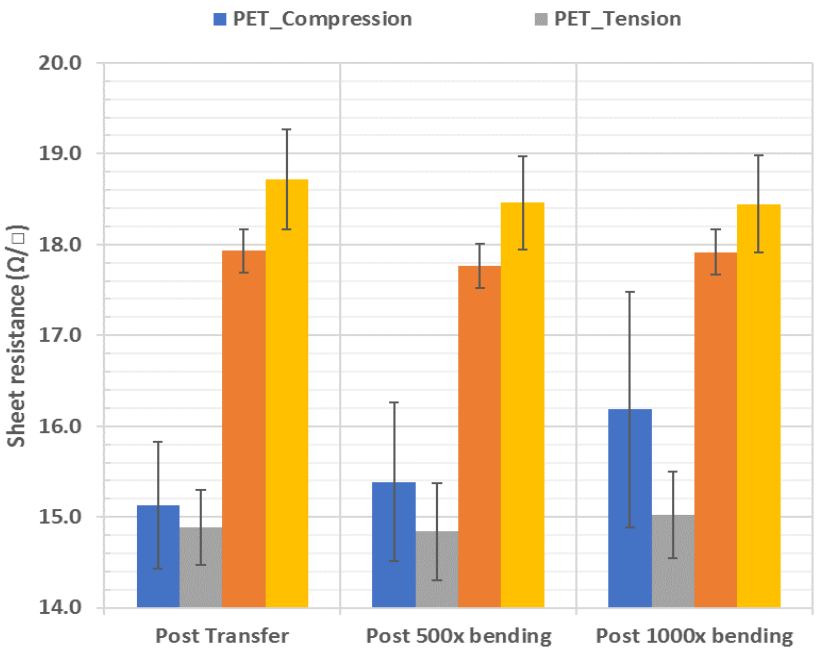


Figure 4.5: Evolution of the sheet resistance after repeated compression or tension cycles for gold pentagonal mesh + graphene on PET and PEN.

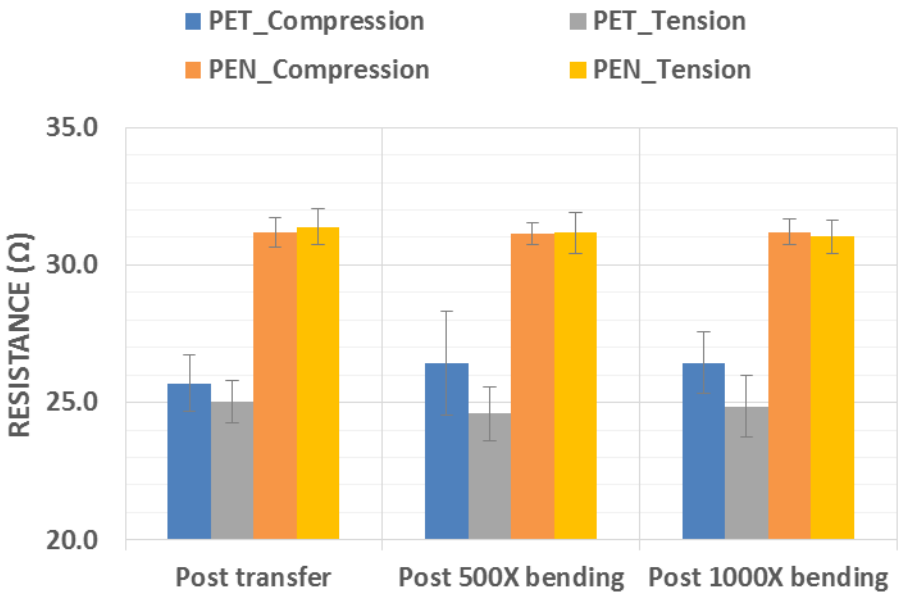


Figure 4.6: Evolution of the 2 point resistance (main device) after repeated compression and tension cycles.

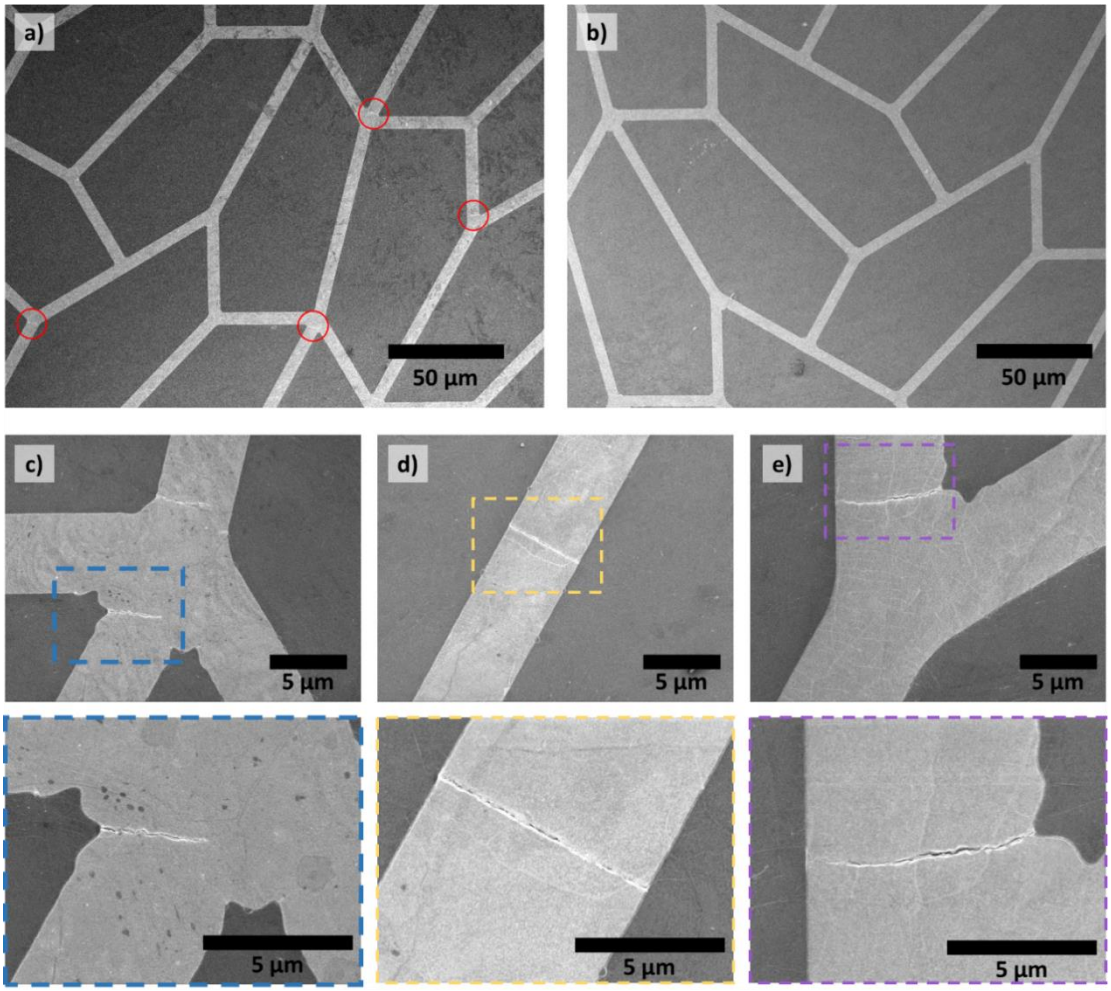


Figure 4.7: SEM images of pentagonal mesh and CVD graphene on a PET substrate that was tested to compression 1000 times a) Typical area with micro breaks present (in red circle) b) typical area free of micro breaks c) d) and e) are higher magnification of microbreaks.

As shown in figure 4.7, microbreaks can be observed post bending tests. These microbreaks are present for devices bended by compression and tension. The breaks are found in minimal quantity and tend to be clustered. Note that despite the breaks present on the metal mesh, graphene is unaffected by the succession of bending (tension or compression) and the breaks in the metal mesh.

4.3.4 Thermo-chromic device

As an example of a practical application of the pentagonal mesh with graphene on PET, chameleon reversible thermo-ink was applied on the sample's surface. Figure 4.8 shows a device before application of the ink and thermal treatment. The experiment was carried out using an input voltage of 3.0 V. The colour change occurred in the first 10 seconds. Unfortunately, the binder used for the ink mix does not change colour, explaining the white colouration still visible after applying the voltage. Once the voltage is off, the device turns back to the initial red colour in less than 5 seconds.

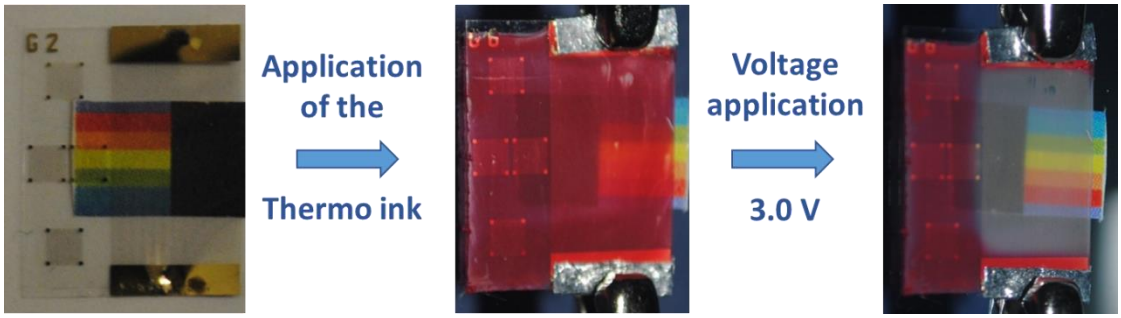


Figure 4.8: Use of the gold pentagonal mesh and graphene electrode (PET) as thermochromics display.

The thermo-ink used for this experiment does not have any prospects in application such as smart windows. The ink has the advantage of being cheap and easy to use, but isn't designed to survive long exposure to UV. This simple experiment however, is a good way to demonstrate a simple thermochromic device and verify its validity before investigating more complex devices.

4.4 Conclusion

We have demonstrated that the electrode made of pentagonal mesh and CVD graphene on PET is stable after repeated ON/OFF switching and long-term conditioning. These results are encouraging and mean that the electrode could satisfy the reliability requirements for industry. We also assessed the flexibility of the electrode on PET and PEN. Minimal changes of resistance were observed in both cases. The presence of microbreaks after 1000 cycles means that the Ti/Au pentagonal mesh and graphene is flexible but not designed for severe treatment. The hybrid can be classified as mildly flexible. Additional testing would be required to validate the hybrid as usable for fully flexible applications. Such characterisation should include a bending test of more than 1000 cycles to verify if the microbreaks are stable or if they would eventually effect the lifetime of the electrodes. Bending test with shorter radius is also to be considered. Additionally, the point of mechanical failure and the recovery capacity of the electrode should also be investigated.

The CVD graphene transferred on top of the mesh resisted the bending tests and did not show damage at the break point. Future work could also consider using a different type of metal mesh.

4.5 References

1. Celle, C., et al., *Highly flexible transparent film heaters based on random networks of silver nanowires.* Nano Research, 2012. **5**(6): p. 427-433.
2. Gupta, R., et al., *Spray Coating of Crack Templates for the Fabrication of Transparent Conductors and Heaters on Flat and Curved Surfaces.* ACS Applied Materials & Interfaces, 2014. **6**(16): p. 13688-13696.
3. Rao, K.D.M. and G.U. Kulkarni, *A highly crystalline single Au wire network as a high temperature transparent heater.* Nanoscale, 2014. **6**(11): p. 5645-5651.
4. Kim, D., et al., *Transparent flexible heater based on hybrid of carbon nanotubes and silver nanowires.* Carbon, 2013. **63**(Supplement C): p. 530-536.
5. Qiu, T., et al., *Hydrogen reduced graphene oxide/metal grid hybrid film: towards high performance transparent conductive electrode for flexible electrochromic devices.* Carbon, 2015. **81**(Supplement C): p. 232-238.
6. Gao, T., et al., *Hierarchical Graphene/Metal Grid Structures for Stable, Flexible Transparent Conductors.* ACS Nano, 2015. **9**(5): p. 5440-5446.
7. Zhu, Y., et al., *Rational Design of Hybrid Graphene Films for High-Performance Transparent Electrodes.* ACS Nano, 2011. **5**(8): p. 6472-6479.
8. Sui, D., et al., *Flexible and Transparent Electrothermal Film Heaters Based on Graphene Materials.* Small, 2011. **7**(22): p. 3186-3192.
9. Kang, J., et al., *An Ag-grid/graphene hybrid structure for large-scale, transparent, flexible heaters.* Nanoscale, 2015. **7**(15): p. 6567-6573.
10. Grego, S., et al., *A method to evaluate mechanical performance of thin transparent films for flexible displays.* Thin Solid Films, 2007. **515**(11): p. 4745-4752.
11. Gleskova, H., S. Wagner, and Z. Suo, *Failure resistance of amorphous silicon transistors under extreme in-plane strain.* Applied Physics Letters, 1999. **75**(19): p. 3011-3013.

12. Grego, S., et al., *Development and evaluation of bend-testing techniques for flexible-display applications.* Journal of the Society for Information Display, 2005. **13**(7): p. 575-581.
13. Gorkhali, S.P., D.R. Cairns, and G.P. Crawford, *Reliability of transparent conducting substrates for rollable displays: A cyclic loading investigation.* Journal of the Society for Information Display, 2004. **12**(1): p. 45-49.
14. Kiruthika, S., R. Gupta, and G.U. Kulkarni, *Large area defrosting windows based on electrothermal heating of highly conducting and transmitting Ag wire mesh.* RSC Advances, 2014. **4**(91): p. 49745-49751.

Chapter 5: Study of the effect of CVD graphene on square metal meshes

The aim was to better understand the contribution of graphene when transferred on top of metal meshes and determine the limitations of CVD graphene for transparent heaters. The electrical, optical and thermal characteristics of different configurations of square mesh with CVD graphene were investigated. The parameters varied were the pitch size (from 40 to 200 µm) and the metal thicknesses (15, 30 and 50 nm of gold on top of 10 nm of titanium).

5.1 Introduction

The addition of CVD graphene on top of metal meshes was reported to offer many potential advantages including a decrease in the power consumption of a device and an improvement in the temperature distribution of the heating metal mesh [1]. However, we reported in chapter 3 that graphene may boost the heating performance of the metal heater by increasing the temperature of the device, with the temperature distribution through the devices being less homogeneous. This result suggests the opposite function of graphene compared to the conclusion raised by J. Kang and Y. Janka. If graphene is to be considered as a valid addition to transparent heaters which include metal meshes, a better understanding of its function is necessary. Are the differences observed due to mesh characteristics or to the graphene itself? Is it possible to determine if graphene will boost the device temperature or ensure a homogeneous temperature distribution? What are the limitations of graphene? If graphene is to really be considered as a viable addition to metal meshes heaters, such questions need to be answered.

The thermal properties of graphene were extensively covered theoretically in the literature, however experimental studies are few due to the challenges associated with the testing of a 2D material [2]. Nevertheless, estimations of the specific heat and the thermal conductivity of graphene can be found in the literature. As

expected, the substrate influences these properties [3, 4]. Defects, edges effects and doping are also expected to limit the thermal conductivity of graphene [2]. To date, most published works focused on suspended graphene and graphene on silicon-based substrates [5-9]. The heat capacity and the thermal conductivity of CVD graphene on PET substrates have not been measured. Additionally, many of the studies are made using nanoribbons and flakes. The combination of the substrate effects and the large size of our samples mean that predicting the graphene contribution is difficult.

The aim of the work presented in this chapter is to investigate the influence of the metal mesh on the graphene contribution. The samples were fabricated using the same process reported in chapter 3. The substrate, the size of the heating device and the graphene layer were also kept identical.

The heating system was simplified by using square meshes. The square mesh has the added bonus of being similar to the geometry used by J. Kang & Y. Janga. Different pitch sizes were used, ranging from 40 µm to 200 µm. The smaller pitch size presents a thermal performance similar to the performance registered with the pentagonal mesh. As for chapters 3 and 4, the mesh was made with titanium and gold. Three metal thicknesses were investigated to evaluate if parameters such as device resistance, temperature reached by the device or simply the pitch size could influence the graphene contribution.

This work can benefit from the work presented by J. Kang & Y. Janga. However, many differences separate the two hybrids:

- The geometry of the meshes. The mesh used in chapter 3 and 4 is a new type of pentagonal mesh designed to minimise resistance variations under mechanical strain. J. Kang & Y. Janga used a standard square mesh. The electrical current is going from an electrode to the second electrode through the straight lines of the mesh. The lines perpendicular to the electrodes only serves as an alternative current path in case of a break in the main mesh lines. In the pentagonal mesh, the current cannot take a straight path. The differences of geometry could result in a different distribution of the heat.

- The mesh fabrication and the metal used. While we favoured a photolithography process followed by the e-beam evaporation of the titanium/gold mesh, J. Kang & Y. Janga used an inkjet printing method to draw the mesh with ink comprising silver nanorods (in triethylene glycol monoethyl ether solvent).
- The transfer of CVD graphene. In chapter 3 and 4, the graphene was transferred on top of the mesh using the transfer developed in chapter 1. J. Kang & Y. Janga transferred the graphene using a hot press method and then fabricated the mesh on top of the graphene. This could influence the different types of contamination encountered and the adhesion between graphene and the other layers of the transparent heater.
- Finally, the structure of the devices. In our case, graphene follows the 3D structure of the mesh on which it was transferred. The graphene/air heat transfer area is dominant followed by the graphene / substrate interface. In J. Kang & Y. Janga case, the graphene is flat and under the mesh meaning that the heat transfer area of the graphene / substrate interface is the dominant interface, followed by graphene / air.

5.2 Experimental methods

5.2.1 Fabrication of the hybrid electrode: metal mesh & CVD graphene

The hybrid electrode, as in chapter 3 and 4, consists of a metal mesh covered by CVD graphene.

The PET substrates were cleaned in R1165, acetone then IPA and DI water prior to fabrication. The metal meshes were fabricated by photolithography using S1805 and LOR3A resist and the mask NTG-M050 (Available in Appendix S6). Square meshes were selected with equal metal width and increasing pitch size (see design B1 to B5 in the Appendix S6). The undercuts were formed using MF309. Three wafers were made, on which three different thickness of metals were evaporated: 10/15, 10/30 and 10/50 nm of titanium and gold. The lift off was made using 1165 and the sample were once more rinsed in acetone, IPA and DI water. The individual samples were cut prior to the transfer of CVD graphene. The transfer used is the method developed in chapter 2.

5.2.2 Thermal characterisation: Type 1 measurement

As in chapter 3, a constant voltage was applied to the samples for 90 seconds before taking a thermal image. The process was repeated with voltages from 2.0 volts to 5.0 volts with 0.5 volt steps. Between each change of voltage, the sample was let to cool for 40 seconds. A thermal image of the cooled sample was taken 40 seconds after the final heating phase.

5.3 Results and discussion

5.3.1 Electrical and transmission characteristics associated with the different variables

The five pitch sizes used in the study are visible in figure 5.1. The difference in metal thickness is not visible through a microscope therefore only the images from the samples with 10/50 nm of titanium/gold meshes were presented. Note that a light colour difference is observable by simple eye inspection for the 10/15 nm thick meshes. They have a titanium tint while the 10/30 and 10/50 nm thick metal meshes have a clear gold colour. The difference in mesh thickness translates to variations in the transparency and resistance of the device.

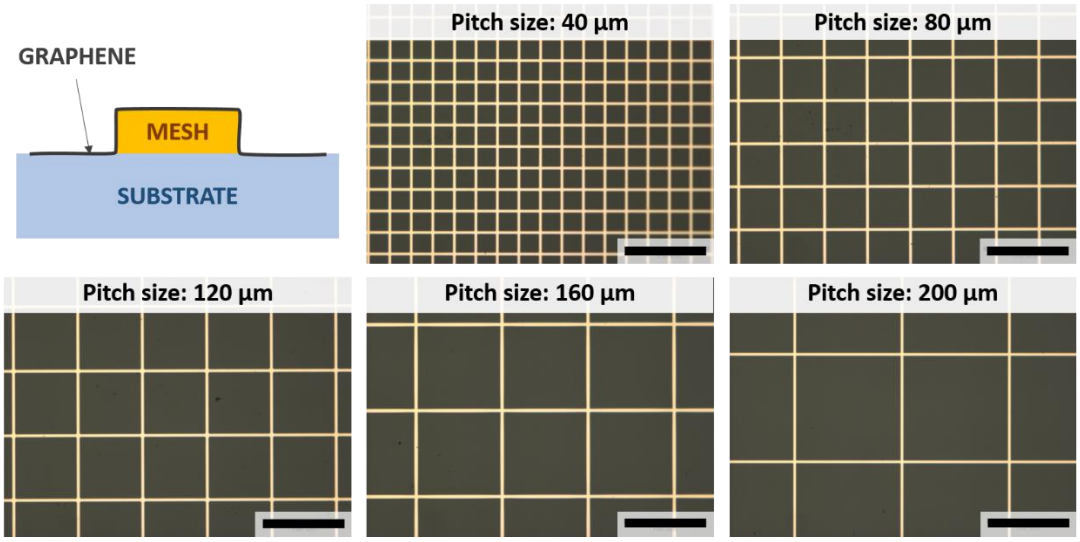


Figure 5.1: Metal mesh/ graphene on PET devices used in the study. The schematic represents the structure of the device. The different pitch sizes used in the study are presented by the microscope images. The CVD graphene is not visible.

The transparency characterisation data are presented in figure 5.2. The comparison of the transmission at 550 nm (Figure 5.2 a)) shows that only the sample made of mesh with lower pitch sizes, such as 40 and 80 µm, are affected by the metal thickness. No differences are observable for the samples with pitch sizes of 120 µm and more. The spectrum in b) c) and d) confirms that the observations (the difference of transparency due to the metal thickness) at 550 nm are roughly

constant from 400 to 800 nm wavelength for pitches ranging from 80 µm to 200 µm. In the case of the 40 µm pitch size, the comparison of the spectrum from 10/15, 10/30 and 10/50 nm thick mesh highlights a strong loss of transparency from 650 nm to 800 nm. A more significant change of transparency was expected for samples with tighter mesh as the increase of the thickness would have a direct impact on the reflection and haze of the sample.

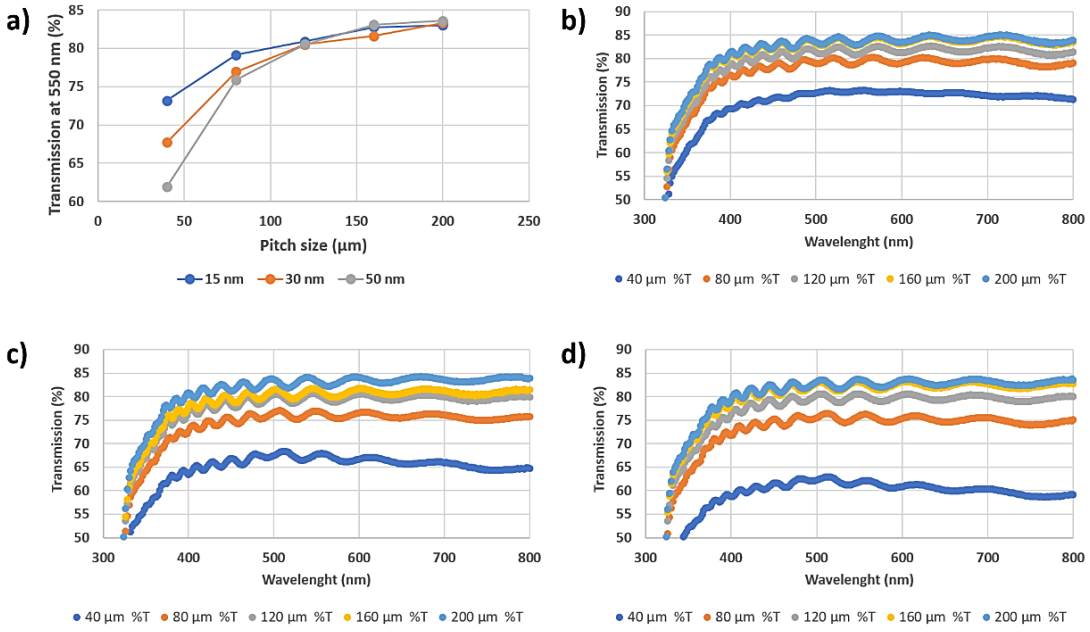


Figure 5.2: Summary of the transparency measurements made from the different hybrid electrodes including the substrate (post graphene transfer). a) Transparency (at 550 nm) as a function of the pitch size of the square meshes. Three different thicknesses of gold were compared: 15, 30 and 50 nm. b) c) and d) Transparency from 300 to 800 nm wavelength of square meshes with 40 to 200 µm pitch size. The spectra are separated depending on the metal thickness: 15, 30 and 50 nm of gold respectively. Note that the fringes observed are due to Fabry-Perot reflection happening in the substrates.

In figure 5.3 a), the sheet resistance of the different metal mesh / graphene hybrids are plotted versus their transparency. As expected, the 10/15 nm meshes present sheet resistances much higher than the samples made of 10/30 and 10/50 nm metal thickness. In figure 5.3 b) The resistance of the testing device (used for thermal characterisation) is compared pre- and post- transfer of graphene. The

addition of graphene increases the resistance of the 10/15 thick meshes and the larger pitch size from the 10/30 nm meshes.

The pentagonal mesh developed in chapter 3 had a sheet resistance of 15.1 Ω/□ and a transparency of 72.1% (at 550 nm wavelength, including the substrate). The transparency and electrical characteristics position the performance of the pentagonal mesh between the performance of the 40 µm and 80 µm pitch size samples made of 10/50 nm of titanium/gold.

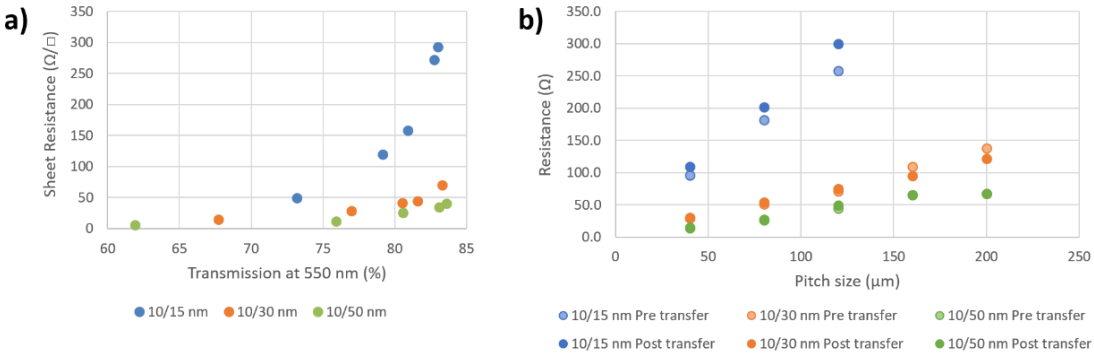


Figure 5.3: a) Sheet resistance in function of the transmission for hybrid made from different thicknesses of metal b) Resistance of the devices used for the thermal characterisation (7 x 11 mm) in function of the pitch size pre- and post- transfer of CVD graphene.

5.3.2 Control of the electrical and thermal characterisation – measurement variables

The variability associated with the measurement set up was investigated before analysing the differences observed between the various samples. As in chapter 3, the sheet resistance was plotted versus the 2 points resistance (figure 5.4 a)). The data are linear and the limited variability observed suggest low variations of the local resistance (resistance over the same sample). Special attention was given to the sample made of 10/30 nm of metals and a pitch size of 160 µm as its 2P resistance did not fit the trend. In figure 5.4 b) the resistance of the testing devices at 3.5 volts was plotted as a function of the 2 points resistance. The linearity of the

data also suggest that the electrical set up used for the thermal measurements are consistent with minimal variability. Note that the sample made from 10/15 nm of metals and a pitch size of 200 µm exhibits a lower resistance at 3.5 V that does not fit the trend.

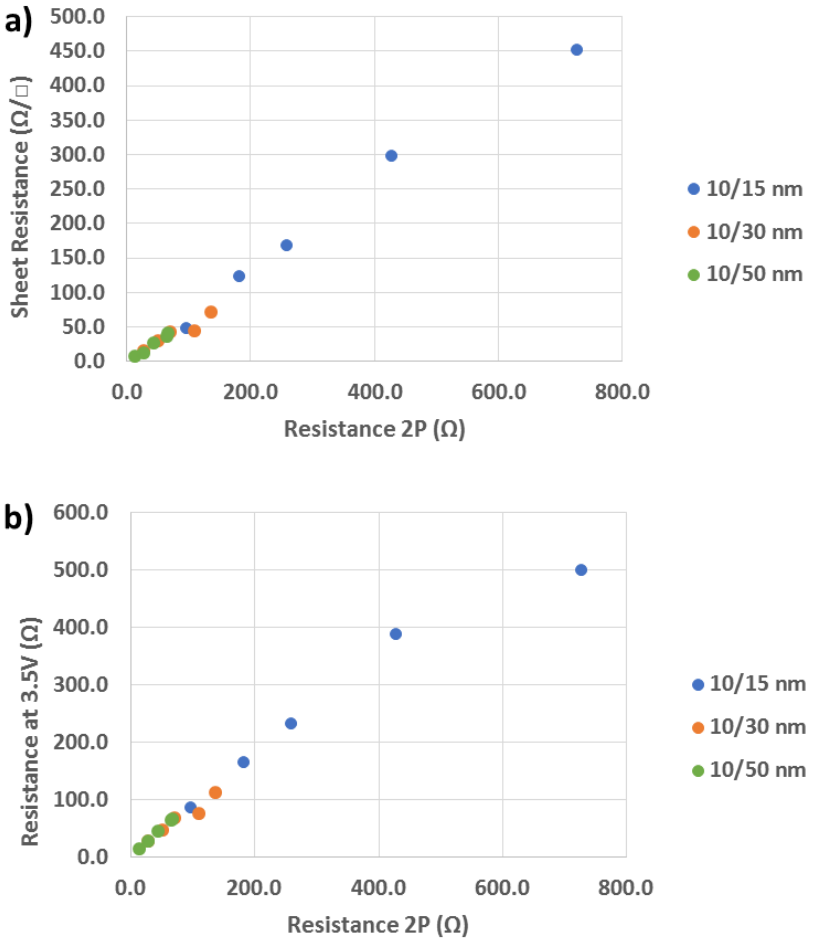


Figure 5.4: a) Sheet resistance in function of the 2-points resistance for 10/15 nm, 10/30 nm and 10/50 nm meshes on PET b) Resistance observed at 3.5V during thermal analysis in function of the 2-points resistance.

In figure 5.5, the thermal images of the various mesh configurations are presented. The following trends were observed:

- At comparable voltage, the heating capacity of the mesh is decreasing when the pitch size is increasing.
- The heating capacity of the meshes is improved when the voltage is increased.

- At comparable pitch size, the heating capacity of the devices is higher for thicker metal thickness.

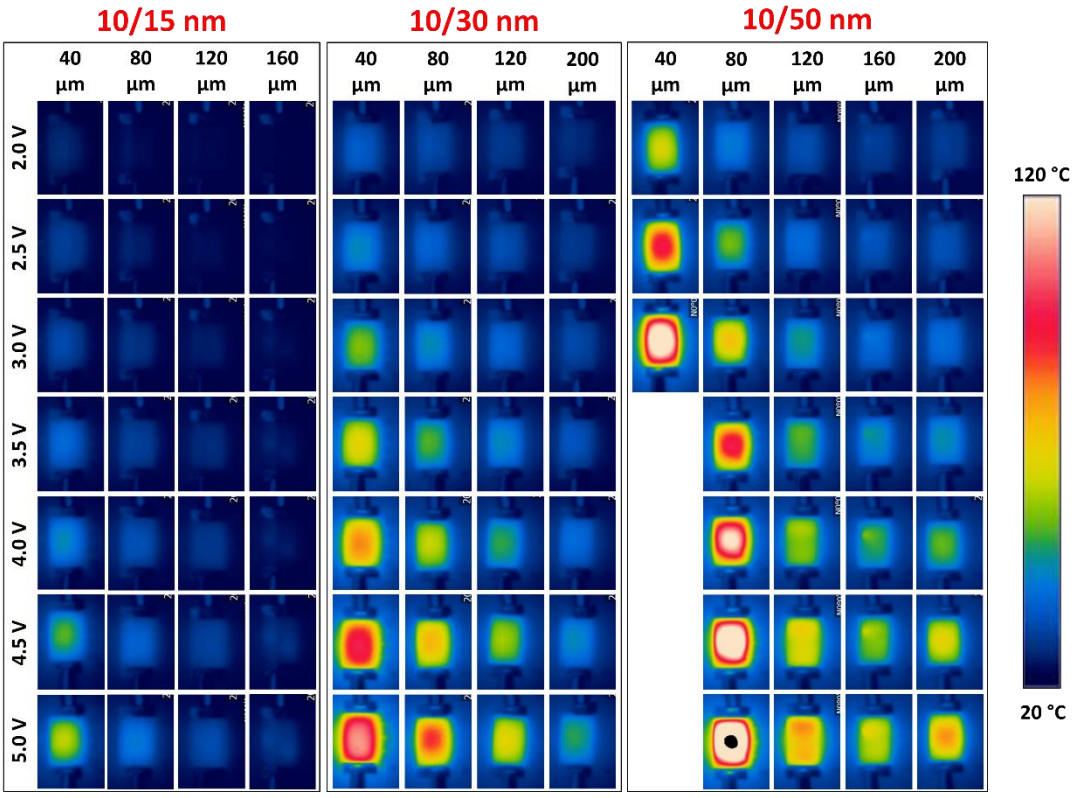


Figure 5.5: Thermal image of the different meshes (no graphene) available at a voltage of 2.0V to 5.0 volts. The samples were categorised in function of the metal thickness and ordered by increasing pitch size. (Thermal images pre- and post-transfer are available in Appendix S8)

Additionally, figure 5.5 draws attention to samples that do not follow the expected trend. For example, the 10/50 nm thick a mesh with 160 µm pitch size reaches a lower temperature than expected. A defect is clearly visible that could explain the results. Figure 5.5 also highlights that the meshes made of 10/15 nm of metal needs to be used with precautions as the higher pitch sizes are close to room temperature.

5.3.3 Observed effects post transfer of CVD graphene

In this section, the focus was on the observed consequences of transferring graphene on top of the meshes. Figure 5.6 presents the thermal outcome (median temperature and the effective range of temperature) as a function of the power

density for each meshes configurations. The use of the power density instead of the voltage indicates whether the change of temperature is due to a change in the electrical performance. The power density was deduced from the applied voltage (2.0 to 5.0 volts), the current was recorded after 90 seconds for a heater dimension of 7 mm x 11 mm.

The first observation that can be made is that the transfer of graphene does have an influence on the thermal properties of the transparent heater.

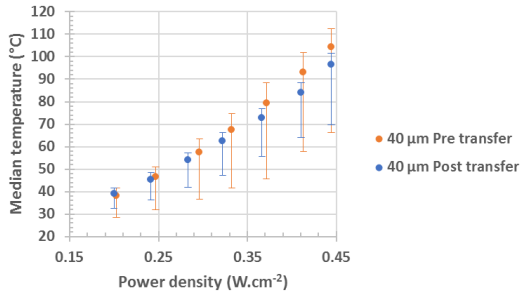
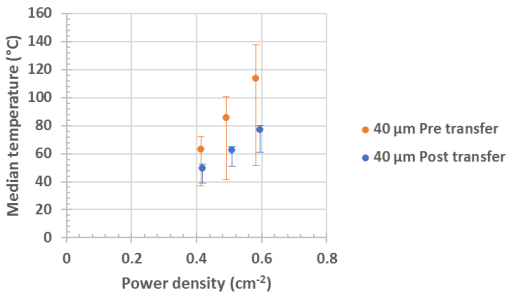
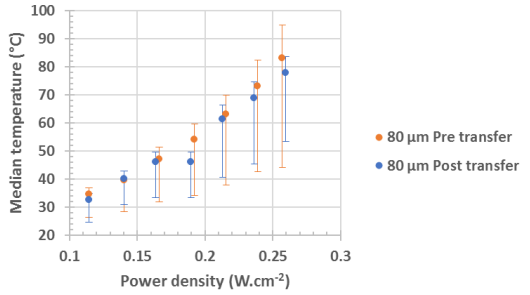
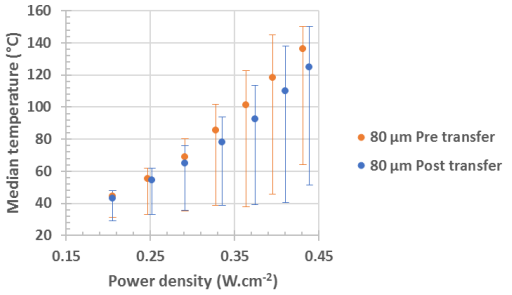
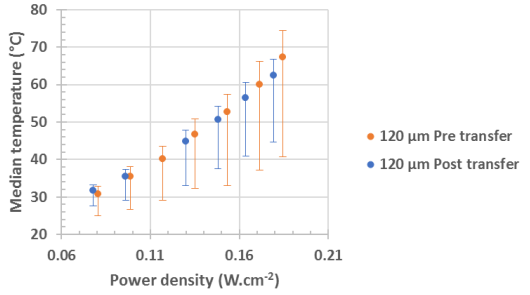
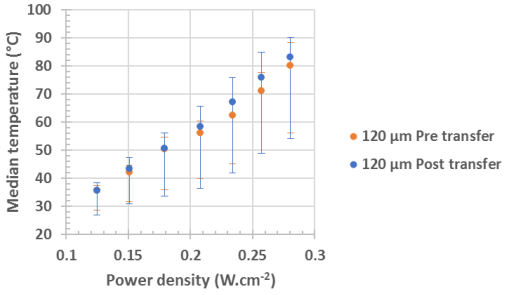
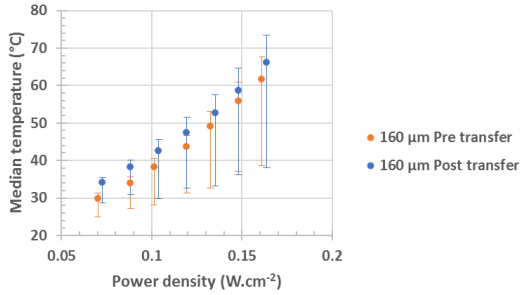
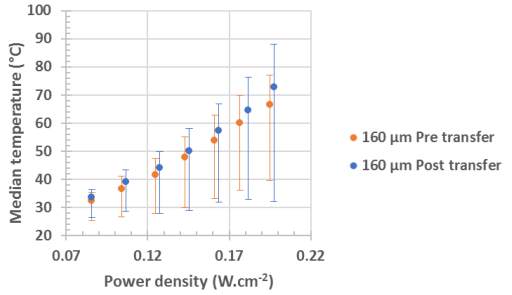
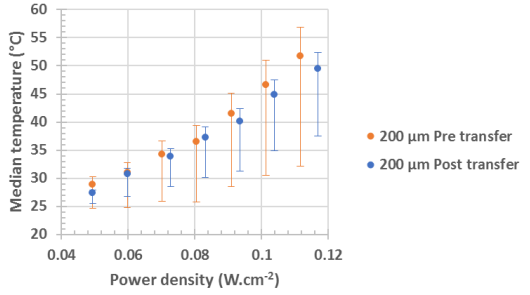
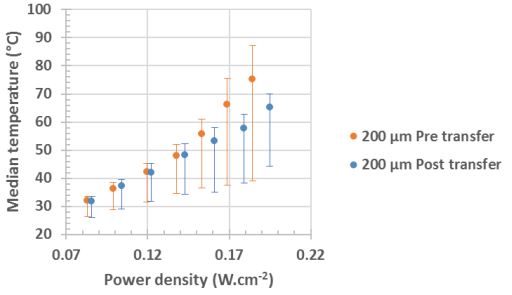
For the meshes with pitch size of 40, 80 and 200 µm (10/30 and 10/50 nm of metals), the given median temperature at a specific power density is lower post transfer. The temperature distribution is also narrower.

The reverse observations are made in the case of the meshes with 120 and 160 µm pitch sizes (10/50 nm of metal).

Finally the 10/30 nm thick meshes with 120 µm pitch size follows the same trend pre- and post- transfer regarding the median temperature. The ranges of temperature were also decreased post- transfer.

Secondly, the increase of the median temperature post- transfer correlates with an increase of the temperature distribution. While the decrease of the median temperature correlates with a decrease of the temperature distribution. In figure 5.7, the temperature distribution was plotted in function of the mean temperature. If the change of distribution was only due to the change of temperature then the slope obtained pre- and post-transfer would be similar. A change of slope would mean that the change of temperature distribution is not only due to the change of temperature. The plotting of each individual samples are available in Appendix S7.

Figure 5.6 (next page): Median temperature (point) and actual spread temperature (bar) in function of the voltage for the different mesh configurations. The actual spread of temperature represent the temperature distribution ranging from the minimum to the maximum temperature. The data pre- transfer of CVD graphene is represented in orange while the data post transfer is in blue. The measurements were stop after 3.0 V in the case of the sample with 40 µm (10/50 nm) as the temperature reached were higher than the thermal camera limitation (120 °C).

	10/30 nm	10/50 nm
40 µm		
80 µm		
120 µm		
160 µm		
200 µm		

In figure 5.7 a), the data which is linear and focused pre- transfer becomes dispersed post- transfer. The ratio temperature distribution / median temperature is also lower post transfer. These observations are not repeated for the samples made of 10/50 nm (figure 5.7 b)).

Finally, the third observation concerns the curve followed by the data. As in chapter 3, the data is expected to form linear trend. The non-linearity observed means that the heat system could be more complex than a simple "generated heat + transfer heat" system.

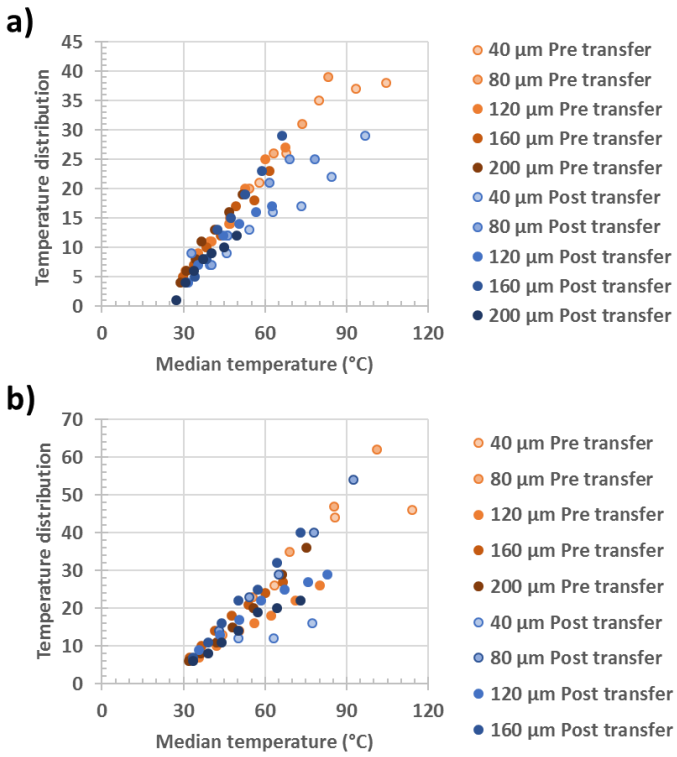


Figure 5.7: Temperature distribution in function of the median temperature grouped in two graphics: a) 10/30 nm and b) 10/50 nm thick meshes. Orange represent the results pre- transfer and blue post transfer.

The decrease observed in some cases confirms the observations made in J. Kang and Y. Janga papers. However, it is important to highlight that this improvement is associated with a decrease of the temperature reached by the heater. These observations can also be observed in J. Kang and Y. Janga's paper but are not mentioned. The similarities between the results found in both pieces of work can at least confirm that the nature of the metal meshes (evaporated metals vs

nanoparticles) and the structure of the device (graphene on top or under the meshes) are not dictating the role of the graphene.

5.3.3 Thermal resistivity and resistance

In this section, we investigate different parameters that could be causing and influencing the temperature difference highlighted in the previous section.

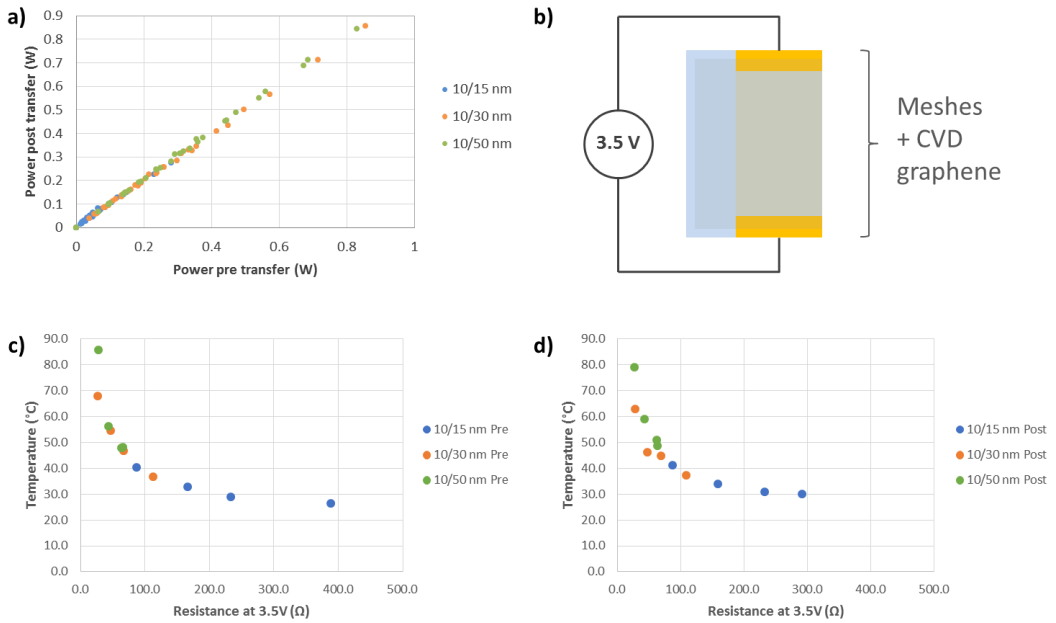
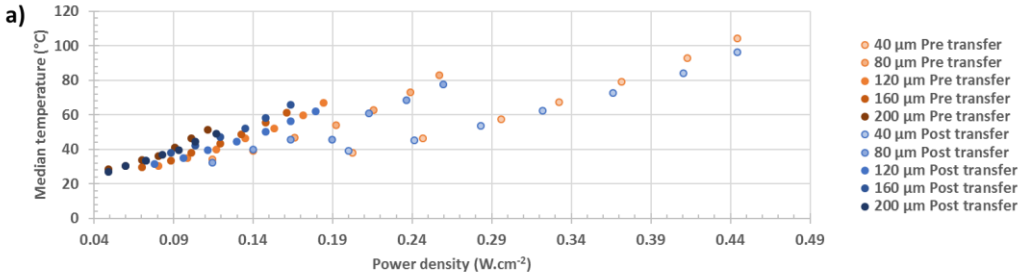
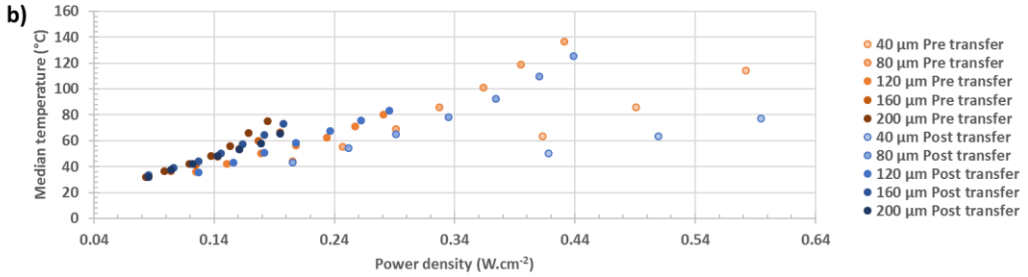


Figure 5.8: a) Comparison of the power during thermal testing pre- and post-transfer (all mesh configurations included) b) schematic of the sample testing c) and d) median temperature (at 3.5 volts) in function of the resistance at 3.5 volts pre- and post- transfer respectively.

In figure 5.8 a), the power was compared pre- and post- transfer. The slope and linearity of the data suggests that the electrical power pre- transfer was equivalent post- transfer. These observations indicate that no change of power occurred post-transfer eliminating the possibility of a change of temperature due to a change in the power consumption of the device. Additionally, the temperature was plotted in function of the device resistance for a voltage of 3.5 volts in figure 5.8 c) (pre) and d) (post). The samples with the lowest resistance reached the highest temperature. Despite the change of temperature pre- and post- transfer, the trend is conserved after the addition of graphene. However, variations are visible for samples with

resistance < 100 Ω suggesting that graphene's effect could be influenced by the initial resistance of the meshes.





c)

		Thermal resistivity (°C.cm^{-2}.W^{-1})	
		10/30 nm	10/50 nm
Pre transfer	40 µm	274.6	299.4
	80 µm	337.5	361.1
	120 µm	345.7	275.4
	160 µm	352.8	317.4
	200 µm	368.2	420.6
Post transfer	40 µm	232.6	153.6
	80 µm	307.6	290.1
	120 µm	303.4	301.4
	160 µm	347.2	345.5
	200 µm	322.6	294.2

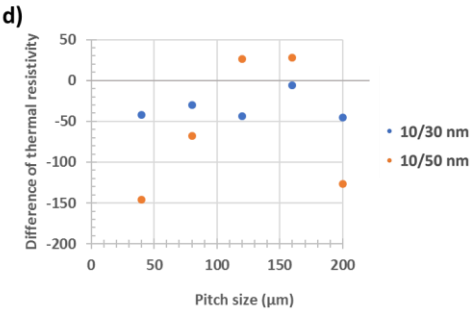


Figure 5.9: Study of the thermal resistivity. a) and b) median temperature as a function of the power density used for the thermal resistivity extrapolation in the case of the 10/30 nm and 10/50nm thick metal meshes. Each graphic groups the plots pre- and post- transfer for all pitch sizes. c) Table grouping the thermal resistivity obtained for each configuration pre- and post- transfer. d) Difference of thermal resistivity (Post – Pre) as a function of the pitch size.

The thermal resistivity is a parameter which depends on the power density and the temperature reached by the sample. The comparison pre- and post- transfer of this parameter can confirm whether the differences observed post transfer are due to change in the power consumption of the device. The thermal resistivity can also help to determine if parameters such as the resistance, the pitch size or the temperature of the devices could contribute to influence graphene effects.

Figure 5.9 a) and b) group the plots used to determine the thermal resistivity presented in fig. 5.9 c). The difference of resistivity pre- and post- transfer was plotted in function of the pitch size (figure 5.9 d)). The samples made of 10/30 nm of metals recorded a loss of thermal resistivity ranging from 0 to 50 °C.cm^2.W^{-1}. No clear pattern associates the pitch size with the difference of thermal resistivity. In the case of the 10/50 nm thick mesh, the difference of resistivity is even more variable ranging from -146 °C.cm^2.W^{-1} to 28°C.cm^2.W^{-1}.

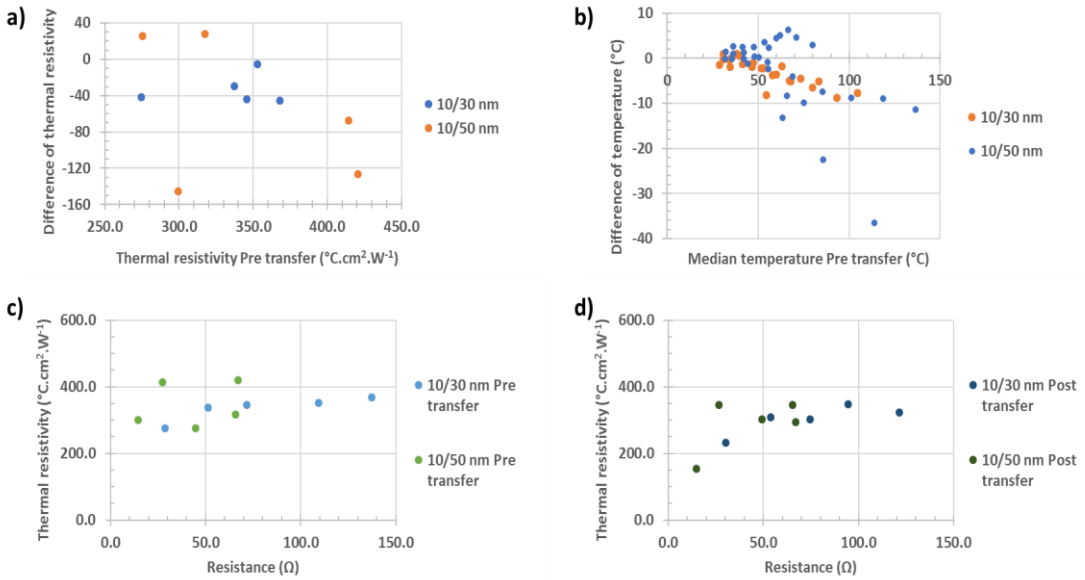


Figure 5.10: a) Difference of thermal resistivity (post-pre) in function of the thermal resistivity of the transparent heater pre- transfer of graphene b) Difference of temperature (post-pre) as a function of the temperature pre- transfer c) and d) Thermal resistivity in function of the resistance of the main device used for the thermal analysis pre- and post- transfer.

In figure 5.10 a), the difference in thermal resistivity was plotted in function of the thermal resistivity pre- transfer. No trend is observed meaning that the thermal performance of the mesh heater does not influence the effect of graphene.

In figure 5.10 b) the difference of temperature was plotted in function of the median temperature. The difference of temperature pre- and post- transfer is limited when the sample reaches temperatures < 50°C. In that case the difference increases when the temperature reached by the device pre-transfer increases. Note that the temperature doesn't determine if the difference is positive or negative.

Finally, in figure 5.10 c) and d) the thermal resistivity was plotted as a function of the device resistance pre- and post- transfer to verify if the observations made in figure 5.8 can be confirmed. The difference between pre- and post- transfer do not follow any pattern cancelling the possibility of the resistance influence.

5.3.4 Lead for future work: comparison pre-, post- and 6 months post transfer

In this last section, the device with 200 µm pitch size and 10/50 nm thick metals was re-tested 6 months after the transfer of graphene. Figure 5.11 groups all the thermal results including pre transfer, immediately post transfer and 6 month post transfer. It is clearly visible in figure 5.11 a) that the median temperature that was originally negatively impacted by the addition of graphene, recovered 6 months after the transfer. Furthermore, the temperatures obtained for voltage less than 4.0 volts are superior 6 months after transfer. The temperature distribution – visible in figure 5.11 b)- is also affected. The temperature distribution after 6 months is also superior to the distribution obtained directly post transfer. As expected by the temperature changes, the thermal resistivity is also influenced by the 6-month breaks (figure 5.11 c)). The change of thermal properties occurring could be due to many factors such as the long exposure of the sample to the environment, an accumulation of humidity between the graphene and the substrate etc. These factors should be investigated in future work.

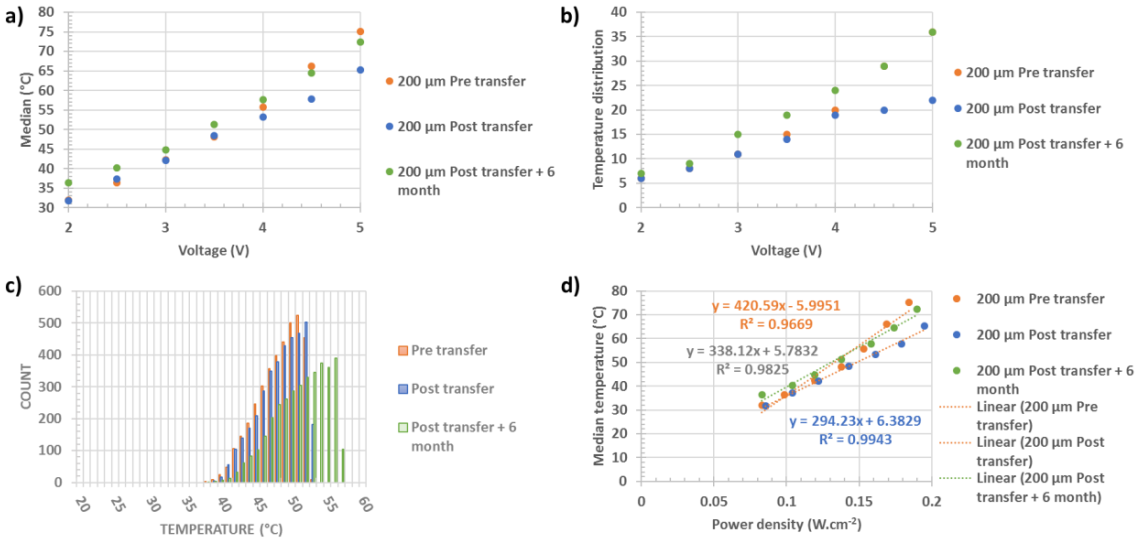


Figure 5.11: Evolution of the thermal performance of a device with 200 µm pitch size and made of 10/50 nm of titanium and gold, including pre (orange) and post (blue) transfer of graphene as well as 6 months after the transfer of graphene (green). a) median temperature as a function of the voltage b) temperature distribution as a function of the voltage c) histograms of the temperature at 3.5 volts d) median temperature as a function of the power density, including the thermal resistivity obtained from the slope.

5.4 Conclusions

The investigations undertaken in this chapter determined important factors which influence the contribution of the graphene in the hybrid heaters.

Firstly, the contribution of graphene is having a limited impact on the electrical performance and transparency of the conductive electrode. The sheet resistance was only increased in the case of the 10/15 nm thick meshes. These devices had sheet resistances much higher than those of the 10/30 nm and 10/50 nm thick meshes. The transparency was in all case only impacted by 3 %.

Secondly, it was demonstrated that graphene influences the temperature of the transparent heater. It also enhances the change of distribution associated with the change of temperature. When the temperature is increased post transfer, the increase of the distribution is amplified by the graphene. On the other hand, when the temperature is decreased post transfer, the distribution is further minimised by the graphene.

While we did not determine specifically which factor determines the graphene contribution (increase vs decrease of the temperature and distribution) we managed to reduce the list of possibilities. The resistance and the pitch size of the meshes do not have any influence on the effects of graphene. The heat generated by the heater, however, influenced the change of temperature observed with graphene. It seems that the difference (positive or negative) is stronger with higher temperature. The comparison of this work with chapter 3 and the work of J. Kang and Y. Janka helped to determine that parameters such as mesh geometry, metal used and device structure (graphene on top or under the meshes) are not the source of the contradictory contributions of graphene.

Finally, the change in the thermal performance observed after 6 months suggests that the key to better understanding the role and contributions of graphene remains in the investigation of graphene itself. Future work should focus on studying the impact of environmental factors and process contamination.

5.5 References

1. Kang, J., et al., *An Ag-grid/graphene hybrid structure for large-scale, transparent, flexible heaters.* Nanoscale, 2015. **7**(15): p. 6567-6573.
2. Pop, E., V. Varshney, and A.K. Roy, *Thermal properties of graphene: Fundamentals and applications.* MRS Bulletin, 2012. **37**(12): p. 1273-1281.
3. Ong, Z.-Y. and E. Pop, *Effect of substrate modes on thermal transport in supported graphene.* Physical Review B, 2011. **84**(7): p. 075471.
4. Qiu, B. and X. Ruan, *Reduction of spectral phonon relaxation times from suspended to supported graphene.* Applied Physics Letters, 2012. **100**(19): p. 193101.
5. Seol, J.H., et al., *Two-Dimensional Phonon Transport in Supported Graphene.* Science, 2010. **328**(5975): p. 213-216.
6. Haskins, J., et al., *Control of Thermal and Electronic Transport in Defect-Engineered Graphene Nanoribbons.* ACS Nano, 2011. **5**(5): p. 3779-3787.
7. Lindsay, L., D.A. Broido, and N. Mingo, *Flexural phonons and thermal transport in graphene.* Physical Review B, 2010. **82**(11): p. 115427.
8. Aksamija, Z. and I. Knezevic, *Lattice thermal conductivity of graphene nanoribbons: Anisotropy and edge roughness scattering.* Applied Physics Letters, 2011. **98**(14): p. 141919.
9. Ghosh, S., et al., *Extremely high thermal conductivity of graphene: Prospects for thermal management applications in nanoelectronic circuits.* Applied Physics Letters, 2008. **92**(15): p. 151911.

Chapter 6: conclusions and future work

Conclusion

The goal of this study was to investigate whether a hybrid made of graphene and metal meshes would be a viable transparent electrode.

Chapter 1 started by outlining the number of applications and therefor markets dependent on transparent electrodes. Unfortunately it was underlined that the extraction of indium, one of the key materials used to make transparent electrodes, is not going to be sufficient to match the future quantities required. Nowadays, alternative transparent electrodes are investigated to avoid the disruption of the market dependent on this technology. The chapter focused on the requirements of a competitive transparent electrode and give a quick overview of the different existing alternatives. It was established that the developed electrode for this work was to meet the following set of characteristics:

- Sheet resistance < 50 Ω/□
- Transmittance > 80% from 400 nm to 800 nm not including the substrate
- Qualified for flexible application
- Suitable to use as heater

Graphene and metal meshes were given more attention due to their potential. The hybrid electrode would combine the excellent sheet resistance of the metal meshes with the better heat distribution properties of the graphene. The main challenges would remain in the fabrication of the electrode and its flexibility.

One of the key steps in the fabrication of the heater hybrid was the transfer of CVD graphene from its copper substrate to the mesh/substrate. The procedure involves many challenging steps due to the 2D nature of the material. The quality of the transferred graphene was not consistent. The graphene was subject to mechanical defects and surface contaminations. The work presented in chapter 2 focused on evaluating and improving the transfer procedure to limit the number of structural defects. A method well known in industry was used: Failure Mode and Effect

Analysis. This method was never previously used for the transfer of graphene, so it was adapted, and guidelines were developed. The new procedure was a more reliable and more efficient which validate the FMEA developed. The transferred graphene matched the quality recorded in literature and the mechanical defects were minimise to < 2%.

Chapter 3 focused on the fabrication and evaluation of the hybrid mesh. The geometry of the mesh and the substrate were picked to withstand mechanical strains such as bending. The metal mesh geometry was an asymmetric pentagon specifically designed to dissipate stress under strain. The metal chosen for the mesh was gold due to its high ductility. The meshes were evaporated on the surface of two polymer substrates commonly found in the literature for flexible electronics: PET and PEN. The performance of the hybrid as transparent electrodes and transparent heaters were evaluated pre- and post- graphene transfer. Regarding the transparent electrode performance, the hybrid on PET achieved a figure of merit of 128 (sheet resistance: 15.0 Ω/□ and transparency: 71.2% (82.9% without substrate)) while the hybrid on PEN yield a figure of merit of 105 (sheet resistance: 18.2 Ω/□ and transparency: 70.9%). Very few differences were observed pre- and post- transfer of graphene. On the other hand, net differences were observed between the thermal performance pre- and post- transfer of graphene for the hybrid on PET. PEN remained mainly unchanged. It was demonstrated that the thermal resistivity of the pentagonal mesh on PET was increased by 18.7% post transfer of graphene, reaching a thermal resistivity of 87.5 °C.cm^2.W^{-1}. The heater on PEN reached a thermal resistivity of 94.9 °C.cm^2.W^{-1}. The transparent heaters presented a response time between 20 and 30 seconds. Overall both electrodes match the goal set up at the start of this thesis. The hybrid on PET present slightly better electrical and optical characteristics. The addition of graphene also successfully enhanced its thermal potential. It was therefore favoured.

The electrodes on PET and PEN were tested for flexibility in chapter 4. Minimal changes of resistance were observed after repeated bending. However, the presence of cracks in the metal mesh post 1000 cycles suggests that the developed electrodes are only “mildly flexible”. Additional testing was done on the electrodes

on PET to investigate its potential for real life application. The results were encouraging as the new electrode managed to stand ON/OFF and long use testing.

It was anticipated that graphene could improve the thermal distribution of a transparent heater made of metal mesh. However, the results in chapter 3 suggested otherwise. Chapter 5 aimed to better understand the contribution of graphene when added on a mesh heater. It was observed that the addition of graphene has the potential to enhance or decrease the thermal ability of the electrode. In this study graphene was transferred on the surface of different square meshes configurations. The use of different metal thickness and pitch sizes enabled the investigation of parameters such as the sample resistance, temperature effects, thermal resistance etc. While the deciding factor remains unknown, the presented work offers a first step toward a better understanding of the contribution of graphene. We establish that the addition of graphene targets the temperature and the temperature distribution. The observed effect is dependent on the heat generated from the mesh. We can also confirm that this effect is independent from the electrical resistance, mesh geometry and pitch size.

Future works

Though the transfer procedure was significantly improved with the help of a FMEA in chapter 2, sub-micron contaminants at the graphene-substrate interface and on the exposed graphene surface (e.g., PMMA residue) remain. A FMEA study could be addressed using high resolution electron microscopy/spectroscopy and scanning probe methods.

The hybrids from chapter 3 were characterised using equipment available on site. Unfortunately, haze measurements are not included in this study. As mentioned in the introduction chapter, the haze is an important characteristic to verify. Future work includes those measurements.

Since micro-cracks were present after the flexibility test, the study of hybrids would benefit from additional mechanical testing. A bending test with shorter radius should be considered. The point of mechanical failure and the recovery capacity of the electrode should also be investigated.

The combined results from chapter 3 and 5 demonstrate that the pentagonal meshes are not as efficient heaters as the standard square meshes. Simulation studies should be considered to determine an optimum mesh design for flexible, transparent heaters.

Finally, the study started in chapter 5 should be pursued. The benefit would not only serve for the enhancement of transparent heater. Other applications also require heat management. Photovoltaic solar cells are a good example. Recent work has highlighted that the heat generated during the conversion of absorbed light to electricity directly impacts solar cell efficiency [1-5]. Such applications would benefit from a layer capable to evacuate the excess heat.

Understanding what factor determines if graphene will enhance or reduce the heating of a device is key to developing this technology. The change in the thermal performance observed after 6 months (presented in chapter 5) suggest that future work should focus on graphene interface. The possibility of contamination over graphene (PMMA or environmental contamination) and/or under graphene (process residue) could be affecting the conductivity of graphene.

Reference

1. Shahil, K.M.F. and A.A. Balandin, *Thermal properties of graphene and multilayer graphene: Applications in thermal interface materials.* Solid State Communications, 2012. **152**(15): p. 1331-1340.
2. Yadav, P., et al., *Effect of temperature and concentration on commercial silicon module based low-concentration photovoltaic system.* Journal of Renewable and Sustainable Energy, 2013. **5**(1): p. 013113.
3. Brinkworth, B.J. and M. Sandberg, *Design procedure for cooling ducts to minimise efficiency loss due to temperature rise in PV arrays.* Solar Energy, 2006. **80**(1): p. 89-103.
4. Hassabou, A., A. Abotaleb, and A. Abdallah, *Passive Thermal Management of Photovoltaic Modules—Mathematical Modeling and Simulation of Photovoltaic Modules.* Journal of Solar Energy Engineering, 2017. **139**(6): p. 061010-061010-9.
5. Tong, X.C., *Advanced Materials for Thermal Management of Electronic Packaging*. Springer.

Appendices

Appendix S1: Optical and Raman characterisation

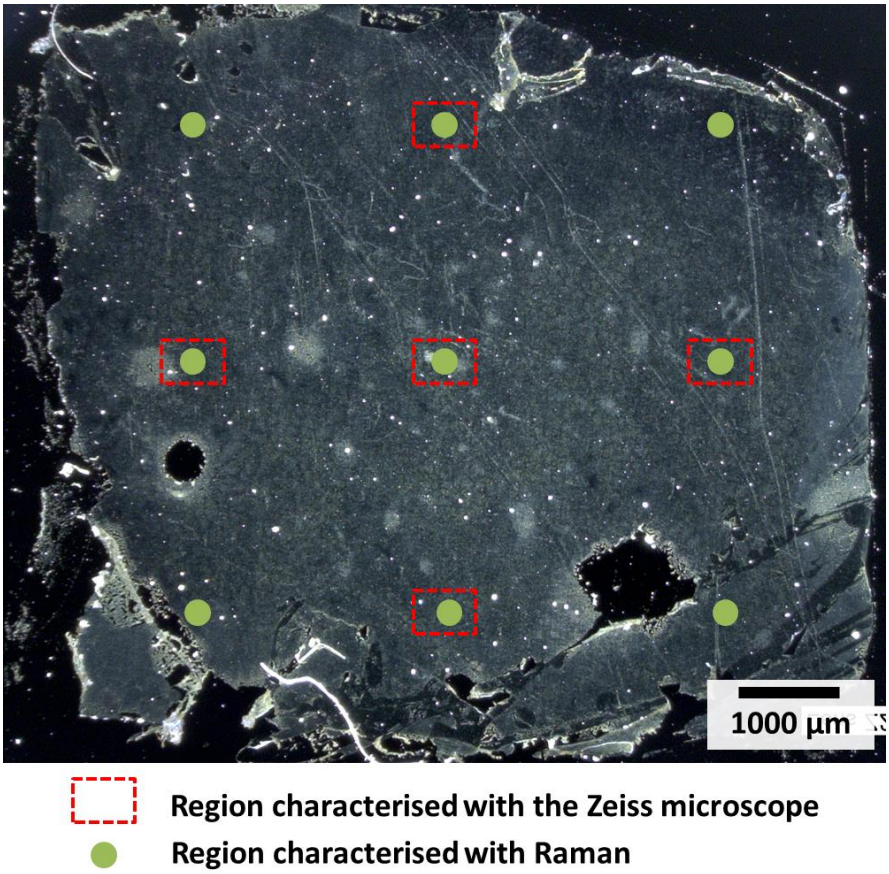


Figure A1. Centimere-scale optical image of a transferred graphene monolayer (standard transfer procedure). The dashed boxes indicate approximate locations of regions examined using high resolution microscopy (see Figure S2 below) and the circles indicate regions characterised using Raman spectroscopy

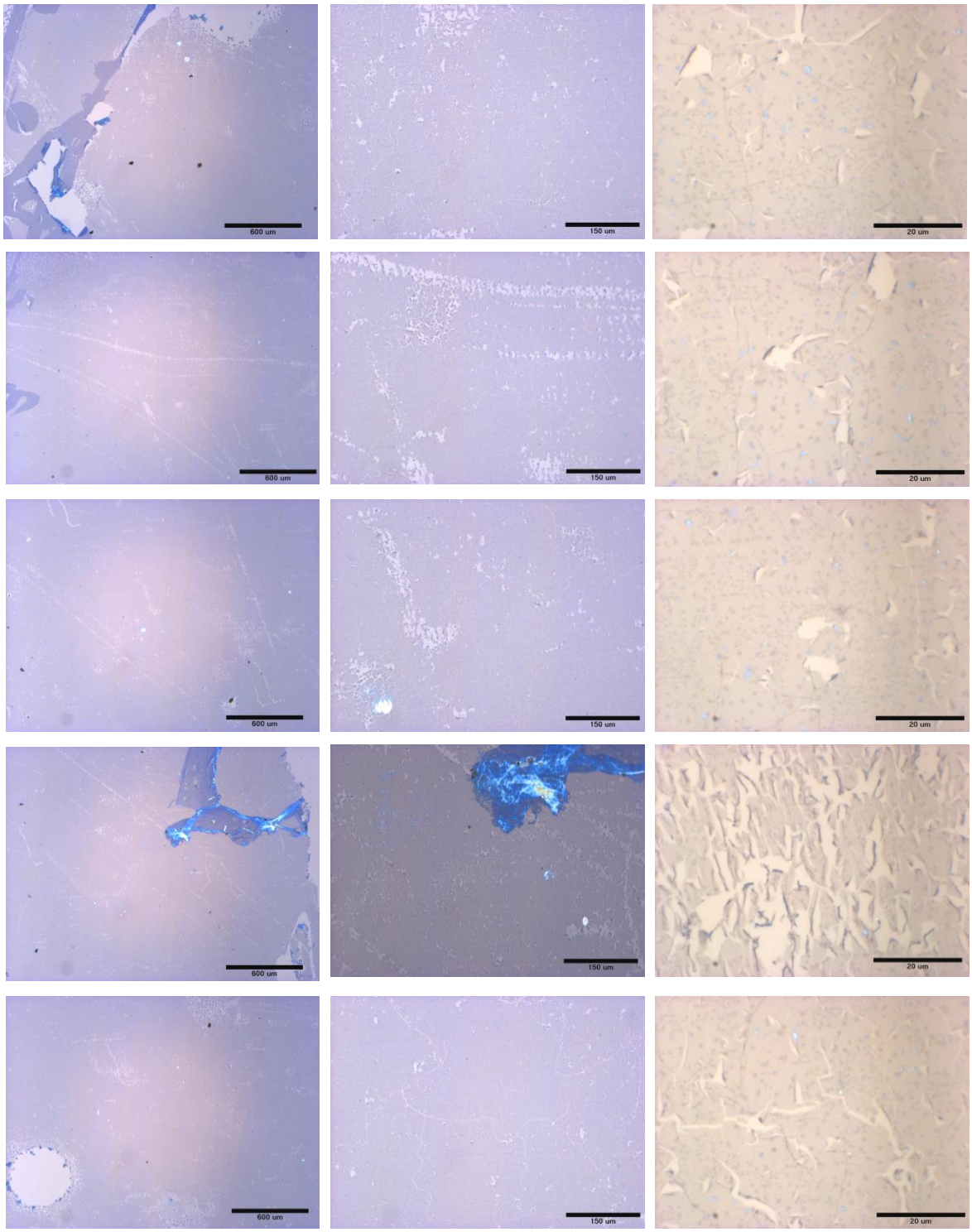


Figure A2. Optical characterisation at 2.5X (left column), 10X (middle column) and 100X (right column) for the five regions marked in Figure A1. The 100X images were analysed using the ImageJ analysis presented in Section S2.

Appendix S2: Image analysis for defect monitoring

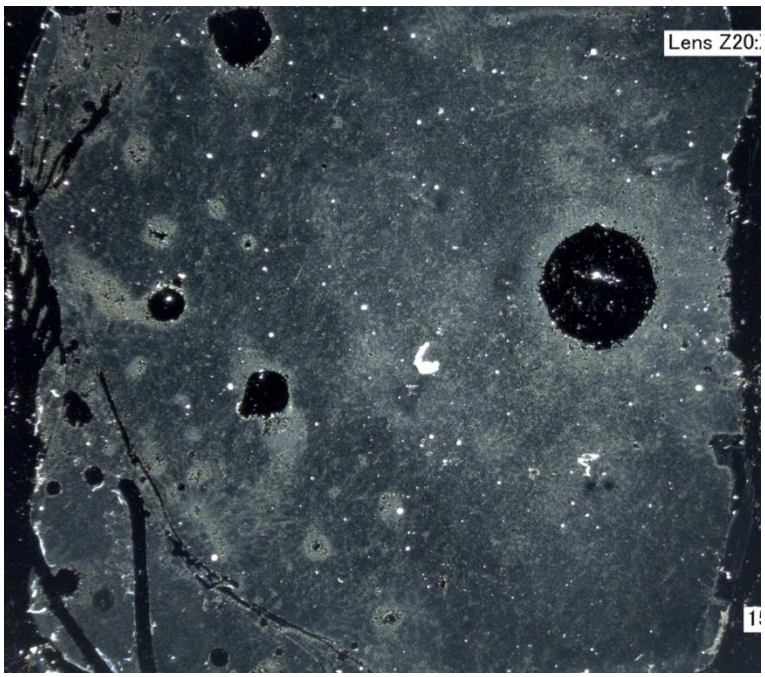


Figure S3. Original image of cm-scale transferred graphene

With the image loaded into ImageJ, the following processing steps are performed:

Step 1: Image > Type > 8 bits (converts to 8-bit greyscale)

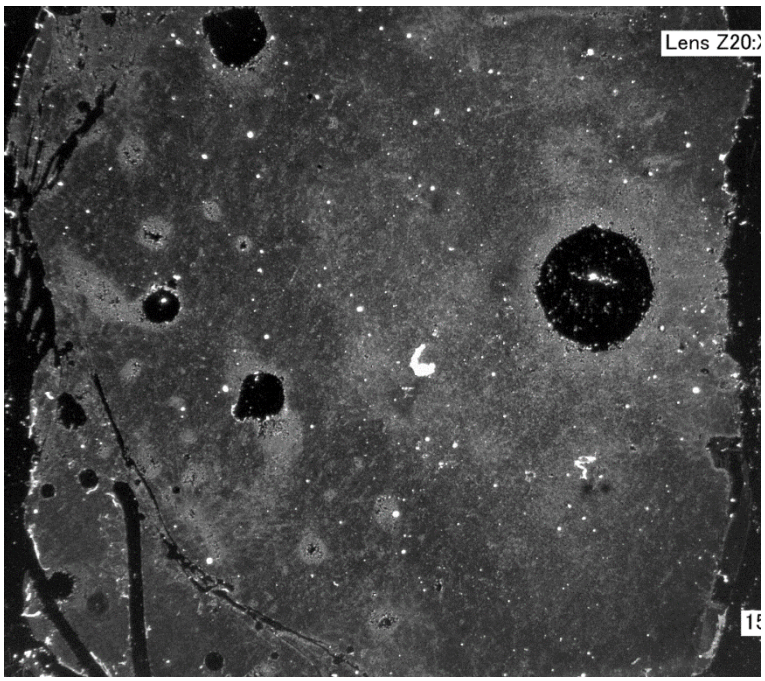
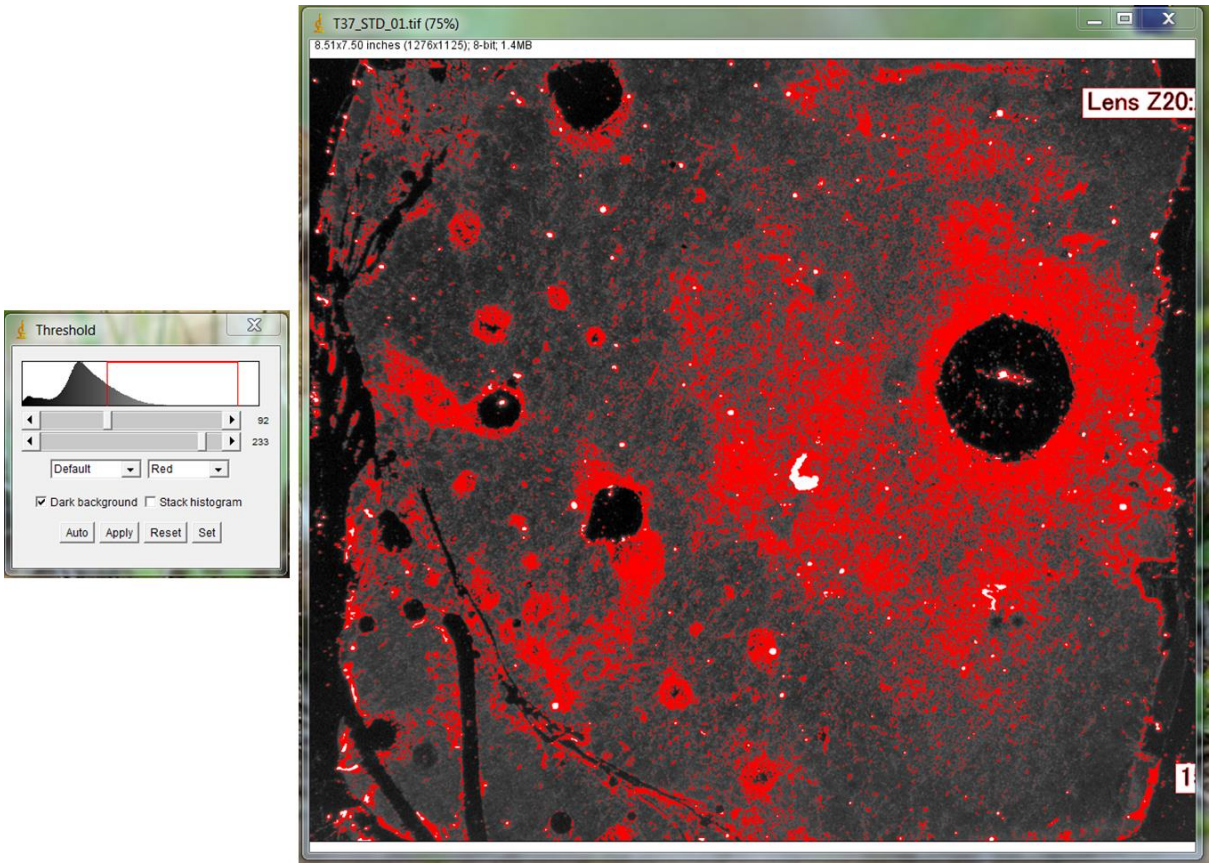


Figure S4. Image converted to 8-bit greyscale

Step 2: Image > Adjust > Threshold (adjust threshold to identify edges)



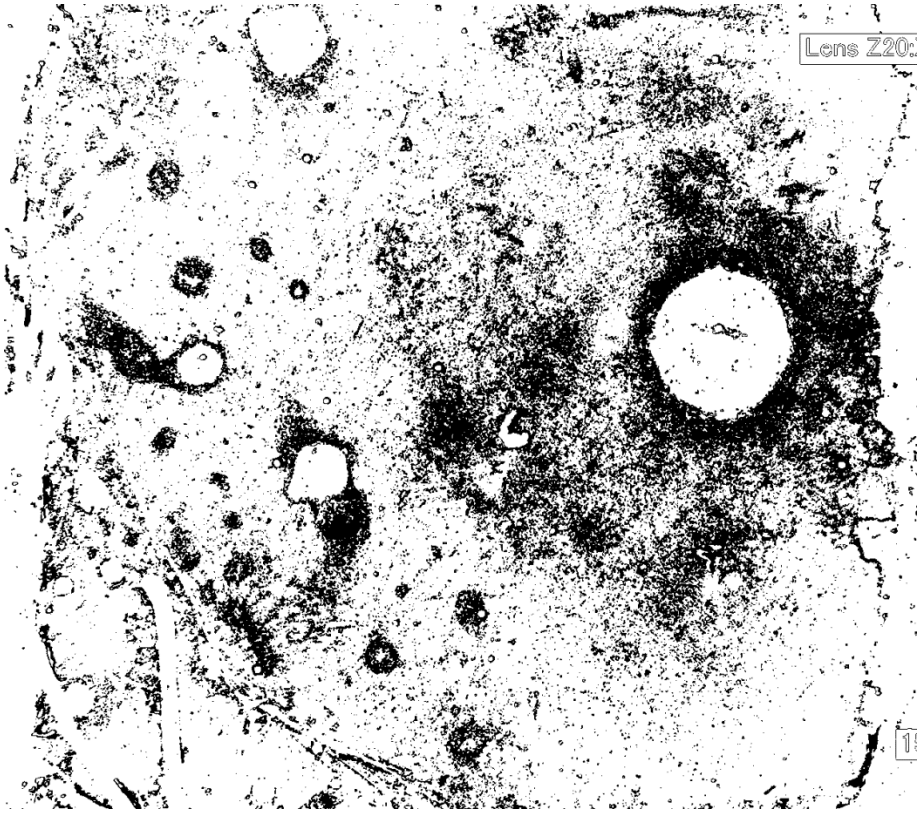
Step 3: Analyze > Measure (identifies number of "defect" pixels – N_1)

Step 4: Close threshold window

Edit > Selection > Select all

Edit > Selection > Make inverse

Process > Binary > Make Binary



Step 5: Image > Adjust > Threshold

Adjust the threshold as appropriate

Step 6: Analyze > Measure (identifies number of "non-defect" pixels – N_2)

The "percentage of defects" for this image is then $100\times N_1 /(N_1+ N_2)$

Appendix S3: Failure Modes Effect Analysis

Table A1 Criteria used to determine severity (SEV) scores

Effect	Severity of Effect	Score
Very High Severity	Final product unusable – 50% of graphene transferred to no graphene transferred	10
	Final product usable with difficulty– Large and small defects on 40 to 50% of the final product	9
	Final product usable with difficulty – Large and small defects on 30 to 40% of the final product	8
High Severity	Final product usable with difficulty – Large and small defects on 20 to 30% of the final product	7
	Final product usable with difficulty – Large and small defects on 15 to 20% of the final product	6
Medium Severity	Final product usable – Large and small defects on 10 to 15% of the final product	5
	Final product usable – Large and small defects on 5 to 10% of the final product	4
	Final product usable – Large and small defects on 2.5 to 5% of the final product	3
Low Severity	Final product easily usable – Large and small defects on < 2.5% of the final product	2
	Final product easily usable – Small defects on < 1% of the final product	1

Table A2 Criteria used to determine likelihood of occurrence (OCC) scores

Occurrence	Probability of failure (P)	Score
Very High probability	P > 8 per 10 samples	10
	7 < P ≤ 8 per 10 samples	9
	6 < P ≤ 7 per 10 samples	8
High probability	5 < P ≤ 6 per 10 samples	7
	4 < P ≤ 5 per 10 samples	6
Medium probability	3 < P ≤ 4 per 10 samples	5
	2 < P ≤ 3 per 10 samples	4
	1 < P ≤ 2 per 10 samples	3
Low probability	1 ≤ P ≤ 2 per 20 samples	2
	P < 1 per 20 samples	1

Table A3 Criteria used to determine likelihood of detection (DET) scores

Detection	Likelihood of detection	Score
No method	No method applied	10
Inaccurate method	Method can only detect impact on overall sample such as mechanical defect or contamination at millimetre scale (e.g. Visual inspection)	9
	Method detects mechanical defects or contamination larger than 10 µm	8
	Method detects mechanical defect or contamination larger than 1 µm	7
Accurate method	Method detects mechanical defect or contamination from 100 nm (e.g. SEM)	6
	Method reports surface details such as roughness or profile at nanoscale (e.g. AFM)	5
	Method detects variation in graphene quality (e.g. Electrical and Raman)	4
Very accurate method	Method detects and identify surface contamination	3
	Method provides details about the quality of graphene and contamination (e.g. XPS)	2
	Method detect defects at atomic level (e.g. TEM, TEM-EELS)	1

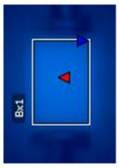
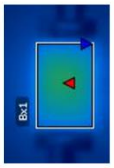
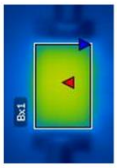
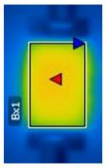
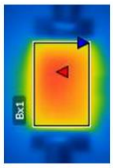
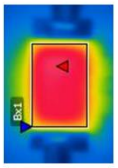
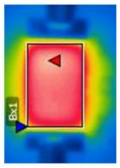
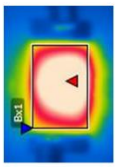
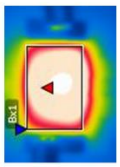
Table A4 Failure Modes Effects Analysis

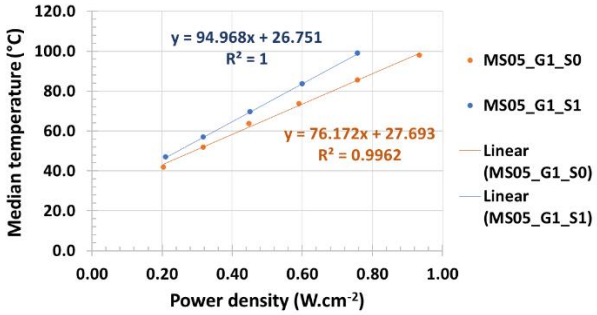
Process Step No.	Key Process Step or Input	Potential Failure Mode	Failure Mode No.	Potential Failure Effects	SEV	Potential Causes	OCC	Current Controls	DET	RPN	Ref.
S1	Unpackaging	Graphene in contact with packaging (vacuum sealed)	FM1	Delamination of graphene, surface contamination on remaining graphene.	9	No free space between graphene and packaging	10	None*	9	810	
S2	Cutting sample to size	Graphene / Copper substrate deformed when being cut into smaller samples.	FM2	Graphene delaminates from Cu or cracks form in graphene.	8	Non-rigid substrate.	10	None*	9	720	
S3	PMMA spin-coating	Samples deform when placed on chuck of spin-coater and suction engaged.	FM3	Delamination, cracks in graphene.	3	Non-rigid substrate. Diameter of the chuck vs sample. Damage from handling.	10	None*	9	270	
S3	PMMA spin-coating	PMMA thickness increases with "age" of solution.	FM4	Incomplete removal of PMMA due to thickness non-uniformity. Bubbles in PMMA. Delamination, cracks in graphene.	10	Local stress parallel or perpendicular to graphene-PMMA interface.	7	None**	8	560	21
S4	PMMA heat-curing	Copper can bend with the glassware used.	FM5	Delamination, cracks in graphene	1	Use of conventional glassware	8	none	9	72	
S5	RIE of back-side graphene	Sample stress/damage from loading into RIE chamber and from substrate holder	FM6	Delamination, cracks in graphene	3	Graphene manipulation. Contact with sample holder.	8	none	9	216	
S5	Transfer from RIE to copper etchant	Sample stress/damage when removing from RIE chamber	FM7	Delamination, cracks in graphene	3	Sample handling	8	none	9	216	
S6	Wet-etching of copper foil	Batch processing: multiples samples in etchant can come into contact	FM8	Delamination, cracks in graphene at sample edge	1	Multiple samples in bath	7	none	9	63	
S7	Transfer to DI water bath	Graphene damage when moved with glass pipette as part of transfer	FM9	Delamination, cracks in graphene	1	Stress applied on the sample	9	none	9	81	
S7	Transfer to DI water bath	Graphene surface in contact with "temporary transfer" substrate.	FM10	Delamination, cracks in graphene	7	Transfer of graphene from one bath to the other	10	none	9	630	35
S8	Transfer to target substrate	Poor adhesion to target substrate, moisture/residue between graphene and substrate	FM11	Delamination, cracks in graphene. Damage from bubbles	7	Transfer from water bath to target substrate	6	none	9	378	25, 35
S9	PMMA removal (heating and dissolution)	Sample introduced to pre-heated (180'C) hotplate	FM12	Delamination, cracks in graphene	7	Thermal shock	10	None***	8	560	
S9	PMMA removal (heating and dissolution)	Inadequate control of hotplate temperature	FM13	Incomplete removal of PMMA	10	Variance between real temperature and indicated temperature	1	none (thermometer can be used)	1	10	

* oxidation of copper (heating to 220 C on hotplate) can be used to reveal the homogeneity of graphene. ** Profilometer can be used to estimate PMMA thickness

***High-resolution optical microscope can be used post annealing - graphene is slightly visible through PMMA at 10X and 100 X

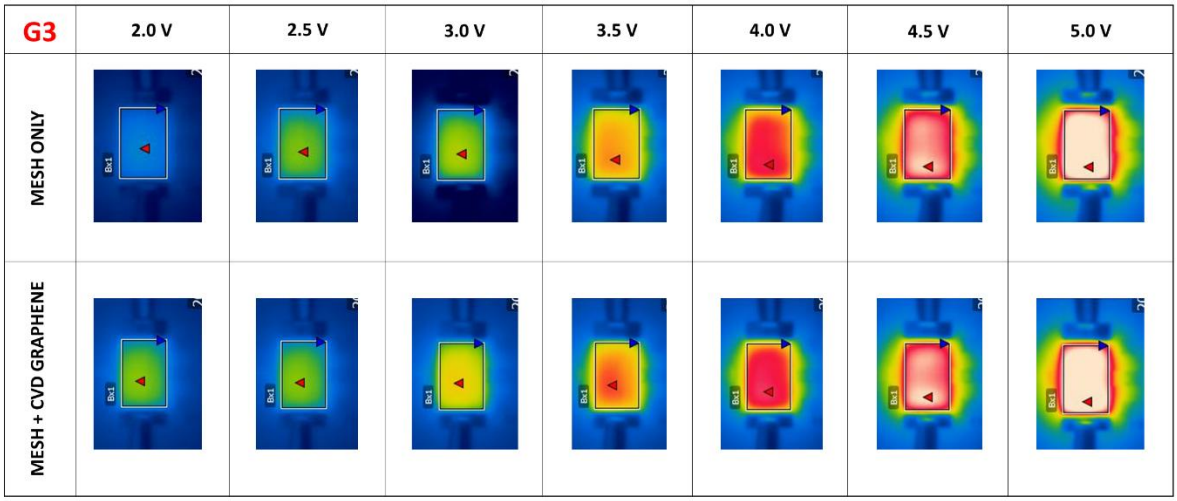
Appendix S4: Thermal analysis of each pentagonal meshes on PET substrate pre- and post- transfer of CVD graphene

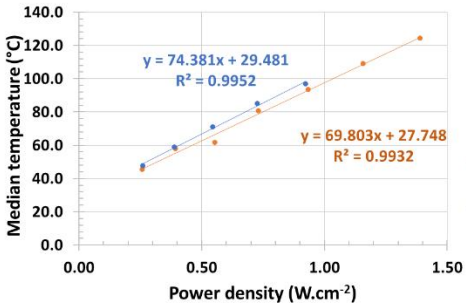
G1	2.0 V	2.5 V	3.0 V	3.5 V	4.0 V	4.5 V	5.0 V
MESH ONLY							
MESH + CVD GRAPHENE							



Pre transfer
Resistance (2 points)= 26.7 Ω
Sheet resistance = 16.5 Ω/□

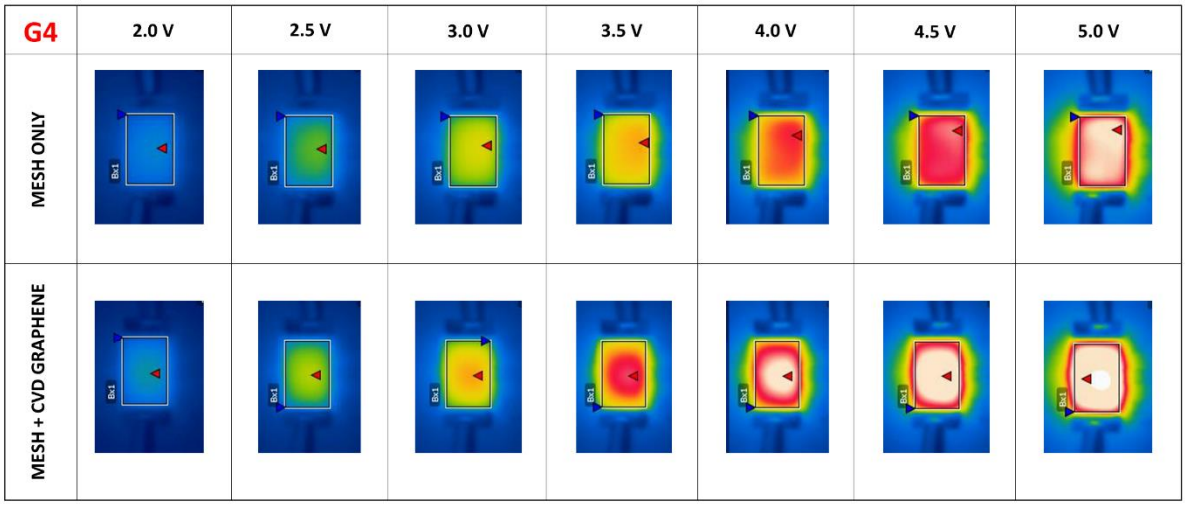
Post transfer
Resistance (2 points)= 26.7 Ω
Sheet resistance = 16.2 Ω/□

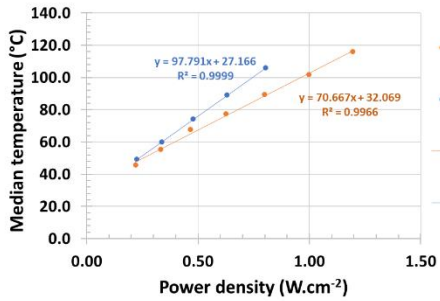




Pre transfer
Resistance (2 points)= 22.1 Ω
Sheet resistance = 13.4 Ω/□

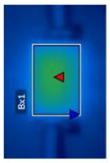
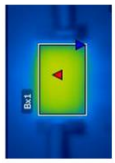
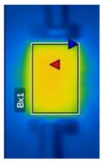
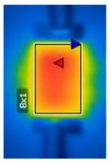
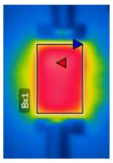
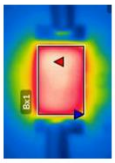
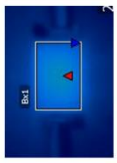
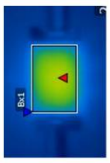
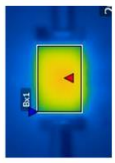
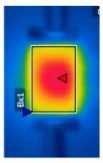
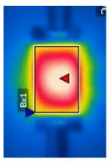
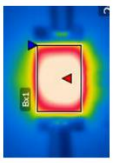
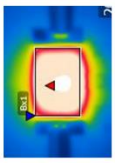
Post transfer
Resistance (2 points)= 23.3 Ω
Sheet resistance = 13.6 Ω/□

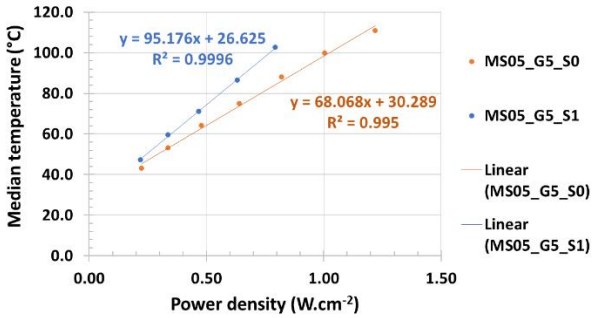




Pre transfer
Resistance (2 points)= 25.5 Ω
Sheet resistance = 15.9 Ω/□

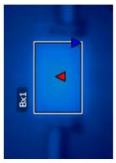
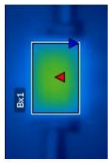
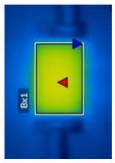
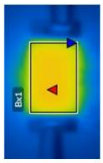
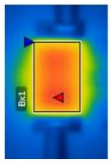
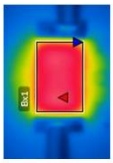
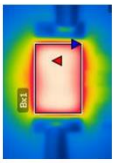
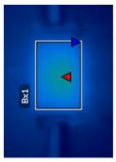
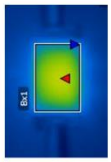
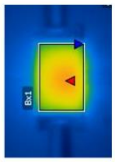
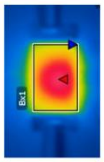
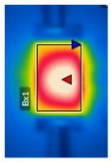
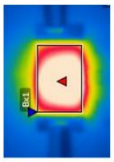
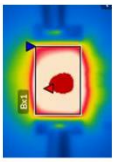
Post transfer
Resistance (2 points)= 27.1 Ω
Sheet resistance = 15.6 Ω/□

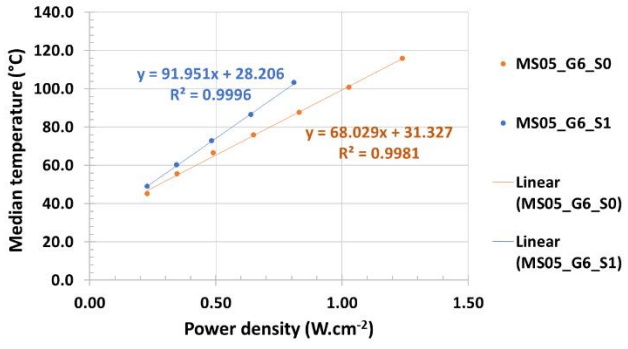
G5	2.0 V	2.5 V	3.0 V	3.5 V	4.0 V	4.5 V	5.0 V
MESH ONLY							
MESH + CVD GRAPHENE							



Pre transfer
Resistance (2 points)= 26.0 Ω
Sheet resistance = 15.4 Ω/□

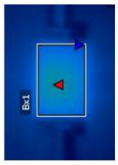
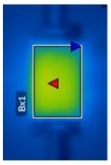
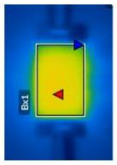
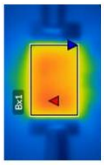
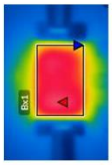
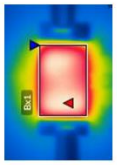
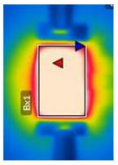
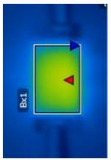
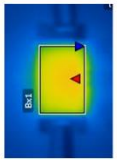
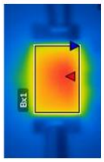
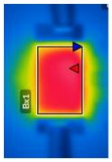
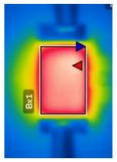
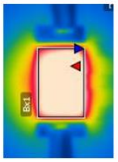
Post transfer
Resistance (2 points)= 25.9 Ω
Sheet resistance = 15.2 Ω/□

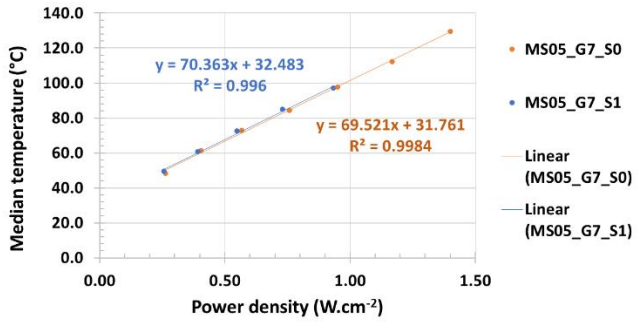
G6	2.0 V	2.5 V	3.0 V	3.5 V	4.0 V	4.5 V	5.0 V
MESH ONLY							
MESH + CVD GRAPHENE							



Pre transfer
Resistance (2 points)= 25.2 Ω
Sheet resistance = 15.4 Ω/□

Post transfer
Resistance (2 points)= 25.8 Ω
Sheet resistance = 15.2 Ω/□

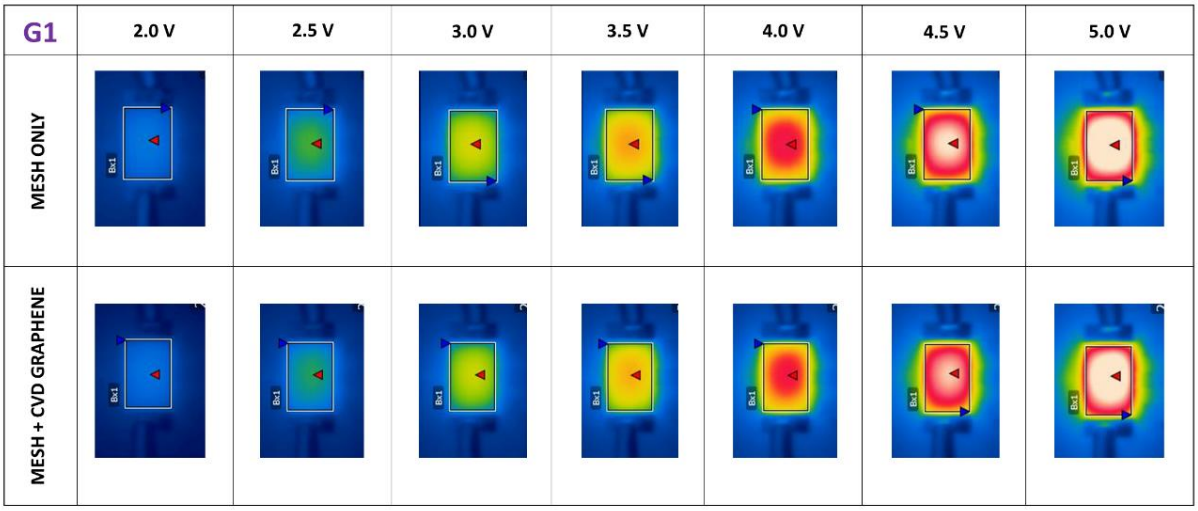
G7	2.0 V	2.5 V	3.0 V	3.5 V	4.0 V	4.5 V	5.0 V
MESH ONLY							
MESH + CVD GRAPHENE							

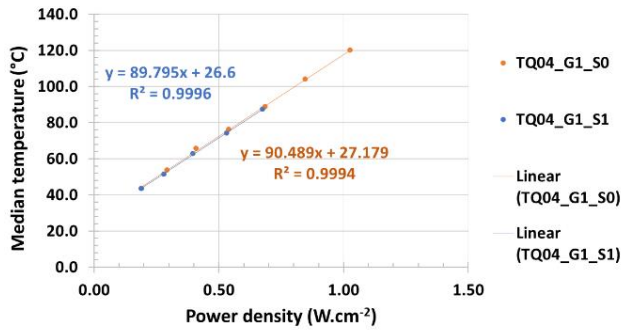


Pre transfer
Resistance (2 points)= 22.0 Ω
Sheet resistance = 13.5 Ω/□

Post transfer
Resistance (2 points)= 23.2 Ω
Sheet resistance = 13.5 Ω/□

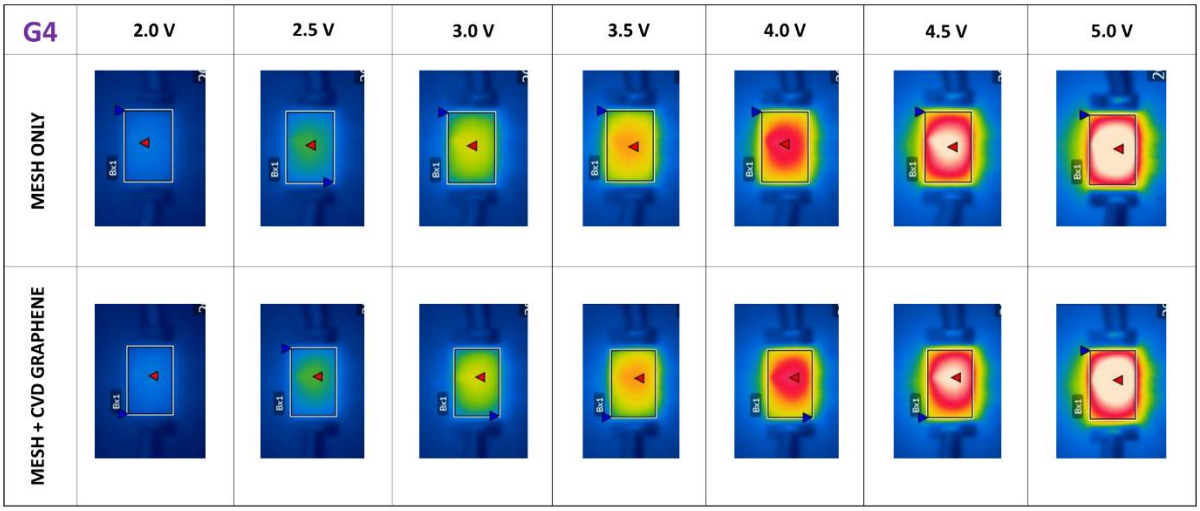
Appendix S5: Thermal analysis of each pentagonal meshes on PEN substrate pre- and post- transfer of CVD graphene

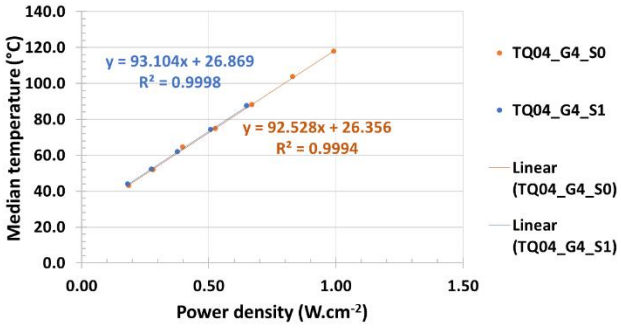




Pre transfer
Resistance (2 points)= 29.9 Ω
Sheet resistance = 17.0 Ω/□

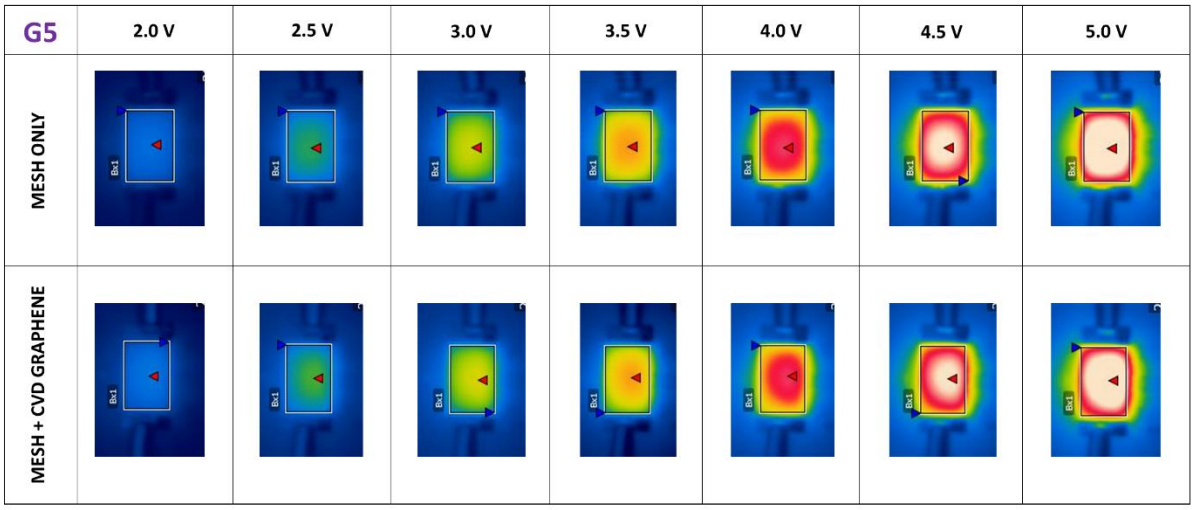
Post transfer
Resistance (2 points)= 30.9 Ω
Sheet resistance = 17.6 Ω/□

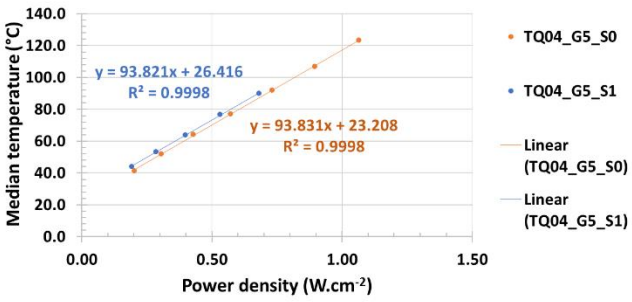




Pre transfer
Resistance (2 points)= 31.5 Ω
Sheet resistance = 17.4 Ω/□

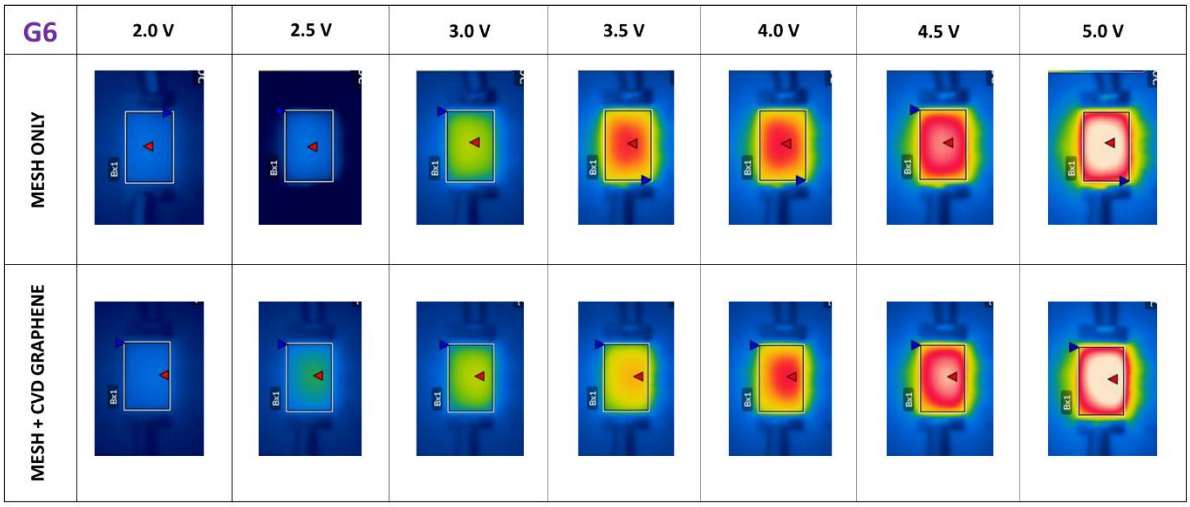
Post transfer
Resistance (2 points)= 32.4 Ω
Sheet resistance = 18.1 Ω/□

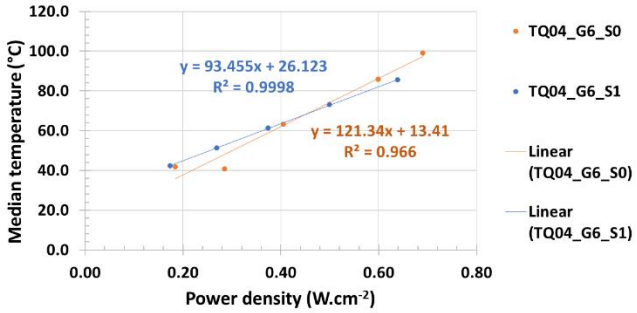




Pre transfer
Resistance (2 points)= 29.0 Ω
Sheet resistance = 17.5 Ω/□

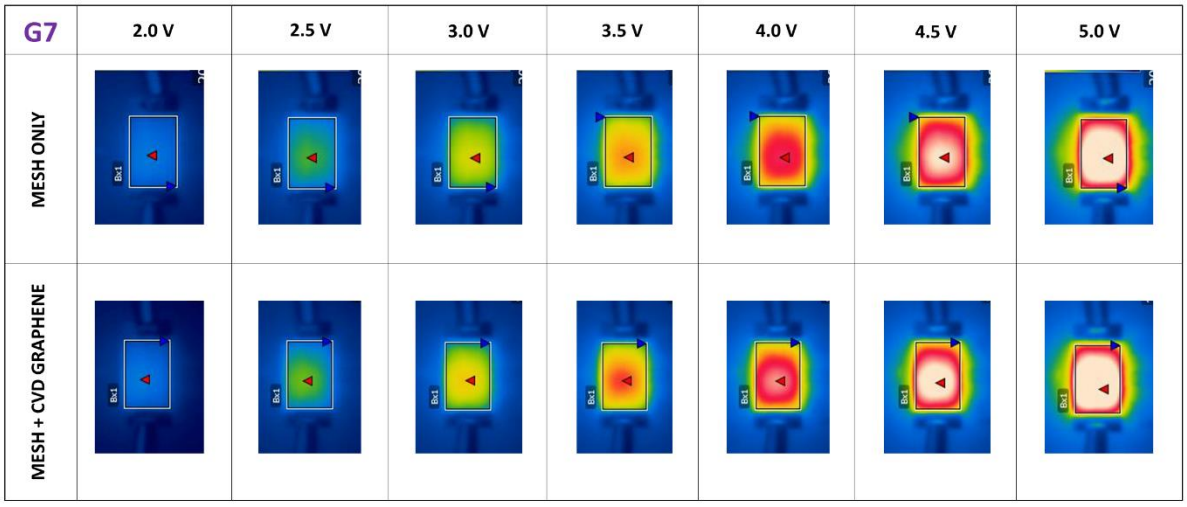
Post transfer
Resistance (2 points)= 30.3 Ω
Sheet resistance = 18.1 Ω/□

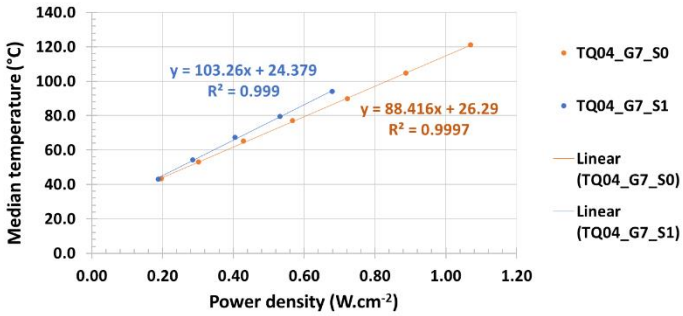




Pre transfer
Resistance (2 points)= 31.5 Ω
Sheet resistance = 18.5 Ω/□

Post transfer
Resistance (2 points)= 32.3 Ω
Sheet resistance = 19.4 Ω/□

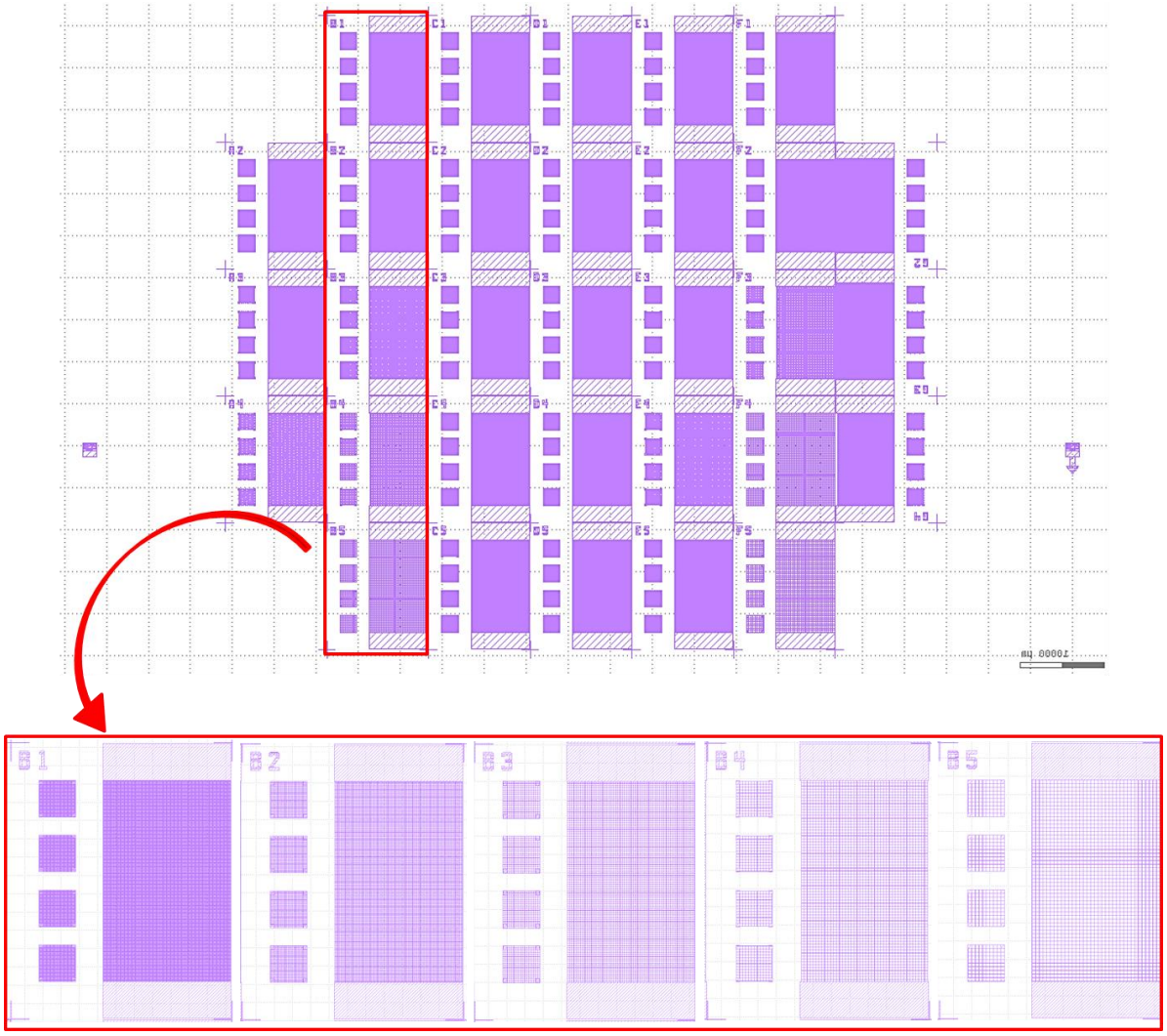




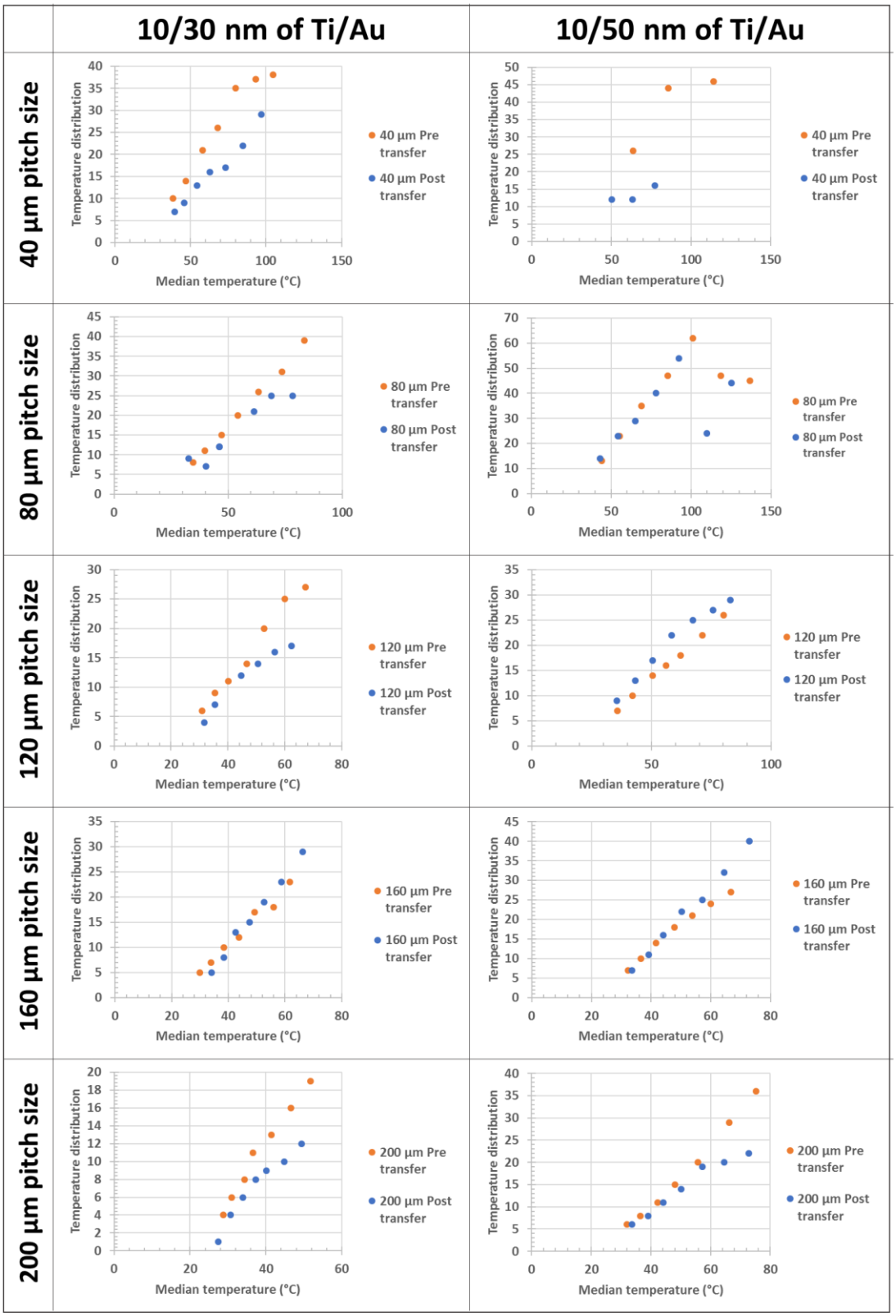
Pre transfer
Resistance (2 points)= 30.7 Ω
Sheet resistance = 17.4 Ω/□

Post transfer
Resistance (2 points)= 30.5 Ω
Sheet resistance =18.1 Ω/□

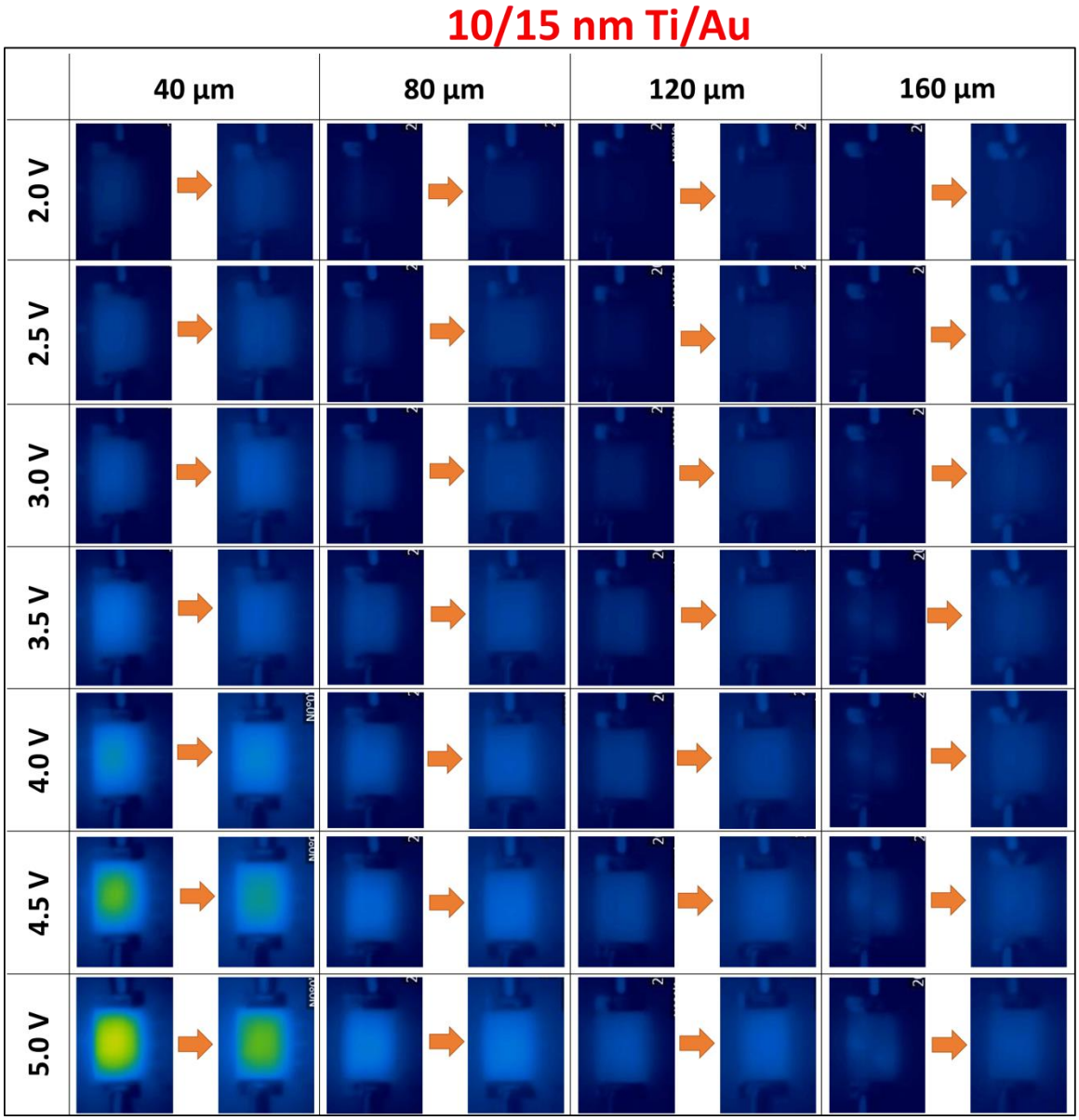
Appendix S6: Lithographic mask NTG-M050



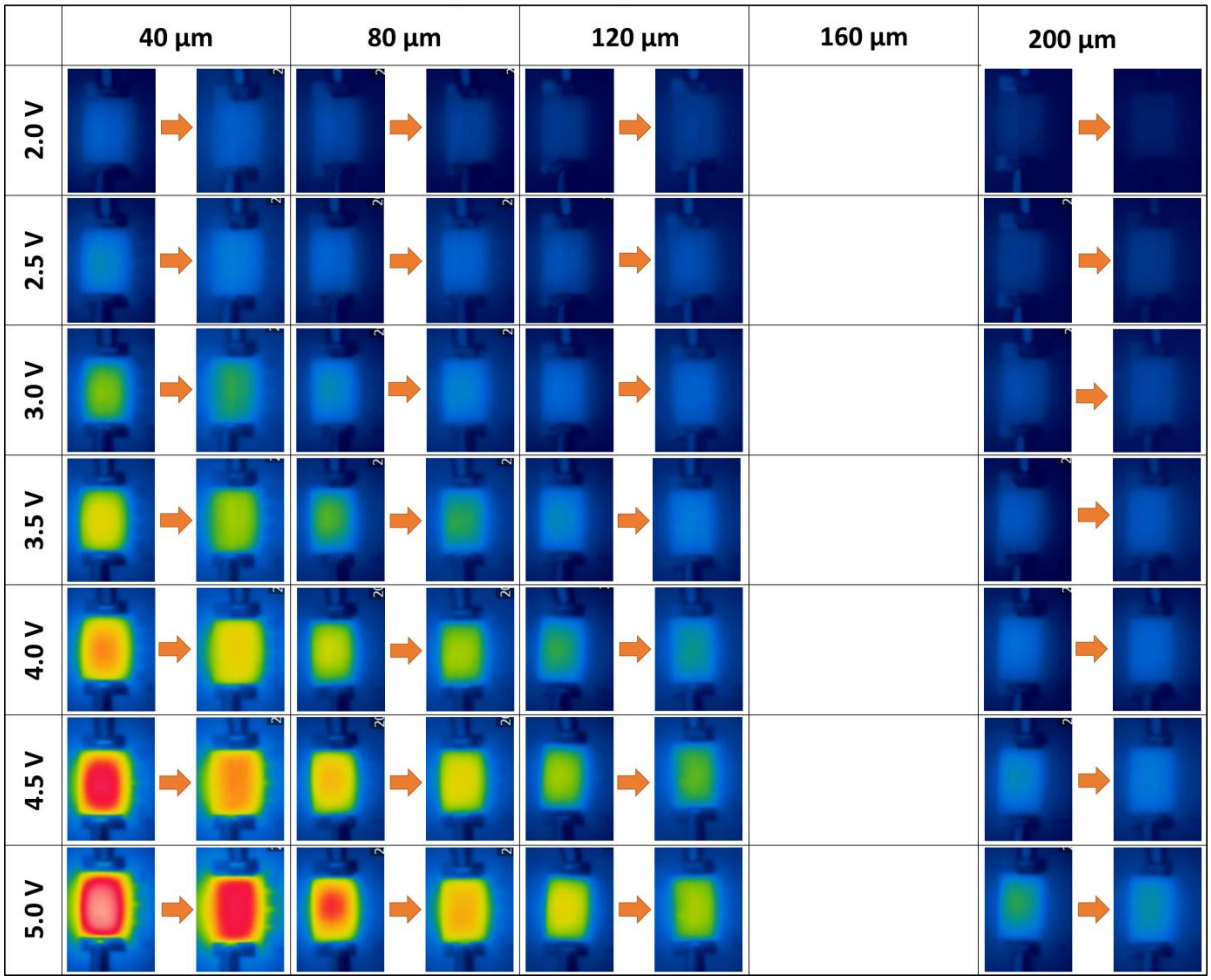
Appendix S7: Temperature distribution in function of the median temperature for square meshes (Chapter 5)



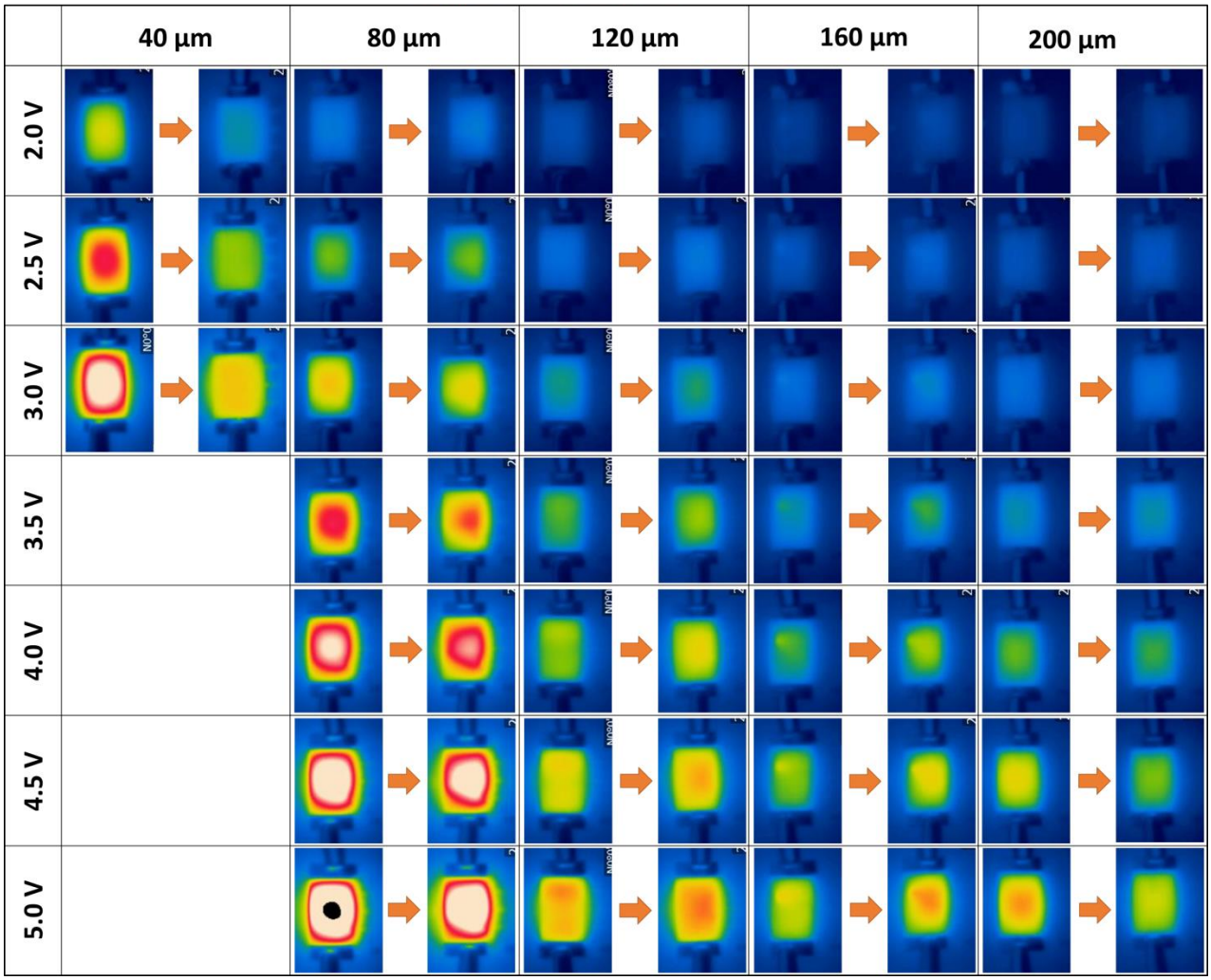
Appendix S8: Thermal image used for chapter 5 analysis



10/30 nm Ti/Au



10/50 nm Ti/Au



Appendix S9: Peer reviewed publications and modules

Publication

"Optimisation of graphene transfer using failure modes and effects analysis" *R. Puicervert, M. Otto, M. Manning, D. Neumaier, A.J. Quinn, and M. Burke – ACS Nano (Under review)*

Targeted publication

"Asymmetric pentagonal metal meshes and CVD graphene for flexible transparent electrodes and heaters" *R. Puicervert, N. Kelly, D. Lordan, R. Murphy, M. Manning, A.J. Quinn, and M. Burke*

Poster presentation

"Development of solar cell from p-doped graphene" *R. Puicervert, M. Manning, M. Burke and A.J. Quinn*

Tyndall postgraduate poster competition, Cork, July 2014, (Finalist)

"Oops my process is failing, what should I do now?" *R. Puicervert, M. Manning, M. Burke and A.J. Quinn*

Tyndall postgraduate poster competition, Cork, July 2016, (Finalist)

"Optimisation of the transfer of CVD graphene using FMEA" *R. Puicervert, M. Manning, M. Burke and A.J. Quinn*

Graphene2017 International Conference (Barcelona-Spain, March 28-31, 2017)

Oral presentation

"Molecular Functionalization of Exfoliated Graphene and Transferred CVD Graphene" Presented by Daniel Lordan

Materials Research Society, Symposium LL on Transparent Electrodes, April 2014, San Francisco

Module

SE6001 Compound Semiconductor Device Fabrication: Ridge Laser Fabrication (5 credits)

ST6013 Statistics and Data Analysis for Postgraduate Research Students (10 Credits)